Action-based quantum Monte Carlo approach to fermion-boson models

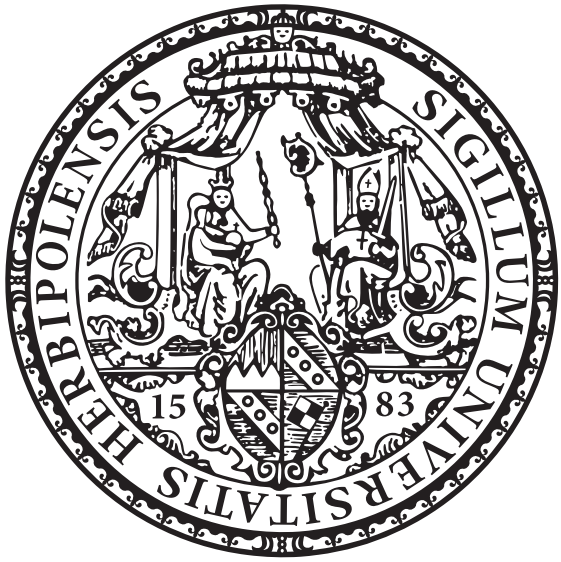

Dissertation zur Erlangung des naturwissenschaftlichen Doktorgrades der Julius-Maximilians-Universität Würzburg

vorgelegt von

Manuel Weber

aus Fulda

Würzburg 2017

Eingereicht am: 6. November 2017
bei der Fakultät für Physik und Astronomie

1. Gutachter: Dr. Martin Hohenadler
2. Gutachter: Prof. Dr. Giorgio Sangiovanni
3. Gutachter: Prof. Stefan Wessel, Ph.D.
der Dissertation.

Vorsitzende(r): Prof. Dr. Johanna Erdmenger

1. Prüfer: Dr. Martin Hohenadler
2. Prüfer: Prof. Dr. Giorgio Sangiovanni
3. Prüfer: Prof. Dr. Ralph Claessen
im Promotionskolloquium.

Tag des Promotionskolloquiums: 8. Februar 2018
Doktorurkunde ausgehändigt am:

Abstract

This work deals with the development and application of novel quantum Monte Carlo methods to simulate fermion-boson models. Our developments are based on the path-integral formalism, where the bosonic degrees of freedom are integrated out exactly to obtain a retarded fermionic interaction. We give an overview of three methods that can be used to simulate retarded interactions. In particular, we develop a novel quantum Monte Carlo method with global directed-loop updates that solves the autocorrelation problem of previous approaches and scales linearly with system size. We demonstrate its efficiency for the Peierls transition in the Holstein model and discuss extensions to other fermion-boson models as well as spin-boson models. Furthermore, we show how with the help of generating functionals bosonic observables can be recovered directly from the Monte Carlo configurations. This includes estimators for the boson propagator, the fidelity susceptibility, and the specific heat of the Holstein model. The algorithmic developments of this work allow us to study the specific heat of the spinless Holstein model covering its entire parameter range. Its key features are explained from the single-particle spectral functions of electrons and phonons. In the adiabatic limit, the spectral properties are calculated exactly as a function of temperature using a classical Monte Carlo method and compared to results for the Su-Schrieffer-Heeger model.

Zusammenfassung

Die vorliegende Arbeit beschäftigt sich mit der Entwicklung und Anwendung neuer Quanten-Monte-Carlo-Methoden zur Simulation von Fermion-Boson-Modellen. Grundlage für unsere Entwicklungen ist der Pfadintegralformalismus, in dem das exakte Ausintegrieren der bosonischen Freiheitsgrade zu einer retardierten fermionischen Wechselwirkung führt. Wir geben einen Überblick über drei Methoden, die für die Simulation retardierter Wechselwirkungen geeignet sind. Insbesondere entwickeln wir eine neue Quanten-Monte-Carlo-Methode mit globalen Updates, die das Autokorrelationsproblem früherer Ansätze löst und linear in der Systemgröße skaliert. Wir demonstrieren die Effizienz dieser Methode am Beispiel des Peierls-Übergangs im Holstein-Modell und diskutieren Erweiterungen auf andere Fermion-Boson-Modelle sowie Spin-Boson-Modelle. Des Weiteren zeigen wir, wie mithilfe erzeugender Funktionale bosonische Observablen direkt aus den Monte-Carlo-Konfigurationen berechnet werden können. Dies beinhaltet unter anderem den Boson-Propagator und die spezifische Wärme des Holstein-Modells. Die methodischen Entwicklungen dieser Arbeit erlauben es uns, die spezifische Wärme des spinlosen Holstein-Modells in seinem gesamten Parameterbereich zu untersuchen. Ihre wesentlichen Merkmale werden mithilfe der Einteilchenspektralfunktionen von Elektronen und Phononen erklärt. Im adiabatischen Grenzfall verwenden wir eine klassische Monte-Carlo-Methode, um die Temperaturabhängigkeit der Spektralfunktionen exakt zu berechnen, und vergleichen unsere Ergebnisse für das Holstein-Modell mit Resultaten für das Su-Schrieffer-Heeger-Modell.

Contents

1. Introduction

The interplay between electronic and lattice degrees of freedom is fundamental to solid-state physics and leads to a variety of interesting phenomena. The most intriguing is maybe the onset of superconductivity at very low temperatures that was discovered by Kamerlingh Onnes in 1911 and since then was observed in many different materials [1]. It took physicists half a century to understand that electron-phonon coupling causes an attractive interaction between electrons and finally leads to an instability of the Fermi surface towards the formation of Cooper pairs [2]. This insight led Bardeen, Cooper, and Schrieffer to formulate their microscopic theory of conventional superconductivity that is now known as BCS theory [3]. For one-dimensional (1D) systems, the situation is inherently different. Fermi-liquid theory breaks down and the metallic phase is either described by a Tomonaga-Luttinger liquid [4, 5] or a Luther-Emery liquid [6]. Here, electron-phonon coupling is the driving force behind the Peierls instability: under the formation of a periodic lattice modulation the metallic state becomes unstable towards charge-density-wave (CDW) order [7]. The theoretical study of conjugated polymers revealed that domain walls between different dimerization patterns may be associated with topological excitations called solitons which appear inside the Peierls gap of the electronic spectrum [8, 9]. Only recently, these kinds of systems have been identified as the simplest realizations of topological band insulators [10]. Furthermore, strong electron-phonon interaction in semiconductors or polymers leads to the formation of polarons [11], i.e., electrons that are screened by a cloud of lattice deformations [12]. Recently, the study of nonequilibrium dynamics using, e.g., pump-probe experiments has attracted a lot of interest. In this context, electron-phonon interaction plays an important role for the relaxation of excited states [13].

For many physical phenomena and in particular for the ones described above, much of our understanding relies on the study of simplified models that capture the key features of a physical problem. As long as these models are simple enough, analytic approaches to their solution are very successful and can explain the basic mechanisms behind physical observations. In many of these cases, the quantum many-particle problem reduces to an effective single-particle description. However, as interactions between particles become more complex, analytic approaches often become approximate and only valid in certain regions of parameter space. Rigorous mathematical solutions to the many-particle problem only exist in special cases. In general, the quantum many-particle problem cannot be solved exactly and therefore requires numerical approaches. To illustrate this point, we consider the Peierls transition in the 1D Holstein molecular-crystal model [14, 15] at half-filling, one of the standard models to describe electron-phonon coupling and the central model studied in this work. The Holstein model consists of free electrons on a lattice in the tight-binding approximation, free phonons described by local

harmonic oscillators, and a local electron-phonon coupling of the density-displacement type.[1] While for some 1D models like the Hubbard model there exist exact solutions by the Bethe ansatz [16–18], the Holstein model lacks a general solution. Nonetheless, it has been shown analytically that the ground-state of a generic electron-phonon model is a spin singlet [19]. According to Peierls' theorem, any finite electron-phonon coupling should lead to an insulating ground state [7]. In the adiabatic approximation, where the phonons lose their dynamics, this is indeed true and the ground state is exactly given by mean-field theory [20]. However, quantum fluctuations of the lattice destroy the ordered state at a critical phonon frequency and lead to a metallic ground state, in contradiction to Peierls' theorem. The detection of the Tomonaga-Luttinger liquid phase in the spinless Holstein model as well as the Luther-Emery phase in the spinful Holstein model required ongoing numerical studies using different approaches [20–30], as reviewed in Ref. [31]. The determination of the phase boundaries is complicated by an exponentially small Peierls gap in the vicinity of the Berezinskii-Kosterlitz-Thouless quantum phase transition as well as the existence of a spin gap in the metallic phase of the spinful Holstein model [32]. To overcome these shortcomings, the further development of efficient numerical methods is essential.

During the last decades, different numerical methods have been developed to simulate the quantum many-particle problem. The most established methods that promise exact results for model Hamiltonians are exact diagonalization (ED) [33], the density-matrix renormalization group (DMRG) [34, 35], and quantum Monte Carlo (QMC) [36]. These methods have been applied to a variety of fermionic or bosonic models with great success. In particular, QMC methods are very efficient for bosonic and spin systems due to the existence of global updating schemes, but also give good results for fermionic models in the absence of a sign problem. By contrast, DMRG has become the method of choice for many 1D systems, where it efficiently calculates the ground state from a variational approach [37, 38]. However, the interplay between fermionic and bosonic degrees of freedom—as it is the case for electron-phonon models like the Holstein model—poses a difficult numerical problem for all of these methods. The major issue for ED and DMRG simulations is the unbound bosonic Hilbert space that must be truncated. Although this is not a principal problem—efficient truncation schemes have been developed in recent years [39–41]—the local state space is significantly enlarged in contrast to the case of fermionic models. The efficiency of ED and DMRG strongly depends on the size of the local Hilbert space: ED solves the many-body problem exactly and therefore suffers from an exponential scaling of complexity with the size of the local state space, whereas DMRG has a more favorable scaling with the so-called bond dimension (see Refs. [37, 38, 42] for details). Using advanced truncation schemes, ED results for the 1D spinless Holstein model at half-filling are available for up to $L = 10$ lattice sites [27, 43], whereas DMRG simulations reached $L = 256$ sites [29]. By contrast, QMC simulations usually do not suffer from the unbound bosonic Hilbert space, but can exhibit very long autocorrelation times because only local boson updates are available [44]. For example, in many QMC methods that are based on a Trotter discretization $\Delta\tau$ of

[1] For a definition of the Holstein model, see Eq. (2.3).

imaginary time [45, 46] the phonons are represented by continuous displacement fields $q_{i,\tau}$ at site i and time slice τ. Then, the kinetic energy of the phonons is given by the action $\mathcal{S}_{\mathrm{b,kin}} = K \sum_{i,\tau} (q_{i,\tau} - q_{i,\tau+1})^2 / (2\omega_0^2 \, \Delta\tau^2)$, where ω_0 is the phonon frequency and K the stiffness constant. Especially when $\omega_0 \, \Delta\tau \ll 1$, only small changes in the local displacements are accepted during a Monte Carlo update. This already leads to tremendous autocorrelation times for the harmonic oscillator [47]. Autocorrelations were shown to be absent for the polaron problem when sampling the principal components of the phonons and using a Lang-Firsov transformation [48]. However, generalizations to finite fillings were only successful for the 1D spinless Holstein model [49].

In QMC simulations, long autocorrelation times often appear in the vicinity of second-order phase transitions and are a consequence of local Monte Carlo updates. The first cluster algorithms that overcame critical slowing down in the Ising model were the Swendsen-Wang [50] and the Wolff algorithm [51]. These algorithms are constructed in such a way that the size of the clusters being updated scales with the correlation length of the system. Later, global updating schemes were also developed for quantum models. The first QMC method with global updates was the loop algorithm [52], followed by the worm [53], operator-loop [54], and directed-loop algorithms [55]. These algorithms have in common that they are based on a world-line representation of the partition function. Many bosonic and spin models as well as 1D fermionic models can by now be simulated very efficiently. However, apart from very specialized algorithms [56], global updates have not been formulated for fermion-boson models. Using global updates for the electrons and local updates for the phonons still results in long autocorrelation times near phase transitions [28]. For fermionic systems in more than one dimension, global updating schemes are rare: while the hybrid QMC method [57, 58] in principle includes global updates, its efficiency for problems in solid-state physics is currently under debate [59].

In this work, we consider an alternative approach to simulate fermion-boson models. It is based on the path-integral representation of the partition function and exploits that the bosons can be integrated out exactly if the action is quadratic in the bosonic fields [60]. One ends up with a retarded fermionic interaction, i.e., nonlocal in imaginary time, that is mediated by the free boson propagator. As a result, the bosonic fields need not be sampled in a Monte Carlo simulation anymore. Originally, this approach has been used to simulate the polaron problem, both in discrete [61–63] and continuous time [64–66], but applications to finite band fillings are also possible. For this purpose, the development of modern continuous-time QMC methods [67, 68]—that are predominantly used as impurity solvers for dynamical mean-field theory (DMFT) [69]—played an important role. Using the example of the Holstein model, it was shown in Ref. [70] that the continuous-time interaction expansion (CT-INT) method [67] gives good results for fermion-boson lattice models and especially allows for reliable simulations in the adiabatic regime of low boson frequencies [71]. The CT-INT method is very flexible regarding the models being simulated and allows the calculation of any fermionic correlation function from the single-particle Green's function using Wick's theorem. However, updates are based on determinantal identities leading to an expensive scaling of $\mathcal{O}(L^3\beta^3)$ operations to generate independent Monte Carlo configurations. Here, L is

the number of lattice sites and $\beta = 1/k_B T$ the inverse temperature. Nonetheless, the CT-INT method reaches system sizes up to $L = \beta t = 50$ [32] and can also be used to simulate two-dimensional fermion-boson models [P1]. Retarded interactions have also been included in the worm algorithm with global world-line updates, where system sizes of $L = 128$ and $\beta t = L/2$ were reached [72]. Because the interaction is nonlocal in imaginary time, the worm algorithm does not show the same performance as for equal-time interactions. By contrast, the directed-loop algorithm has not been able to treat nonlocal interactions in imaginary time so far, but nonlocal interactions in space can be simulated efficiently [73, 74]. Retarded interactions are also studied in the context of DMFT and the hybridization expansion method [75] to understand dynamical screening effects [76–78], and in extended DMFT calculations [79, 80].

The main goal of this thesis is the further development of the action-based QMC approach to fermion-boson problems. Our starting point is the CT-INT method, where retarded interactions are sampled in the form of vertices in a perturbation expansion. The main advantage of the action-based approach—to integrate out the bosons so that they need not be sampled—is also one of its few disadvantages: bosonic observables cannot be accessed directly anymore. However, with the help of generating functionals we can derive sum rules to recover bosonic observables from fermionic correlation functions. For example, the phonon propagator of the Holstein model can be recovered from the time-displaced charge-charge correlation function, which is directly accessible in the CT-INT method via Wick's theorem. We also develop another way of calculating bosonic observables: because we sample retarded interactions resulting from fermion-boson coupling, many bosonic observables can be inferred directly from the Monte Carlo configurations. This is a common feature of many QMC methods based on a series expansion and was used, e.g., to derive a unified QMC estimator for the fidelity susceptibility [81]. Furthermore, the analogy between different QMC methods led us to the development of a new algorithm for retarded interactions. It is based on the stochastic series expansion (SSE) representation [82] which provides global directed-loop updates [55]. Originally, the SSE representation was obtained from a series expansion in the total Hamiltonian, but it can also be derived from the path-integral approach where retarded interactions can be included. We formulate an efficient directed-loop algorithm for retarded interactions that solves the autocorrelation problem for various fermion-boson models. We test our method for the 1D spinless Holstein model and reach system sizes up to $L = 1282$ and $\beta t = 2L$.

The algorithmic developments of this thesis allow us, for the first time, to study the thermodynamic properties of Peierls chains using the example of the spinless Holstein model.[2] While the ground-state properties of the Holstein model are in principle known from QMC or DMRG, a systematic study of thermodynamic observables like the specific heat was out of reach so far. In QMC simulations, the accessible system sizes were too small to overcome finite-size effects, whereas finite-temperature DMRG studies are hindered by the increasing size of the phonon Hilbert space as temperature increases.

[2] A few results exist for the thermodynamic properties of 1D spin-Peierls models [83, 84]. However, they are limited by their accuracy at low temperatures, in particular for the specific heat.

Using the directed-loop algorithm developed in this thesis, we are now able to calculate the specific heat for systems reaching $L = 162$ lattice sites. For this purpose, we derive a direct Monte Carlo estimator that recovers the specific heat from the distribution of vertices. We present results for the specific heat of the spinless Holstein model covering the entire parameter range from weak to strong coupling and from low to high phonon frequencies. In the adiabatic limit, we compare our results for the Holstein model with those obtained for the Su-Schrieffer-Heeger (SSH) model [8], another electron-phonon model with a different coupling mechanism.

In the following, we give a brief outline of this work.

In Chap. 2, we define the fermion-boson models studied in this thesis and introduce the path-integral formalism to derive a retarded fermionic interaction from a generic fermion-boson model. Using the concept of generating functionals, we show how bosonic observables can be recovered from fermionic correlation functions. In particular, we specify sum rules for the phonon propagator and the total energy of the Holstein model.

In Chap. 3, we present the action-based QMC approach to retarded interactions. After discussing the basics of Monte Carlo sampling, we introduce a generic framework to formulate QMC methods from a perturbation expansion of the path integral. Based on this, we give an overview of three methods that can be used to simulate retarded interactions: the CT-INT method, the worm algorithm, and the directed-loop algorithm. We continue with a derivation of bosonic QMC estimators that use the information contained in the Monte Carlo configurations. Finally, we provide a detailed description of the directed-loop QMC method developed in this work. We show test results for the spinless Holstein model and discuss possible generalizations to other models.

In Chap. 4, we show applications to the thermodynamic and spectral properties of Peierls chains. First, we consider the adiabatic limit where we briefly discuss the Peierls instability as well as symmetry-protected topological states in Peierls systems. We use a classical Monte Carlo method to calculate the specific heat of the spinless Holstein and SSH models. With this method, spectral functions can be obtained directly on the real-frequency axis. We explain the specific heat data by analyzing the temperature dependence of the single- and two-particle spectra. The effects of quantum lattice fluctuations on the specific heat of the spinless Holstein model are studied in the subsequent section. We first discuss the specific heat for a fixed coupling as a function of the phonon frequency, then the adiabatic and antiadiabatic regimes as a function of the electron-phonon coupling. To explain the low-temperature features in the adiabatic regime, we consider the electron and phonon spectral functions across the Peierls transition.

In Chap. 5, we conclude and give an outlook on prospective algorithmic developments, possible applications, and future work on thermodynamic properties of Peierls systems.

Additional information is provided in the Appendix. In App. A, we show how retarded interactions for fermion-boson models can be obtained directly from the interaction picture without referring to the path integral. In App. B, we define the electron and phonon spectral functions for the Holstein model, derive a relation between the phonon spectral function and the dynamic charge structure factor, and outline sum rules for the total energy. Appendix C deals with different approaches to calculate the specific

heat from QMC simulations. On the one hand, we derive a direct QMC estimator for the specific heat of the Holstein model. On the other hand, we outline a maximum entropy approach that calculates the specific heat from fitting and differentiating the total energy. Finally, we discuss finite-size effects for the Holstein model and the SSH model in the adiabatic limit.

Much of the work presented in this thesis is based on the publications [P2–P4] (see p. 121). In particular, the presentation of fermion-boson models and the path-integral formalism in Chap. 2 as well as the discussion of the perturbation expansion, the CT-INT method, and the measurement of bosonic observables from the Monte Carlo configurations in Chap. 3 rely on Ref. [P3]. The discussion of the directed-loop algorithm for retarded interactions in Chap. 3 is based on Ref. [P2] and its supplemental material. The results for thermodynamic and spectral properties of adiabatic Peierls chains presented in Chap. 4 were published in Ref. [P4], whereas the study of combined effects of thermal and quantum lattice fluctuations on the spinless Holstein model have not been published so far. Results for the phonon spectrum rely on Ref. [P3] and the appendix on spectral functions is based on Refs. [P3, P5].

2. Fermion-boson models and retarded interactions

In principle, quantum many-particle physics in thermal equilibrium does not include the notion of time. However, to solve the partition function in the path-integral formulation, one introduces an artificial time axis called the imaginary-time axis that ranges from zero to $\beta = 1/k_{\mathrm{B}}T$. Actions obtained in this way are instantaneous, though. Retarded interactions, i.e., interactions that are nonlocal in imaginary time, usually arise when dividing the physical system into two subsystems: the subsystem of interest is still called the system, whereas the other part is referred to as the bath. A coupling between system and bath allows for particle or energy exchange. From the perspective of the system, the coupling to the bath then looks like a self-interaction that is nonlocal in time. This effect becomes manifest in the path-integral formalism. Starting from a bilinear action in the bath fields, the latter can be integrated out analytically which leads to a retarded interaction in the system. Many physical examples can be described by retarded interactions originating from the coupling to a bath: In the Kondo problem, the local spin of an impurity is screened by the surrounding Fermi sea that acts as a bath [85]. Realistic modeling of physical systems at low energies requires the inclusion of screening effects from high-energy bands which leads to retarded interactions [78]. The coupling of a physical system to bosonic or fermionic baths is also studied in the context of quantum dissipative systems, both in equilibrium and nonequilibrium [86]. In this work, we are particularly interested in fermionic systems that couple locally to a bosonic bath, more precisely, in electron-phonon coupled systems. Here, the effect of the phonons on the electronic system can be described by a retarded electronic interaction that is mediated by the free phonon propagator.

The goal of this chapter is to introduce the path-integral formalism for a generic fermion-boson model in order to prepare our discussion of action-based QMC methods in Chap. 3. We briefly define two fermion-boson models that fall into the class of the generic model, i.e., the Holstein model and the SSH model. Their physical properties will be discussed in detail in Chap. 4. For the generic fermion-boson model, we derive a retarded fermionic interaction by integrating out the bosons. The result is specified for the electron-phonon models considered in this thesis. Furthermore, we show how bosonic observables can be recovered from fermionic correlation functions using the concept of generating functionals. In particular, we derive sum rules for the phonon propagator and the phonon energies of the Holstein model.

Our presentation in this chapter is based on Ref. [P3]. Although we restrict ourselves to fermion-boson models with a single bosonic mode, the basic formalism derived in this chapter can be easily generalized to other systems that couple to a bosonic bath.

For example, the fermionic degrees of freedom can be replaced by bosons or spins, but also different types of boson propagators are possible. To keep the notation as simple as possible, we only consider 1D models. Generalizations to higher dimensions are straightforward.

2.1. Fermion-boson models

The 1D electron-phonon models studied in this thesis belong to a larger class of fermion-boson Hamiltonians of the form

$$\hat{H} = \hat{H}_\mathrm{f} + \underbrace{\sum_q \omega_q \hat{b}_q^\dagger \hat{b}_q}_{\hat{H}_\mathrm{b}} + \underbrace{\sum_q \left(\gamma_q \hat{\varrho}_q \hat{b}_q^\dagger + \bar{\gamma}_q \hat{\varrho}_q^\dagger \hat{b}_q\right)}_{\hat{H}_\mathrm{fb}} \tag{2.1}$$

which consist of a general fermionic part $\hat{H}_\mathrm{f}$ and a remainder that is quadratic in the bosonic creation and annihilation operators $\hat{b}_q^\dagger$, $\hat{b}_q$. The bosonic part $\hat{H}_\mathrm{b}$ is described by harmonic oscillators with a general dispersion ω_q, whereas $\hat{H}_\mathrm{fb}$ contains the coupling to an arbitrary fermionic operator $\hat{\varrho}_q$ with coupling parameter γ_q (we also include the complex conjugate $\bar{\gamma}_q$). The sums in Eq. (2.1) run over momenta $q = 2\pi n/L$ with $n \in \{0, \ldots, L-1\}$. Here, L is the number of lattice sites. We set the lattice constant and $\hbar$ equal one and use periodic boundary conditions to define the momenta q.

Below, we define the Holstein model as well as the SSH model and map them to the generic form (2.1). For both models, the electronic part of the Hamiltonian is given by the nearest-neighbor hopping of spinful fermions with amplitude t,

$$\hat{H}_\mathrm{f} = -t \sum_i \underbrace{\sum_\sigma \left(\hat{c}_{i,\sigma}^\dagger \hat{c}_{i+1,\sigma} + \hat{c}_{i+1,\sigma}^\dagger \hat{c}_{i,\sigma}\right)}_{\hat{B}_{i,i+1}} . \tag{2.2}$$

Here, $\hat{B}_{i,i+1}$ is the electronic bond operator and $\hat{c}_{i,\sigma}^\dagger$, $\hat{c}_{i,\sigma}$ create or annihilate an electron at lattice site i with spin σ, respectively. The corresponding spinless models are obtained by dropping spin indices. The retarded interactions derived from the path integral only depend on the bosonic part $\hat{H}_\mathrm{b}$ and the type of fermion-boson coupling in $\hat{H}_\mathrm{fb}$, but not on the explicit choice of $\hat{H}_\mathrm{f}$, which could also include other terms like a Hubbard interaction. Therefore, we leave $\hat{H}_\mathrm{f}$ unspecified in the following.

2.1.1. Holstein model

As a first example of the generic model (2.1), we consider the Holstein molecular-crystal model [14, 15]

$$\hat{H} = \hat{H}_\mathrm{f} + \sum_i \left(\frac{1}{2M}\hat{P}_i^2 + \frac{K}{2}\hat{Q}_i^2\right) + g \sum_i \hat{Q}_i \, \hat{\rho}_i \, . \tag{2.3}$$

The phonons are described by local harmonic oscillators with displacements $\hat{Q}_i$ and momenta $\hat{P}_i$; M is the oscillator mass and K the spring constant. The displacements couple to the local charge density $\hat{\rho}_i = \sum_\sigma (\hat{n}_{i,\sigma} - 1/2)$ (here $\hat{n}_{i,\sigma} = \hat{c}^\dagger_{i,\sigma}\hat{c}_{i,\sigma}$) with coupling parameter g. The Holstein model follows from the generic model (2.1) by dropping the momentum dependence of the bosons, i.e., $\omega_q = \omega_0 = \sqrt{K/M}$ and $\gamma_q = \bar{\gamma}_q = \gamma = g/\sqrt{2M\omega_0}$, and assuming a density-displacement coupling so that $\hat{\varrho}_q = L^{-1/2}\sum_i e^{-\mathrm{i}qi}\hat{\rho}_i$.[1] We also introduce the dimensionless coupling parameter $\lambda = \gamma^2/(2\omega_0 t) = g^2/(4Kt)$.

The Holstein model is the central model studied in this thesis. We use it as an example to explain and develop QMC methods for retarded interactions in Chap 3. Furthermore, we study its thermodynamic and spectral properties in Chap. 4. The phase diagram in Fig. 4.1 shows that the spinless Holstein model undergoes a quantum phase transition between a Peierls insulating phase and a metallic Luttinger liquid phase. For further information on the physical properties of the model, see Chap. 4. In particular, Sec. 4.1.1 includes a definition of the adiabatic limit and a discussion of the Peierls instability.

2.1.2. Su-Schrieffer-Heeger model

As a second example, we consider the Su-Schrieffer-Heeger (SSH) model [8]

$$\hat{H} = \hat{H}_\mathrm{f} + \sum_i \left[\frac{1}{2M}\hat{P}_i^2 + \frac{K}{2}\left(\hat{Q}_{i+1} - \hat{Q}_i\right)^2\right] + \alpha\sum_i \left(\hat{Q}_{i+1} - \hat{Q}_i\right)\hat{B}_{i,i+1} \tag{2.5}$$

where the electrons couple to the phonons in the form of a modulation of the electronic hopping as a result of lattice distortions. The SSH model can be obtained from the generic Hamiltonian (2.1) by choosing acoustic phonons with dispersion $\omega_q = \omega_\pi \sin(q/2)$ and $\omega_\pi = 2\sqrt{K/M}$ [P6]. The coupling of the phonons to the bond operators leads to $\hat{\varrho}_q = L^{-1/2}\sum_i e^{-\mathrm{i}qi}\hat{B}_{i,i+1}$ and a complex coupling $\gamma_q = \alpha\left(e^{-\mathrm{i}q} - 1\right)/\sqrt{2M\omega_q}$.[2] For the SSH model, we define the dimensionless coupling $\lambda = 2|\gamma_q|^2/(\omega_q t) = \alpha^2/(Kt)$.

A similar model that is given by the Hamiltonian [87]

$$\hat{H} = \hat{H}_\mathrm{f} + \sum_i \left(\frac{1}{2M}\hat{P}_{i,i+1}^2 + \frac{K}{2}\hat{Q}_{i,i+1}^2\right) + \alpha\sum_i \hat{Q}_{i,i+1}\hat{B}_{i,i+1} \tag{2.7}$$

[1] For the Holstein model, the displacement and momentum operators can be transformed into the second-quantized creation and annihilation operators via the relations

$$\hat{Q}_i = \frac{1}{\sqrt{2M\omega_0}}\left(\hat{b}_i^\dagger + \hat{b}_i\right), \qquad \hat{P}_i = \mathrm{i}\sqrt{\frac{M\omega_0}{2}}\left(\hat{b}_i^\dagger - \hat{b}_i\right). \tag{2.4}$$

Then, the parameters for the generic Hamiltonian (2.1) can be read off immediately. We omit the zero-point energy in Eq. (2.1).

[2] For the SSH model, the bosonic operators in Eq. (2.5) must first be Fourier transformed into momentum space before we can apply the relations

$$\hat{Q}_q = \frac{1}{\sqrt{2M\omega_q}}\left(\hat{b}_{-q}^\dagger + \hat{b}_q\right), \qquad \hat{P}_q = \mathrm{i}\sqrt{\frac{M\omega_q}{2}}\left(\hat{b}_q^\dagger - \hat{b}_{-q}\right). \tag{2.6}$$

describes the coupling of the electronic bond operators $\hat{B}_{i,i+1}$ to a single displacement $\hat{Q}_{i,i+1}$ instead of the difference $\left(\hat{Q}_{i+1} - \hat{Q}_i\right)$. In contrast to the original SSH model, the phonons are defined at the bonds between two lattice sites i and $i+1$ and rather describe the dynamics of the bonds than the fluctuations of the atom positions. The model has optical phonons with frequency $\omega_q = \omega_0 = \sqrt{K/M}$ and is therefore called the optical SSH model. It follows from the generic Hamiltonian (2.1) by choosing the constant coupling $\gamma_q = \bar{\gamma}_q = \gamma = \alpha/\sqrt{2M\omega_0}$ to the bond operators $\hat{\varrho}_q = L^{-1/2} \sum_i e^{-\mathrm{i}qi} \hat{B}_{i,i+1}$. Formally, the optical SSH model is very similar to the Holstein model, only $\hat{\varrho}_q$ is chosen differently.

The SSH model was originally introduced for the theoretical study of soliton excitations in conjugated polymers [8]. In Chap. 4, we briefly discuss solitons in the context of symmetry-protected topological insulators and investigate how they appear in the adiabatic limit of the spinless SSH model as a consequence of thermal fluctuations. Moreover, we use, in particular, the optical SSH model as a further example to demonstrate the applicability of the action-based QMC approach.

2.2. Path-integral formalism and retarded interactions

The path integral provides a general approach to derive retarded interactions for systems coupled to a bosonic bath. We derive an effective fermionic action for the generic fermion-boson model (2.1). With the help of generating functionals, any bosonic observable can be recovered from fermionic correlation functions. In particular, we derive sum rules for the phonon propagator and the total energy of the Holstein model.[3]

2.2.1. Effective fermionic action for the bosons

The grand-canonical partition function of a fermion-boson coupled many-particle system can be represented by the functional field integral

$$Z = \int \mathcal{D}(\bar{b}, b) \int \mathcal{D}(\bar{c}, c)\, e^{-\mathcal{S}[\bar{b},b,\bar{c},c]}\,, \tag{2.8}$$

where $\mathcal{D}(\bar{b}, b)$ $[\mathcal{D}(\bar{c}, c)]$ is the bosonic [fermionic] integration measure and $\mathcal{S}$ the action of the total system. We use the coherent-state representation $\hat{b}\,|b\rangle = b\,|b\rangle$ with complex variables b for the bosons, and $\hat{c}\,|c\rangle = c\,|c\rangle$ with anticommuting Grassmann variables c for the fermions. The bosonic and fermionic fields are functions of imaginary time τ and fulfill the boundary conditions $b(\beta) = b(0)$ and $c(\beta) = -c(0)$. Note that in the field-integral approach time ordering is implicit. For further details on coherent states and the functional field integral, see Refs. [89, 90].

[3] Note that the path-integral formalism is not essential to derive retarded interactions. In App. A, we describe an alternative way to obtain retarded interactions directly from the Hamiltonian-based interaction picture. In this approach, the bosonic degrees of freedom are eliminated by applying Wick's theorem to the bosonic correlation functions that appear in the interaction expansion. Moreover, instead of generating functionals one can also use the equations of motion to derive sum rules for bosonic observables [88]. However, in our opinion the path-integral approach is more elegant and much simpler. Therefore, we use the path integral in the course of this work.

For the generic fermion-boson model (2.1), the action $\mathcal{S}$ is split into the fermionic part

$$\mathcal{S}_\mathrm{f} = \int_0^\beta d\tau \sum_{i\sigma} \{\bar{c}_{i,\sigma}(\tau)\,[\partial_\tau - \mu]\,c_{i,\sigma}(\tau) + H_\mathrm{f}[\bar{c}_{i,\sigma}(\tau), c_{i,\sigma}(\tau)]\} \tag{2.9}$$

and the remainder containing the free-boson part and the interaction,

$$\mathcal{S}_\mathrm{b} + \mathcal{S}_\mathrm{fb} = \int_0^\beta d\tau \sum_q \left\{ \bar{b}_q(\tau)\,[\partial_\tau + \omega_q]\,b_q(\tau) + \gamma_q\,\varrho_q(\tau)\,\bar{b}_q(\tau) + \bar{\gamma}_q\,\bar{\varrho}_q(\tau)\,b_q(\tau) \right\} . \tag{2.10}$$

Then, the partition function takes the form

$$Z = \int \mathcal{D}(\bar{c}, c)\, e^{-\mathcal{S}_\mathrm{f}[\bar{c},c]} \underbrace{\int \mathcal{D}(\bar{b}, b)\, e^{-\mathcal{S}_\mathrm{b}[\bar{b},b] - \mathcal{S}_\mathrm{fb}[\bar{b},b,\bar{c},c]}}_{= Z_\mathrm{b}\, e^{-\mathcal{S}_\mathrm{ret}[\bar{c},c]}} . \tag{2.11}$$

Because the action is quadratic in the bosonic fields, they can be integrated out exactly [60], leading to an effective fermionic interaction

$$\mathcal{S}_\mathrm{ret} = -\sum_q \frac{|\gamma_q|^2}{\omega_q} \iint_0^\beta d\tau d\tau'\, \bar{\varrho}_q(\tau)\, P_q(\tau - \tau')\, \varrho_q(\tau') \tag{2.12}$$

mediated by the noninteracting bosonic Green's function $P_q(\tau - \tau') = \omega_q \langle \bar{b}_q(\tau) b_q(\tau') \rangle_\mathrm{b}$. Here, we introduced the expectation value with respect to the free-boson part, $\langle O \rangle_\mathrm{b} = Z_\mathrm{b}^{-1} \int \mathcal{D}(\bar{b}, b)\, e^{-\mathcal{S}_\mathrm{b}} O$, where $Z_\mathrm{b} = \int \mathcal{D}(\bar{b}, b)\, e^{-\mathcal{S}_\mathrm{b}}$ is the partition function of free bosons. For $0 \le \tau < \beta$, $P_q(\tau)$ is given by

$$P_q(\tau) = \omega_q \frac{e^{-\omega_q \tau}}{1 - e^{-\omega_q \beta}} \tag{2.13}$$

and we impose periodic boundary conditions $P_q(\tau + \beta) = P_q(\tau)$. With the factor of ω_q, the adiabatic and antiadiabatic limits of $P_q(\tau)$ are

$$\lim_{\omega_q \to 0} P_q(\tau) = \frac{1}{\beta} , \qquad \lim_{\omega_q \to \infty} P_q(\tau) = \delta(\tau) . \tag{2.14}$$

In general, the bosonic propagator $P_q(\tau)$ mediates a nonlocal interaction that drops off exponentially in imaginary time. However, in the adiabatic limit $\omega_q \to 0$ the interaction becomes long-ranged, whereas in the antiadiabatic limit $\omega_q \to \infty$ it becomes instantaneous.

Retarded interactions for electron-phonon models

For the Holstein model, the effective interaction (2.12) takes the form

$$\mathcal{S}_\mathrm{ret} = -2\lambda t \iint_0^\beta d\tau d\tau' \sum_i \rho_i(\tau)\, P(\tau - \tau')\, \rho_i(\tau') , \tag{2.15}$$

which is diagonal in real space. Because the free phonon propagator is now local in space, we replaced $P_q(\tau) \to P(\tau)$. For the optical SSH model, the retarded interaction is very similar and given by

$$\mathcal{S}_{\mathrm{ret}} = -\frac{\lambda t}{2} \iint_0^\beta d\tau d\tau' \sum_i B_{i,i+1}(\tau)\, P(\tau-\tau')\, B_{i,i+1}(\tau')\,. \tag{2.16}$$

However, for the SSH model with acoustic phonons, we obtain a nonlocal interaction in space and time, i.e.,

$$\mathcal{S}_{\mathrm{ret}} = -\frac{\lambda t}{2} \iint_0^\beta d\tau d\tau' \sum_{ij} B_{i,i+1}(\tau)\, P_{ij}(\tau-\tau')\, B_{j,j+1}(\tau')\,, \tag{2.17}$$

where $P_{ij}(\tau) = L^{-1}\sum_q e^{-\mathrm{i}q(i-j)} P_q(\tau)$. While $P_q(\tau) > 0$ is always satisfied, $P_{ij}(\tau)$ obtains negative contributions for $i \neq j$ if we consider an arbitrary dispersion ω_q that is not constant [P6].

2.2.2. Correlation functions and generating functionals

The expectation value of an arbitrary observable $O[\bar{b}, b, \bar{c}, c]$ takes the form

$$\left\langle O[\bar{b}, b, \bar{c}, c]\right\rangle = \frac{\int \mathcal{D}(\bar{b}, b) \int \mathcal{D}(\bar{c}, c)\, O[\bar{b}, b, \bar{c}, c]\, e^{-\mathcal{S}}}{\int \mathcal{D}(\bar{b}, b) \int \mathcal{D}(\bar{c}, c)\, e^{-\mathcal{S}}}\,. \tag{2.18}$$

If the observable only depends on the fermionic fields, the bosonic parts of $\mathcal{S}$ can be integrated out exactly, both in the numerator and in the denominator of Eq. (2.18). Then, $O[\bar{c}, c]$ can be calculated directly from the retarded interaction, i.e.,

$$\langle O[\bar{c}, c]\rangle = \frac{\int \mathcal{D}(\bar{c}, c)\, O[\bar{c}, c]\, e^{-\mathcal{S}_{\mathrm{f}} - \mathcal{S}_{\mathrm{ret}}}}{\int \mathcal{D}(\bar{c}, c)\, e^{-\mathcal{S}_{\mathrm{f}} - \mathcal{S}_{\mathrm{ret}}}}\,. \tag{2.19}$$

To calculate an observable $O[\bar{b}, b, \bar{c}, c]$ that also depends on the bosonic fields, we add the source term

$$\mathcal{S}_{\mathrm{source}} = -\int_0^\beta d\tau \sum_q \left[\eta_q(\tau)\, \bar{b}_q(\tau) + \bar{\eta}_q(\tau)\, b_q(\tau)\right] \tag{2.20}$$

to the action in the numerator of Eq. (2.18). Then, the bosonic fields contained in the observable can be expressed as functional derivatives with respect to the complex source fields $\eta_q(\tau)$ and $\bar{\eta}_q(\tau)$. After integrating out the bosons (including the source term), the source fields appear in $\mathcal{S}_{\mathrm{ret}}$, i.e.,

$$\mathcal{S}_{\mathrm{ret}}^{\mathrm{source}} = -\sum_q \frac{|\gamma_q|^2}{\omega_q} \iint_0^\beta d\tau d\tau' \left[\bar{\varrho}_q(\tau) - \bar{\gamma}_q^{-1}\bar{\eta}_q(\tau)\right] P_q(\tau-\tau') \left[\varrho_q(\tau') - \gamma_q^{-1}\eta_q(\tau')\right]\,, \tag{2.21}$$

and Eq. (2.18) becomes

$$\left\langle O[\bar{b},b,\bar{c},c]\right\rangle = \lim_{\bar{\eta},\eta\to 0} \frac{\int \mathcal{D}(\bar{c},c)\, O[\frac{\delta}{\delta\bar{\eta}},\frac{\delta}{\delta\eta},\bar{c},c]\, e^{-\mathcal{S}_{\mathrm{f}}-\mathcal{S}_{\mathrm{ret}}^{\mathrm{source}}}}{\int \mathcal{D}(\bar{c},c)\, e^{-\mathcal{S}_{\mathrm{f}}-\mathcal{S}_{\mathrm{ret}}}} \,. \tag{2.22}$$

As a result, any bosonic observable can be recovered from a higher-order fermionic correlation function.

2.2.3. Bosonic observables for the Holstein model

In the following, we illustrate the use of generating functionals for the Holstein model.[4] To express bosonic observables in terms of the displacements $q_i(\tau)$ or the momenta $p_i(\tau)$ we rewrite the source term (2.20) as

$$\mathcal{S}_{\mathrm{source}} = -\int_0^\beta d\tau \sum_i \left[\xi_i(\tau)\, q_i(\tau) + \zeta_i(\tau)\, p_i(\tau)\right] , \tag{2.23}$$

with real fields $\xi_i(\tau)$ and $\zeta_i(\tau)$. Transformation of the source fields in Eq. (2.21) leads to the action

$$\mathcal{S}_{\mathrm{ret}}^{\mathrm{source}} = \mathcal{S}_{\mathrm{ret}} + \mathcal{S}_{\xi\rho}^{+} + \mathcal{S}_{\xi\xi}^{+} + \mathcal{S}_{\zeta\rho}^{-} + \mathcal{S}_{\zeta\zeta}^{+} + \mathcal{S}_{\xi\zeta}^{-} , \tag{2.24}$$

where the individual contributions are given by

$$\mathcal{S}_{\mu\nu}^{\pm} = -\alpha_{\mu\nu} \iint_0^\beta d\tau d\tau' \sum_i \mu_i(\tau)\, P_{\pm}(\tau-\tau')\, \nu_i(\tau') \tag{2.25}$$

with $\alpha_{\xi\rho} = -2\sqrt{\lambda t/K}$, $\alpha_{\xi\xi} = 1/(2K)$, $\alpha_{\zeta\rho} = 2\mathrm{i}\sqrt{M\lambda t}$, $\alpha_{\zeta\zeta} = M/2$, and $\alpha_{\xi\zeta} = \mathrm{i}/\omega_0$. Here, we defined the phonon propagators

$$P_{\pm}(\tau) = \frac{1}{2}\left[P(\tau) \pm P(\beta-\tau)\right] , \tag{2.26}$$

corresponding to $P_{+}(\tau-\tau') = K\,\langle q_i(\tau)\, q_i(\tau')\rangle_{\mathrm{b}} = M^{-1}\langle p_i(\tau)\, p_i(\tau')\rangle_{\mathrm{b}}$ and $P_{-}(\tau-\tau') = -\mathrm{i}\,\omega_0\,\langle q_i(\tau)\, p_i(\tau')\rangle_{\mathrm{b}}$.

Phonon propagator

With the help of the generating functionals in Eqs. (2.24) and (2.25), we get access to the phonon propagators

$$D_Q(i-j,\tau-\tau') = K\left\langle q_i(\tau)\, q_j(\tau')\right\rangle = P_{+}(\tau-\tau')\,\delta_{i,j} + X_{ij}^{++}(\tau,\tau') , \tag{2.27}$$

$$D_P(i-j,\tau-\tau') = \frac{1}{M}\left\langle p_i(\tau)\, p_j(\tau')\right\rangle = P_{+}(\tau-\tau')\,\delta_{i,j} + X_{ij}^{--}(\tau,\tau') \tag{2.28}$$

[4] The sum rules derived below also apply to the optical SSH model (2.7) after substituting $\rho_i(\tau) \to B_{i,i+1}(\tau)$ and $\lambda \to \lambda/4$.

consisting of the free propagator $P_+(\tau - \tau')$ and the interaction contributions

$$X_{ij}^{\pm\pm}(\tau,\tau') = 4\lambda t \iint_0^\beta d\tau_1 d\tau_1' \, P_\pm(\tau - \tau_1) \left\langle \rho_i(\tau_1)\rho_j(\tau_1') \right\rangle P_\pm(\tau_1' - \tau') \,. \tag{2.29}$$

The phonon propagators of the Holstein model are completely determined by the dynamic charge-charge correlation function. A relation between the corresponding spectral functions is derived in App. B.2.

Total energy

The total energy of the Holstein model, $E = E_{\mathrm{el}} + E_{\mathrm{ph}} + E_{\mathrm{ep}}$, is the sum of the electronic part E_{el}, the phonon part E_{ph}, and the electron-phonon interaction term E_{ep}. We further split $E_{\mathrm{ph}} = E_{\mathrm{ph}}^{\mathrm{kin}} + E_{\mathrm{ph}}^{\mathrm{pot}}$ into the kinetic and potential parts of the phonon energy. With the help of generating functionals, the bosonic contributions to the total energy can be calculated from the local charge-charge correlation function $C_\rho(\tau - \tau') = \sum_i \langle \rho_i(\tau)\rho_i(\tau') \rangle$ via the sum rules

$$E_{\mathrm{ph}}^{\mathrm{kin}} = \frac{E_{\mathrm{ph}}^0}{2} - 2\lambda t \iint_0^\beta d\tau d\tau' P_-(\tau)\, P_-(\tau')\, C_\rho(\tau - \tau') \,, \tag{2.30}$$

$$E_{\mathrm{ph}}^{\mathrm{pot}} = \frac{E_{\mathrm{ph}}^0}{2} + 2\lambda t \iint_0^\beta d\tau d\tau' P_+(\tau)\, P_+(\tau')\, C_\rho(\tau - \tau') \,, \tag{2.31}$$

$$E_{\mathrm{ep}} = -4\lambda t \int_0^\beta d\tau \, P_+(\tau)\, C_\rho(\tau) \,. \tag{2.32}$$

Here, $E_{\mathrm{ph}}^0 = L\, P_+(0)$ is the contribution of free phonons at $\lambda = 0$. $E_{\mathrm{ph}}^{\mathrm{pot}}$ and $E_{\mathrm{ph}}^{\mathrm{kin}}$ follow from the phonon propagators (2.27) and (2.28) by fixing the interaction to $X_{ii}^{\pm\pm}(0,0)$. In Appendix B.3, we provide further information on the relation between the bosonic observables and the dynamic charge structure factor.

3. Action-based quantum Monte Carlo approach to retarded interactions

During the last decades, many QMC methods have been developed that avoid a Trotter discretization of imaginary time and are therefore regarded as numerically exact methods. For the development of different QMC methods, choosing the right representation of the partition function played an important role. Many QMC methods are based on a Hamiltonian formulation. For example, the SSE representation [82] was established as a high-temperature expansion of the partition function, i.e., an expansion in the full Hamiltonian, where a Monte Carlo configuration is given by a sequence of operators that does not even contain an explicit notion of imaginary time. By contrast, the worm algorithm [53] was formulated in the interaction-expansion representation where the imaginary-time evolution of operators requires an explicit time labeling of kinks appearing in a world-line configuration. Later, it has been recognized that the interaction-expansion representation provides a general framework for many QMC methods [56, 91]. With the development of determinantal continuous-time QMC methods that are predominantly used as impurity solvers [67,68,75] in DMFT applications, an action-based formulation of QMC methods was promoted. Again, these methods rely on an interaction-expansion representation, but now in a path-integral formulation. In contrast to the Hamiltonian-based methods used before, the flexibility of the path-integral approach allowed an easy implementation of retarded interactions that arise from the coupling to a bosonic bath or from dynamical screening. Important applications included the simulation of lattice fermion-boson models using the CT-INT method [70] and extended DMFT calculations for screening effects in impurity models [76, 79, 80]. However, world-line methods had already been used before to simulate retarded interactions for the polaron problem [61–66]. Recently, the worm algorithm has also been applied to retarded interactions at finite band fillings [72].

In this chapter, we give an introduction to the action-based QMC approach to retarded interactions. We restrict ourselves to exact methods that can be used to simulate fermion-boson models on a lattice, i.e., the CT-INT method, the worm algorithm, and the directed-loop algorithm. These methods have in common that they sample interaction vertices in a perturbation expansion, but differ in the choice which part of the action is regarded as the perturbation. An apparent disadvantage of the action-based approach is the loss of direct access to bosonic observables. For those methods that expand in the retarded interaction we show that bosonic observables can be recovered efficiently from the distribution of vertices. Furthermore, we develop a new QMC algorithm with directed-loop updates that is based on the SSE representation and solves the autocorrelation problem for 1D fermion-boson models. Although we restrict ourselves

to fermion-boson models, the concepts discussed for world-line methods, i.e., the worm algorithm and the directed-loop algorithm, also apply to bosonic or spin models coupled to a bosonic bath. Accordingly, these world-line algorithms can also be used to simulate bosonic models with retarded interactions in higher spatial dimensions.

After a brief introduction to the basics of Monte Carlo sampling in Sec. 3.1, we give an overview of QMC methods for retarded interactions in Sec. 3.2 and show how they follow from a unified picture of the perturbation expansion. This section already includes a short description of the directed-loop algorithm developed in this thesis. In Sec. 3.3, we show for the CT-INT method how bosonic observables can be recovered from the distribution of vertices. Finally, in Sec. 3.4 we give a detailed description of the directed-loop algorithm, demonstrate its efficiency, and discuss possible extensions to other models. Parts of this chapter are based on Refs. [P2, P3].

3.1. Monte Carlo basics

The Monte Carlo method is a stochastic approach to calculate high-dimensional sums and integrals as they occur for example in the partition function of a many-particle system. Its efficiency relies on the central-limit theorem which ensures that the statistical error of an observable scales inversely with the square root of the number of samples. In particular, the sampling error is independent of the dimension of the integrals. In the following, we briefly review the main concepts of Monte Carlo sampling using the example of the partition function. Our presentation follows Refs. [68, 92, 93].

3.1.1. From the partition function to Monte Carlo sampling

In the Monte Carlo language, the partition function of a physical system is written as a sum over configurations C and a weight $W(C)$, i.e.,

$$Z = \sum_C W(C)\,. \tag{3.1}$$

Each configuration C consists of a set of variables that can either be discrete or continuous. Hence, the $\sum$ symbol in Eq. (3.1) may in general contain sums over discrete variables and integrals over continuous ones. In a classical system, the Monte Carlo weight is often given by the Boltzmann factor $W(C) = \exp[-\beta E(C)]$, where a configuration is represented by a point in phase space and $E(C)$ is the corresponding energy. Even for a quantum system, a mapping to the form (3.1) is always possible. Using the path-integral formulation of the partition function, the quantum many-particle problem is mapped to a classical problem with an additional dimension for imaginary time.

Although the mapping of the partition function to the form (3.1) is often used to identify the weight $W(C)$, the defining equation for the Monte Carlo sampling is the expectation value of an observable. It is given by

$$\langle O \rangle = \frac{1}{Z} \sum_C W(C)\, O(C)\,, \tag{3.2}$$

where $O(C)$ is the contribution to the observable for a given configuration. The precise form of $O(C)$ depends on the details of the Monte Carlo method used and can be very different for different methods. If $W(C) > 0$, we can identify the probability distribution $p(C) = W(C)/Z$ that is sampled in the Monte Carlo process. However, especially for fermionic systems $W(C)$ may have negative contributions which leads to the *negative sign problem*. A positive weight can then be obtained by a simple reweighting:

$$\langle O \rangle = \frac{\sum_C |W(C)|\, O(C)\, s(C)}{\sum_C |W(C)|\, s(C)} = \frac{\langle Os \rangle_{|W|}}{\langle s \rangle_{|W|}} \,. \tag{3.3}$$

Here, we take the expectation value with respect to the absolute value of the weight and add the sign $s(C)$ to the observable. In the presence of a severe sign problem, Monte Carlo simulations usually scale exponentially [94].

Equation (3.2) can be estimated using *importance sampling*: We draw M samples $C^{(i)}$, $i \in \{1, \ldots, M\}$, from the distribution $p(C)$ and obtain the sample mean

$$\bar{O} = \frac{1}{M} \sum_{i=1}^{M} O_i \,. \tag{3.4}$$

Here, we have introduced the short-hand notation $O_i = O(C^{(i)})$. The estimator $\bar{O}$ itself is a random variable that converges to the exact result $\langle O \rangle$ in the limit $M \to \infty$. Its variance can be estimated from the sample variance

$$\sigma_{\bar{O}}^2 = \frac{1}{M-1} \sum_{i=1}^{M} \left(O_i - \bar{O} \right)^2 \tag{3.5}$$

if all samples are statistically independent. Then, the error becomes $(\sigma_{\bar{O}}^2/M)^{1/2}$ for large M. However, the true error can be much larger if the samples are correlated (cf. Sec. 3.1.3).

3.1.2. Markov chains and the Metropolis-Hastings algorithm

There are different ways of generating random configurations from a probability distribution. If $p(C)$ is known, we can often use *direct sampling* to generate independent samples, which is very efficient in low-dimensional phase spaces. In Sec. 3.4.2, we will use direct sampling to generate random numbers distributed according to the phonon propagator. For the high-dimensional phase space of the partition function, we use a different approach called *Markov chain sampling*. It is based on a stochastic process that generates a new configuration $C^{(t+1)}$ only from the present configuration $C^{(t)}$ with the transition probability $T(C^{(t)} \to C^{(t+1)})$. Thereby, an artificial time t is introduced that labels the configurations. To keep the notation as simple as possible, we drop the time labels in the following. Conservation of probability requires $\sum_{C'} T(C \to C') = 1$. The Markov chain starts from an arbitrary initial distribution and converges to the stationary distribution $W(C)$ if two conditions are fulfilled: ergodicity and balance. *Ergodicity*

means that it is possible to reach any configuration C' from C in a finite number of Markov steps, whereas the *balance* condition

$$\sum_C W(C)\, T(C \to C') = W(C') \tag{3.6}$$

ensures that the Markov process converges to the stationary distribution $W(C)$. Note that for a Markov process the normalization of the probability distribution need not be known. For example, to sample Eq. (3.2) we only need the weight $W(C)$ but not the normalization factor Z. In practice, it is often easier to work with the *detailed-balance* condition

$$W(C)\, T(C \to C') = W(C')\, T(C' \to C) \tag{3.7}$$

that directly leads to Eq. (3.6) by summing both sides of the equation over C.

Markov chains provide a general framework to sample the weight $W(C)$. However, one still has to find an algorithm defined by the transition probabilities $T(C \to C')$. A particular choice is given by the *Metropolis-Hastings algorithm* [95, 96]. In this algorithm, the transition probability is split into a proposal probability $T_0(C \to C')$ and an acceptance probability $A(C \to C')$ so that $T(C \to C') = T_0(C \to C')\, A(C \to C')$. While the proposal probability is chosen in advance, the acceptance follows from the Metropolis choice

$$A(C \to C') = \min[1, R(C \to C')]\,, \quad R(C \to C') = \frac{W(C')\, T_0(C' \to C)}{W(C)\, T_0(C \to C')}\,, \tag{3.8}$$

which fulfills the detailed balance condition (3.7).

3.1.3. Autocorrelation times

While Markov chain sampling yields high acceptance rates, subsequent configurations are usually strongly correlated. We have to distinguish between two issues: the equilibration time of the Markov chain towards equilibrium and the autocorrelation time between subsequent measurements in equilibrium. Both time scales are usually captured by the normalized autocorrelation function [93]

$$A_O(t) = \frac{\frac{1}{M-t}\sum_{i=1}^{M-t} O_i O_{i+t} - \bar{O}^2}{\frac{1}{M}\sum_{i=1}^{M} O_i^2 - \bar{O}^2}\,. \tag{3.9}$$

Typically, $A_O(t)$ decays exponentially at large times [93], which defines the exponential autocorrelation time

$$\tau_{\mathrm{exp},O} = \limsup_{t\to\infty} \frac{t}{-\log|A_O(t)|} \tag{3.10}$$

for the observable O. The relaxation time for the slowest mode in the system is then defined as $\tau_{\mathrm{exp}} = \sup_O \tau_{\mathrm{exp},O}$, which sets an upper bound for the equilibration time. For

each observable, we can also define the integrated autocorrelation time

$$\tau_{\mathrm{int},O} = \frac{1}{2} + \sum_{t=1}^{\infty} A_O(t)\,, \tag{3.11}$$

which controls the statistical error of the observable O once equilibrium is reached. If the samples are statistically independent, $\tau_{\mathrm{int},O} = 1/2$ and the variance of the estimator $\bar{O}$ is related to the variance of the individual samples O_i via $\sigma^2_{\bar{O}} = \sigma^2_{O_i}/M$. In the presence of autocorrelations, the variance increases by a factor of $2\tau_{\mathrm{int},O}$ and becomes $\sigma^2_{\bar{O}} = 2\tau_{\mathrm{int},O}\,\sigma^2_{O_i}/M$. Therefore, the effective number of independent samples is reduced by a factor of $2\tau_{\mathrm{int},O}$. In practice, the integrated autocorrelation time can be estimated from a binning analysis (for details see Ref. [97]).

3.2. Quantum Monte Carlo methods for retarded interactions

In this section, we use the path-integral representation of the partition function to introduce a general framework for QMC methods that are based on a perturbation expansion and can be used to simulate retarded interactions of the form

$$\mathcal{S}_{\mathrm{ret}} = -2\lambda t \iint_0^\beta d\tau_1 d\tau_2 \sum_i \rho_i(\tau_1)\, P_+(\tau_1 - \tau_2)\, \rho_i(\tau_2)\,. \tag{3.12}$$

Depending on whether we perform the perturbation expansion in $\mathcal{S}_{\mathrm{ret}}$ or choose it as the unperturbed part of the action, we obtain different representations for QMC methods. We give an overview of three representations that follow from the general framework, i.e., the diagrammatic determinantal representation, the world-line representation, and the SSE representation. For simplicity, we only consider retarded interactions of the density-density type, as obtained from the Holstein model, but we also discuss extensions to other types of retarded interactions. The presentation in this section is based on Refs. [P2,P3].

3.2.1. Unified picture based on the perturbation expansion

The coherent-state path integral provides a general framework for the perturbation expansion that allows us to include retarded interactions. In this formulation, the grand-canonical partition function of an arbitrary fermionic action reads

$$Z = \int \mathcal{D}(\bar{c}, c)\, e^{-\mathcal{S}_0[\bar{c},c] - \mathcal{S}_1[\bar{c},c]}\,. \tag{3.13}$$

We split the action into the unperturbed part $\mathcal{S}_0$ and the perturbation $\mathcal{S}_1$. The perturbation expansion of Eq. (3.13) is

$$Z = \sum_{n=0}^{\infty} \frac{(-1)^n}{n!}\, Z_0\, \langle \mathcal{S}_1^n \rangle_0\,, \tag{3.14}$$

where we defined the expectation value with respect to the unperturbed system as $\langle O \rangle_0 = Z_0^{-1} \int \mathcal{D}(\bar{c}, c)\, e^{-\mathcal{S}_0} O$ with $Z_0 = \int \mathcal{D}(\bar{c}, c)\, e^{-\mathcal{S}_0}$.

The QMC methods considered below have in common that the expansion in Eq. (3.14) is calculated stochastically by sampling configurations of vertices. For this purpose, we write the perturbation in the vertex notation

$$\mathcal{S}_1 = -\sum_{\nu} w_\nu h_\nu \,. \tag{3.15}$$

A vertex is represented by an instance of the superindex ν that contains both discrete (e.g., lattice sites) and continuous variables (e.g., imaginary times), a weight w_ν, and the Grassmann representation of the operators $h_\nu[\bar{c}, c]$. We included an additional minus sign in the vertex to get rid of the trivial sign $(-1)^n$ in Eq. (3.14). The perturbation expansion becomes

$$Z = \sum_{n=0}^{\infty} \underbrace{\sum_{\nu_1 \dots \nu_n}}_{\sum_{C_n}} \underbrace{\frac{1}{n!}\, w_{\nu_1} \dots w_{\nu_n}\, Z_0 \, \langle h_{\nu_1} \dots h_{\nu_n} \rangle_0}_{\sum_\alpha W_\alpha(C_n)} \,. \tag{3.16}$$

The sum runs over the expansion order n, the ordered list of vertices $C_n = \{\nu_1, \dots, \nu_n\}$, and the variable α that allows an additional sampling of the trace in world-line QMC methods (see below). In the diagrammatic determinantal representation, we will omit this index. Hence, we can already identify the weight $W_\alpha(C_n)$ to be sampled in the Monte Carlo method.[1] The expectation value $\langle O \rangle = Z^{-1} \int \mathcal{D}(\bar{c}, c)\, e^{-\mathcal{S}_0 - \mathcal{S}_1} O$ of an observable O takes the form

$$\langle O \rangle = \sum_{n=0}^{\infty} \sum_{C_n} \sum_{\alpha} p_\alpha(C_n)\, \langle\!\langle O \rangle\!\rangle_{C_n, \alpha} \,, \tag{3.17}$$

where $p_\alpha(C_n) = W_\alpha(C_n) / \sum_n \sum_{C_n} \sum_\alpha W_\alpha(C_n)$ is the probability distribution sampled in the Monte Carlo simulation and $\langle\!\langle O \rangle\!\rangle_{C_n, \alpha}$ is the value of the observable for configuration C_n and label α. For a finite system size L and inverse temperature β, the perturbation expansion always converges [67]. As shown in Sec. 3.3.1, the average expansion order scales as $\langle n \rangle = -\langle \mathcal{S}_1 \rangle \sim \beta L$.

The perturbation expansion (3.16) provides a general framework to deal with retarded interactions in QMC simulations. However, the choice which part of the action is regarded as the perturbation $\mathcal{S}_1$ of the unperturbed part $\mathcal{S}_0$ leads to different QMC methods. The details of an algorithm are then determined by the specific representa-

[1] To be precise, $W_\alpha(C_n)$ is not exactly the Monte Carlo weight for continuous-time methods. Consider, for example, a vertex with variables $\nu = \{i, \tau\}$. To simplify the notation for the QMC methods and the vertex measurements discussed below, we put the integration measure $d\tau$ for the imaginary-time variable in $\sum_\nu = \sum_i \int d\tau$. This is correct as long as we consider properties of the perturbation expansion, but to obtain the true probability density for the Monte Carlo sampling, the integration measures of the vertices must be included in the Monte Carlo weight. Then, the weights are consistent with those obtained for QMC methods with a Trotter discretization of imaginary time. However, the additional $d\tau$ factors drop out of the Metropolis ratio in the end.

tion used to calculate the expectation value $\langle h_{\nu_1} \dots h_{\nu_n} \rangle_0$ required for the Monte Carlo weight $W_\alpha(C_n)$. In the following, we give an overview of different QMC approaches to simulate lattice models with retarded interactions. We introduce the different methods in their original representations. Afterwards we show how they apply to the simulation of retarded interactions using the example of the Holstein model. In this section, we already review the directed-loop QMC method developed in this thesis. However, the details of the algorithm will be discussed in Sec. 3.4.

3.2.2. Diagrammatic determinantal representation

The continuous-time QMC method in the interaction expansion, also known as the CT-INT method, was introduced by Rubtsov *et al.* [67] to simulate rather general fermionic actions. In this representation, $\mathcal{S}_0$ contains the single-particle terms of the action, i.e.,

$$\begin{aligned} \mathcal{S}_0 &= \int_0^\beta d\tau \sum_{ij\sigma} \bar{c}_{i,\sigma}(\tau) \left[(\partial_\tau - \mu)\, \delta_{i,j} - t_{i,j} \right] c_{j,\sigma}(\tau) \\ &= \iint_0^\beta d\tau d\tau' \sum_{ij\sigma} \bar{c}_{i,\sigma}(\tau)\, G_0^{-1}(i-j, \tau-\tau')\, c_{j,\sigma}(\tau')\,, \end{aligned} \tag{3.18}$$

where $t_{i,j} = t\,(\delta_{i,j+1} + \delta_{i,j-1})$ is the hopping matrix element between nearest neighbors and G_0 is the noninteracting single-particle Green's function. Because $\mathcal{S}_0$ is a bilinear in the fermionic fields, Wick's theorem applies to $\langle h_{\nu_1} \dots h_{\nu_n} \rangle_0$ for each configuration C_n [98]. Thus, the Monte Carlo weight $W(C_n)$ only involves the determinant $\det M(C_n) = \langle h_{\nu_1} \dots h_{\nu_n} \rangle_0$ of the $\mathcal{O}(n) \times \mathcal{O}(n)$ matrix $M(C_n)$. Its entries are noninteracting Green's functions with space-time arguments taken from the interaction vertices. Updates correspond to the addition or removal of individual vertices using the Metropolis-Hastings algorithm (cf. Sec. 3.1.2), and involve matrix-vector multiplications with $\mathcal{O}(n^2)$ operations. Since $\mathcal{O}(n)$ updates are necessary to reach an independent configuration, the algorithm scales as $\mathcal{O}(n^3)$. A clear advantage of the CT-INT method is that for any configuration C_n, Wick's theorem can be used to calculate any correlation function $\langle\!\langle O \rangle\!\rangle_{C_n}$ from the single-particle Green's function $\langle\!\langle \bar{c}_{i,\sigma}(\tau)\, c_{j,\sigma'}(\tau') \rangle\!\rangle_{C_n}$ [98].

While the technical details of the algorithm can be found in Refs. [68, 99], the idea behind the CT-INT method is very simple. For a given expansion order n, each vertex provides a set of Grassmann fields that is distributed over space and imaginary time. Because the perturbation expansion is performed around the noninteracting system, the contractions of the fermionic fields can be regarded as Feynman diagrams. In the end, for every expansion order n and configuration of vertices C_n, all the Feynman diagrams (including the disconnected ones) are taken into account in the determinant $\det M(C_n)$.

In principle, the diagrammatic determinantal representation is independent of the internal structure of the interaction vertex[2] so that the interaction can be nonlocal in space and imaginary time. The first application of the CT-INT method to retarded

[2] Of course, the possible interaction terms that can be simulated efficiently with the CT-INT method are limited by the fermionic sign problem.

interactions was performed by Assaad and Lang [70] considering the Holstein model

$$\mathcal{S}_1 = -\underbrace{\iint_0^\beta d\tau d\tau' \sum_{i\sigma\sigma' s}}_{\sum_\nu} \underbrace{\lambda t\, P_+(\tau-\tau')}_{w_\nu} \underbrace{\left[\rho_{i,\sigma}(\tau) - s\delta\right]\left[\rho_{i,\sigma'}(\tau') - s\delta\right]}_{h_\nu}, \tag{3.19}$$

which is still local in space. To establish a relation to the generic vertex notation in Eq. (3.15), we identified the constituents of the vertex in Eq. (3.19). In particular, each vertex contains the variables $\nu = \{i, \tau, \tau', \sigma, \sigma', s\}$, where the auxiliary Ising variable $s = \pm 1$ (and $\delta = 0.51$) is included to avoid the sign problem [70]. The formulation of the CT-INT method does not change in the presence of retarded interactions, only the acceptance rate for adding a new vertex is optimized by proposing the time difference $\tau - \tau'$ according to the phonon propagator $P_+(\tau - \tau')$ via inverse transform sampling. A pedagogical introduction to the CT-INT method with an emphasis on retarded interactions can be found in Ref. [100].

The CT-INT method was successfully applied to a number of 1D electron-phonon models including Holstein and Holstein-Hubbard models [32, 70, 71, 101–103, P3, P5], the optical SSH model [P6], the interplay between Holstein- and SSH-type coupling [104], and a long-range Fröhlich-type interaction [105]. Applications to the SSH model with acoustic phonons [P6] led to a severe sign problem caused by negative contributions of the free phonon propagator in the nonlocal interaction (2.17). Recently, the CT-INT method was successfully applied to the 2D Holstein model [P1].

In this work, we extend the CT-INT method with respect to measuring bosonic correlation functions from the distribution of vertices (see Sec. 3.3), and present results for the single-particle spectral functions of the spinless Holstein model (see Sec. 4.2.2).

3.2.3. World-line representation and worm algorithm

Another representation that is often used for QMC methods is the world-line representation. It is based on the idea that the partition function $Z = \sum_\alpha \langle\alpha| e^{-\beta\hat{H}} |\alpha\rangle$ describes the imaginary-time evolution of an initial state $|\alpha\rangle$ from time $\tau = 0$ to $\tau = \beta$. In the following, we explain the basic steps to arrive at a world-line representation of Z using the case of spinless fermions, where $|\alpha\rangle = |n_1, \ldots, n_L\rangle$ is given in the local occupation-number basis. The Hamiltonian consists of two types of operators that are distinguished by their effect on $|\alpha\rangle$: diagonal operators that leave $|\alpha\rangle$ unchanged and off-diagonal operators that change the occupation numbers of $|\alpha\rangle$. The time evolution of $|\alpha\rangle$ becomes particularly clear in the interaction-expansion representation[3] where the Hamiltonian $\hat{H} = \hat{H}_0 - \hat{H}_1$ is split into the diagonal part $\hat{H}_0$ (including the chemical potential) and the off-diagonal perturbation $\hat{H}_1$. We consider the hopping term $\hat{H}_1 = t\sum_i \hat{B}_{i,i+1} = t\sum_b \hat{B}_b$ as the perturbation and introduce the bond variable b between lattice sites i and $i+1$. It is important that the operators in the perturbation $\hat{H}_1$ are non-branching, i.e., $\hat{B}_b |\alpha\rangle \sim |\alpha'\rangle$. Then,

[3] The interaction picture as well as the interaction expansion are defined in App. A.

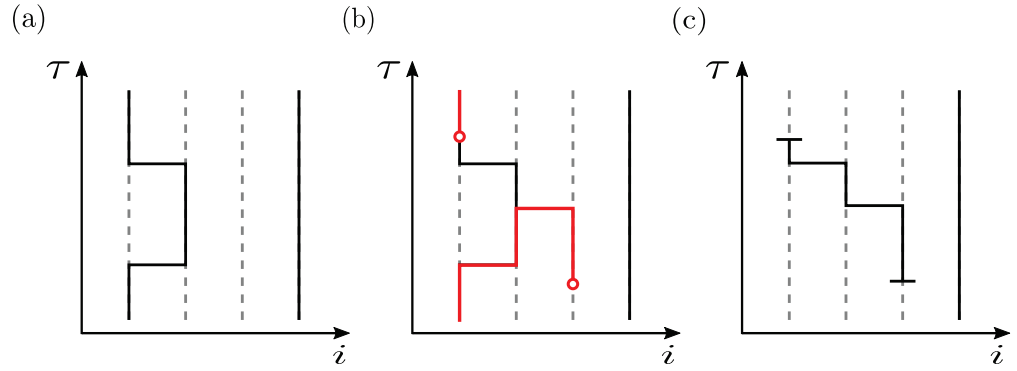

Figure 3.1.: (a) Closed world-line configuration for a 4-site system with two electrons. A world line is represented by a solid line and illustrates the path an electron takes in space and imaginary time. (b) The same world-line configuration as in (a) but with an additional worm (red) included. Open circles correspond to the head and the tail of the worm. (c) Flipping the occupation numbers in (a) along the path of the worm in (b) leads to an open world-line configuration with two world-line discontinuities. Thereby, kinks can be created or annihilated.

the perturbation expansion becomes

$$Z = \sum_{n=0}^{\infty} t^n \sum_{b_1 \ldots b_n} \int_0^{\beta} d\tau_n \ \ldots \int_0^{\tau_3} d\tau_2 \int_0^{\tau_2} d\tau_1 \sum_{\alpha} \langle\alpha| e^{-\beta \hat{H}_0} \hat{B}_{b_n}(\tau_n) |\alpha_{n-1}\rangle \langle\alpha_{n-1}| \ldots$$
$$\ldots |\alpha_2\rangle \langle\alpha_2| \hat{B}_{b_2}(\tau_2) |\alpha_1\rangle \langle\alpha_1| \hat{B}_{b_1}(\tau_1) |\alpha\rangle \ , \quad (3.20)$$

where $\hat{B}_b(\tau) = e^{\tau \hat{H}_0} \hat{B}_b \, e^{-\tau \hat{H}_0}$. We end up with a time-ordered sequence of operators $\hat{B}_{b_p}(\tau_p)$ that act at time τ_p and propagate the initial state $|\alpha\rangle$. Since the propagated state $|\alpha_p\rangle \sim \prod_{l=1}^{p} \hat{B}_{b_l} |\alpha\rangle$ is uniquely defined, we need not sum over intermediate states.

From Eq. (3.20) the world-line representation of the interaction expansion becomes manifest. Starting with an initial state $|\alpha\rangle = |n_1, \ldots, n_L\rangle$, the occupation numbers cannot change until the first operator $\hat{B}_{b_1}(\tau_1)$ is applied at time τ_1. The expectation value $\langle\alpha_1| \hat{B}_{b_1}(\tau_1) |\alpha\rangle$ is only nonzero if one of the sites of bond b_1 is occupied and the other site is empty. Then, $\hat{B}_{b_1}(\tau_1)$ exchanges the occupation numbers at bond b_1. This procedure is repeated for the remaining operators $\hat{B}_{b_p}(\tau_p)$. In the end, we obtain a graphical representation as shown in Fig. 3.1(a), where solid lines correspond to occupied lattice sites and dashed lines to empty sites. Then, the path a single electron takes in space and imaginary time defines a world line. An electron can only hop to a neighboring site if an operator $\hat{B}_{b_p}(\tau_p)$ is applied. The resulting horizontal line is called a kink.

Equation (3.20) is the starting point to formulate world-line QMC methods for instantaneous interactions in continuous time. Usually, these methods are applied to bosonic or spin models, but they can also be used to simulate 1D fermionic models.[4] A Monte Carlo configuration is then defined by the expansion order n, the initial state $|\alpha\rangle$, and a

[4] For fermionic models in more than one dimension, world-line QMC methods suffer from a sign problem.

list of kinks C_n, where each kink has a bond and a time variable. The Monte Carlo weight $W_\alpha(C_n)$ factorizes into a product of weights $\langle\alpha_p|\,\hat{B}_{b_p}(\tau_p)\,|\alpha_{p-1}\rangle = e^{\tau_p \Delta E_p}\,\langle\alpha_p|\,\hat{B}_{b_p}\,|\alpha_{p-1}\rangle$ where we define $\Delta E_p = \langle\alpha_p|\,\hat{H}_0\,|\alpha_p\rangle - \langle\alpha_{p-1}|\,\hat{H}_0\,|\alpha_{p-1}\rangle$ as the energy change of the diagonal term at kink p. If $\hat{H}_0$ consists of local operators, the weight of a kink is completely determined by the change of the occupation numbers at the corresponding bond. Originally, world-line QMC methods used local update procedures in the form of kink motion or the creation and annihilation of kink-antikink pairs. However, these local updates lead to a series of problems: The Monte Carlo sampling can only be performed in the canonical ensemble and cannot change the winding number of a world-line configuration. In the end, the local kink updates lead to long autocorrelation times, especially in the vicinity of second-order phase transitions [53].

A very efficient world-line QMC method for instantaneous interactions is the worm algorithm introduced by Prokof'ev *et al.* [53]. It circumvents the problem of long autocorrelation times by performing the Monte Carlo sampling in an enlarged configuration space. In addition to the closed world-line configurations of the partition function, the worm algorithm also considers configurations with two world-line discontinuities that are connected by a "worm". These configurations correspond to the single-particle Green's function and the end points of the worm are the space-time coordinates of particle creation and annihilation. They are represented by additional matrix elements $\langle\alpha_p|\,\hat{c}_i^\dagger(\tau)\,|\alpha_{p-1}\rangle$ and $\langle\alpha_q|\,\hat{c}_j(\tau_0)\,|\alpha_{q-1}\rangle$ in the expansion (3.20). In the worm algorithm, the head of the worm becomes a dynamical object that can move through space and imaginary time and thereby creates or annihilates kinks [see Figs. 3.1(b) and (c)]. Only when the head of the worm hits its own tail, the world line closes and a valid configuration for the partition function is reached again. In the end, this entire process corresponds to a global update of a world-line configuration. Because each worm update only requires local information from the world-line configuration, this update procedure is very efficient and $\mathcal{O}(L\beta)$ operations lead to an independent Monte Carlo configuration. For further details on the worm algorithm, see Refs. [53, 106, 107].

Recently, Zi Cai *et al.* [72] extended the worm algorithm to the simulation of retarded interactions that are diagonal in the occupation number. To formulate the method, they used the path-integral representation of the perturbation expansion (3.16) and put all the diagonal terms contained in $\mathcal{S}$ into the unperturbed part $\mathcal{S}_0$, i.e.,

$$\mathcal{S}_0 = \int_0^\beta d\tau \sum_i \bar{c}_i(\tau)\,\partial_\tau\, c_i(\tau) + \int_0^\beta d\tau\, H_0(\tau) + \mathcal{S}_{\text{ret}}\,. \tag{3.21}$$

For the Holstein model, $H_0(\tau)$ only contains the chemical potential. As in the interaction expansion (3.20), the perturbation $\mathcal{S}_1$ is given by the electronic hopping terms. Using the vertex notation of Eq. (3.15), we have $\nu = \{b, \tau\}$, $w_\nu = t$, and $h_\nu = B_b(\tau)$. The Monte Carlo weight $W_\alpha(C_n)$ can then be obtained by mapping the time-ordered expectation value $\langle h_{\nu_1} \dots h_{\nu_n}\rangle_0$ to the world-line representation (3.20). It takes exactly the same form, up to an additional factor $\exp(-\mathcal{S}_{\text{ret}}[\{n_i(\tau)\}])$ that stems from the retardation. The worm updates can be formulated as usual, but the Monte Carlo weights cannot be obtained from the local world-line configuration anymore. For each update step,

the double integral in $\mathcal{S}_{\mathrm{ret}}[\{n_i(\tau)\}]$ requires the knowledge of the density $n_i(\tau)$ for all times $\tau \in [0, \beta)$. Therefore, the worm algorithm only scales as $\mathcal{O}(L\beta^2)$ for retarded interactions. If the interaction is also nonlocal in space, the scaling becomes even worse leading to $\mathcal{O}(L^2\beta^2)$ operations to obtain independent Monte Carlo configurations. Zi Cai *et al.* [72] applied the worm algorithm to a 1D bosonic model with a retarded density-density interaction that is local in space and reached system sizes of $L = 128$ and $\beta t = L/2$ [72].

Similar world-line approaches to retarded interactions appear in the context of DMFT using the hybridization expansion method [75] to understand dynamical screening effects [76–78], and in extended DMFT calculations [79,80]. However, all these approaches have in common that only diagonal retarded interactions can be simulated.

3.2.4. Stochastic series expansion representation

A different representation that is closely related to the world-line picture introduced above is the stochastic series expansion (SSE) representation [82]. It corresponds to a high-temperature expansion of the partition function in the Hamiltonian formulation and is given by

$$\begin{aligned} Z &= \sum_{\alpha} \langle\alpha| e^{-\beta\hat{H}} |\alpha\rangle = \sum_{\alpha} \sum_{n=0}^{\infty} \frac{(-\beta)^n}{n!} \langle\alpha| \hat{H}^n |\alpha\rangle \\ &= \sum_{\alpha} \sum_{n=0}^{\infty} \frac{\beta^n}{n!} \sum_{S_n} \langle\alpha| \prod_{p=1}^{n} \hat{H}_{a_p,b_p} |\alpha\rangle \ . \end{aligned} \tag{3.22}$$

The Hamiltonian $\hat{H}$ is written as a sum of local operators, $\hat{H} = -\sum_{a,b} \hat{H}_{a,b}$, where a specifies an operator type and b the bond between sites $i(b)$ and $j(b)$. The expansion (3.22) is sampled stochastically. A configuration with expansion order n corresponds to a string of n operators, specified by the index sequence $S_n = \{[a_1, b_1], \ldots, [a_n, b_n]\}$,[5] and a state $|\alpha\rangle$ from a complete basis in which $\hat{H}$ is non-branching, i.e., $\hat{H}_{a,b}|\alpha\rangle \sim |\alpha'\rangle$. In the spirit of the world-line representation introduced above, the sequence of operators $\hat{H}_{a_p,b_p}$ leads to a propagation of the initial state $|\alpha\rangle$ in imaginary time and the propagated state is given by $|\alpha_p\rangle \sim \prod_{l=1}^{p} \hat{H}_{a_l,b_l} |\alpha\rangle$. However, there is no explicit notion of imaginary time because we expand in the total Hamiltonian. In contrast to the worm algorithm, the SSE representation requires that $\hat{H}$ contains both off-diagonal ($a = 1$) and diagonal ($a = 2$) operators. Then two types of updates are sufficient to achieve ergodicity: the diagonal updates and the directed-loop updates.

Before we describe the update procedures, we first introduce a graphical representation of the operator sequence using the world-line picture. This simplifies our further discussion of the directed-loop updates. For simplicity, we consider a spinless fermionic model, but the basic ideas can be easily generalized to other systems. Figure 3.2(a) shows two examples of a typical vertex appearing in a world-line configuration. Each

[5] We use the symbol S_n instead of C_n because in the SSE representation the index sequence does not include imaginary-time variables.

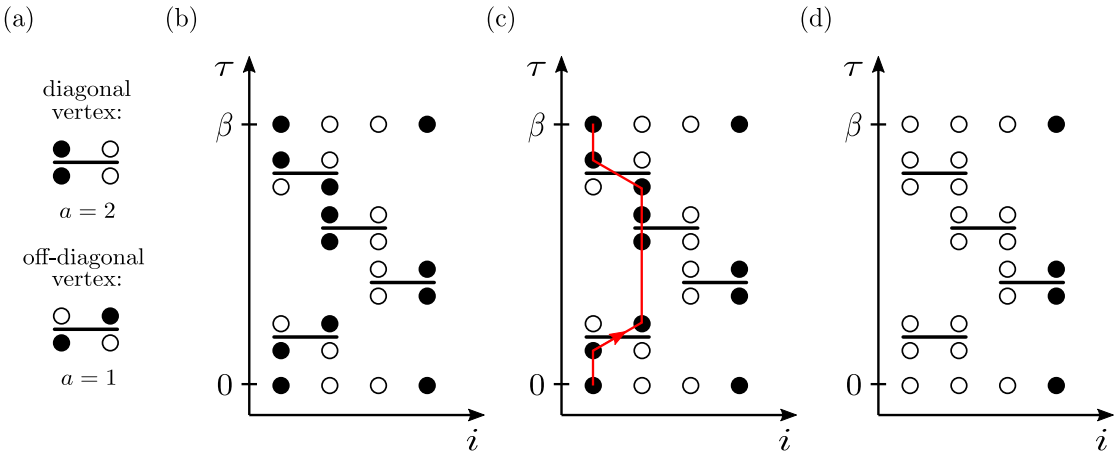

Figure 3.2.: (a) Examples for a diagonal and an off-diagonal vertex. The vertex structure is explained in the main text. (b) A sequence of vertices that illustrates the propagation of the initial state $|\alpha\rangle$ and generates the same world-line configuration as in Fig. 3.1(a). (c) During the directed-loop updates, a closed loop (red) is constructed that starts at the lower vertex and propagates in the direction of the arrow. (d) Flipping the occupation numbers of the vertex legs connected by the loop changes the operator types of the vertices as well as the initial state $|\alpha\rangle$.

vertex consists of a horizontal bar representing the operator and four circles attached to it, also called the legs of the vertex. The two lower (upper) circles illustrate the occupation of the state at neighboring lattice sites before (after) the operator is applied. Here, open (filled) symbols indicate empty (occupied) lattice sites. A diagonal operator then leaves the state unchanged, whereas an off-diagonal operator exchanges the fillings of the circles. A typical SSE world-line configuration is now defined by a sequence of vertices, as shown in Fig. 3.2(b). Therefore, we do not draw filled (dashed) lines for occupied (unoccupied) world lines anymore [as in Fig. 3.1(a)]. Figure 3.2(b) shows the same world-line configuration as Fig. 3.1(a), but contains additional off-diagonal vertices that do not change the world-line configuration.

The efficiency of the SSE representation for QMC simulations relies on the *directed-loop updates* which provide global updates that significantly reduce autocorrelation times. They are very similar to the worm updates discussed before. In the latter, the occupation of a world-line segment is changed along a closed loop that is constructed from local update moves of the world-line discontinuities. In contrast to the worm algorithm, the directed loops connect different vertices of a world-line configuration and can only jump to neighboring sites at the positions of the vertices. Starting at an entrance leg l_e of a randomly chosen vertex, the choice of the exit leg l_x determines how the vertex changes as a result of the flipping of the occupation numbers n_{l_e}, n_{l_x} to $1 - n_{l_e}, 1 - n_{l_x}$. Thereby, the operator type of the vertex can change from $a = 1$ to $a = 2$ or vice versa. From l_x the loop continues to the next vertex until it closes. The probabilities for choosing l_x are determined by the directed-loop equations for a general vertex [55], which can be derived from the requirement of local detailed balance (cf. Sec. 3.4.3). An example for a directed

loop is given in Fig. 3.2(c) and the resulting world-line configuration in Fig. 3.2(d).

During the directed-loop updates, the number of vertices as well as their positions are fixed. Therefore, we need a second type of update procedure, the *diagonal updates*, which changes the total number of operators in the operator string S_n. This is done by adding or removing diagonal operators that do not change the world-line configuration. For an efficient sampling, it is convenient to fix the length of the operator string to N by inserting $N-n$ unit operators ($a=0$).[6] Then, S_N can be traversed sequentially and updates $\hat{H}_{0,b} \leftrightarrow \hat{H}_{2,b}$ be proposed. The corresponding configuration weights are directly obtained from the propagated state $|\alpha_p\rangle$. For further details see Ref. [55].

The SSE representation can also be obtained from the path-integral formulation of the perturbation expansion. For this purpose, we make the trivial choice

$$\mathcal{S}_0 = \int_0^\beta d\tau \sum_i \bar{c}_i(\tau)\, \partial_\tau\, c_i(\tau) \tag{3.23}$$

and put all the other terms into the perturbation $\mathcal{S}_1$. For problems without retardation, Eq. (3.15) takes the form $\mathcal{S}_1 = -\int d\tau \sum_{a,b} H_{a,b}(\tau)$, i.e., $\nu = \{a,b,\tau\}$, $w_\nu = 1$, and $h_\nu = H_{a,b}(\tau)$. The relation between the perturbation expansion in Eq. (3.16) and the SSE representation (3.22) is established by mapping the time-ordered expectation value to an operator string:

$$\sum_{S_n} Z_0 \langle h_{\nu_1} \dots h_{\nu_n} \rangle_0 = \sum_{S_n} \sum_\alpha \langle\alpha| \prod_p \hat{H}_{a_p,b_p} |\alpha\rangle \ . \tag{3.24}$$

While the Grassmann fields on the l.h.s. imply time ordering, it becomes explicit by the operator sequence on the r.h.s. We included the sum over S_n in Eq. (3.24) to relabel the operator types and bonds after the application of time ordering. On the r.h.s., the time labels have become obsolete. Therefore, the additional τ-integrals contained in $\sum_{C_n}$ [cf. Eq. (3.16)] can be carried out and give β^n, leading to Eq. (3.22). A mapping between the SSE and the time-ordered interaction expansion in the full Hamiltonian was previously introduced in Ref. [91].

For retarded interactions such as Eq. (3.12), $\langle h_{\nu_1} \dots h_{\nu_n} \rangle_0$ can still be mapped to an operator string to calculate the weight of a configuration. However, the fact that for $\mathcal{S}_{\text{ret}}$ the weight $w_\nu = P_+(\tau - \tau')$ depends on imaginary time demands an explicit sampling of the τ-integrals, as well as time-ordering of the fields. Since $\mathcal{S}_1$ consists of bilinears $\bar{c}(\tau)c(\tau)$, this re-ordering does not change the sign of the configuration. To formulate the Monte Carlo updates for retarded interactions, we have to solve basically two issues: On the one hand, the diagonal updates cannot be performed as before by traversing the operator string since the two constituents of the retarded interaction act at different positions in the operator string. On the other hand, one has to find a coherent representation of the vertices that allows an exchange of the bilinear hopping terms with one time argument and the biquadratic interaction terms with two time arguments in the directed-loop updates and still preserves the locality of the loop construction.

[6] If N is large enough, we do not introduce a systematic error. A convenient choice is $N = 1.25\,n$ [55].

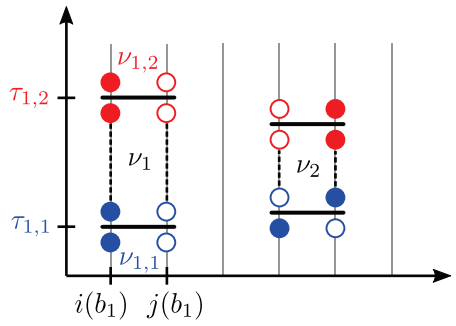

Figure 3.3.: Vertices for the spinless Holstein model [cf. Eqs. (3.26) and (3.27)]. Vertex ν_1 is a diagonal vertex ($a_{1,1} = a_{1,2} = 2$) on bond b_1 connecting sites $i(b_1)$ and $j(b_1)$. It consists of subvertices $\nu_{1,1}$ at time $\tau_{1,1}$ and $\nu_{1,2}$ at $\tau_{1,2}$. Vertex ν_2 is off-diagonal ($a_{2,1} = 1$, $a_{2,2} = 0$) and acts at b_2, $\tau_{2,1}$, $\tau_{2,2}$.

To formulate the directed-loop algorithm for retarded interactions, it is expedient to write each vertex ν_k as two subvertices $\nu_{k,1}$ and $\nu_{k,2}$. While this is already the case for the retarded interaction, we add a unit "operator" $\mathbb{1}_b(\tau)$ with a dummy time variable to the hopping terms. Each subvertex then has local variables $\nu_{k,j} = \{a_{k,j}, b_{k,j}, \tau_{k,j}\}$ (see Fig. 3.3). For the Holstein model, $b_{k,1} = b_{k,2} = b_k$. To lighten the notation we drop the index k from here on. We write Eq. (3.15) as

$$\mathcal{S}_1 = -\iint_0^\beta d\tau_1 d\tau_2 \, P_+(\tau_1 - \tau_2) \sum_{a_1,a_2,b} h_{a_1 a_2, b}(\tau_1, \tau_2) \,. \tag{3.25}$$

The off-diagonal hopping vertices are given by

$$\begin{aligned} h_{10,b}(\tau_1, \tau_2) &= \frac{t}{2} B_b(\tau_1) \, \mathbb{1}_b(\tau_2) \,, \\ h_{01,b}(\tau_1, \tau_2) &= \frac{t}{2} \mathbb{1}_b(\tau_1) \, B_b(\tau_2) \,, \end{aligned} \tag{3.26}$$

whereas the diagonal interaction vertices read

$$h_{22,b}(\tau_1, \tau_2) = \lambda t \left[C + \rho_{i(b)}(\tau_1) \, \rho_{i(b)}(\tau_2) + \rho_{j(b)}(\tau_1) \, \rho_{j(b)}(\tau_2) \right] \tag{3.27}$$

with $j(b) = i(b) + 1$. For simplicity, we set the chemical potential to zero. To arrive at the form (3.25), we multiplied the off-diagonal terms in Eq. (3.26) with the bosonic propagator and exploited $\int_0^\beta d\tau_2 \, P_+(\tau_1 - \tau_2) = 1$ for the dummy time variables. This essentially promotes the hopping terms to retarded interactions and yields a vertex weight $\mathcal{W}_\nu = w(\tau_1, \tau_2) \, W[h_{a_1 a_2, b}(\tau_1, \tau_2)] \, d\tau_1 d\tau_2$.[7] Here, $w_\nu = w(\tau_1, \tau_2) = P_+(\tau_1 - \tau_2)$ irrespective of the operator types a_1, a_2. As a result, $P_+(\tau_1 - \tau_2)$ only plays a role for the diagonal updates but drops out of the directed-loop equations, allowing for a simple

[7] Because $\mathcal{W}_\nu$ is the Monte Carlo weight for a vertex, we included the imaginary-time measures $d\tau_1$ and $d\tau_2$ in its definition.

and efficient implementation (cf. Sec. 3.4.3). By contrast, $W[h_{a_1a_2,b}(\tau_1,\tau_2)]$ depends on time only implicitly via the world-line configuration. Finally, the constant $C = 1/2 + \delta$ ($\delta \geq 0$) in Eq. (3.27) ensures positive weights.

In the diagonal updates, the operator string cannot be traversed sequentially anymore because each vertex update requires knowledge of the propagated state at two distinct positions in the string. However, the occupation number at $\{i, \tau\}$ is completely determined by the initial state $|\alpha\rangle$ and the number of off-diagonal operators that act between 0 and τ and involve site i. During the diagonal updates, we construct an ordered list containing the time arguments of the operators $B_{b(i)}(\tau)$ for each i. Sorting this list takes $\mathcal{O}(L\beta \log \beta)$ operations, after which any propagated state can be quickly calculated. Diagonal updates involve adding or removing a single vertex $h_{22,b}(\tau_1,\tau_2)$ using the Metropolis-Hastings algorithm (cf. Sec. 3.1.2). Sampling τ_1, τ_2 according to the phonon propagator $P_+(\tau_1 - \tau_2)$ by inverse transform sampling ensures high acceptance rates for any phonon frequency ω_0.

The directed-loop updates for retarded interactions are now very similar to those for instantaneous interactions. Our generalization exploits (i) the subvertex structure introduced above, (ii) the fact that the update of a subvertex only changes the world-line configuration locally into another allowed configuration, and (iii) our choice of the weight $w(\tau_1,\tau_2)$ that removes any time dependence from the directed-loop equations. Because of these conditions, each subvertex can be updated individually during the loop construction. However, the retarded interaction (3.12) leads to an update probability that also depends on the other subvertex connected via $P_+(\tau)$.

The ideas presented in this section to generalize the directed-loop algorithm to retarded interactions are not restricted to the Holstein model, but also apply to other models, e.g., Fröhlich, SSH, and spin-phonon models [31]. The SSE representation is therefore more flexible than the interaction-expansion representation used for the worm algorithm regarding the simulation of retarded interactions and reaches system sizes of $L = 1282$ and $\beta t = 2L$ [P2]. In Sec. 3.4, we give a detailed discussion of the directed-loop algorithm including a definition of the vertex weights, the formulation of the diagonal and directed-loop updates, the definition of observables, test results for the Holstein model, and the discussion of possible extensions to other models.

3.3. Bosonic observables from the distribution of vertices

An apparent disadvantage of the fermionic approach is the loss of direct access to bosonic observables. However, as shown in Sec. 2.2, the latter can be systematically calculated from sum rules over fermionic correlation functions. For QMC methods that treat the retarded interaction as a perturbation, information about the bosonic fields is also encoded in the vertex distribution. For models with a local fermion-boson interaction (e.g., the Holstein model), the bosonic contributions to the total energy as well as the local bosonic propagator can be calculated efficiently from the vertex distribution. Moreover, with the help of auxiliary Ising fields [108] originally introduced to avoid the sign problem [70], even nonlocal correlation functions such as the full bosonic propagator become

accessible. Finally, we derive an estimator for the fidelity susceptibility that is applicable to retarded boson-mediated interactions and can be used to identify phase transitions.

In the following, we show which observables can be recovered from the vertex distribution for a generic model (with vertex h_ν). Then, we apply the general results to the Holstein model. Finally, we use the CT-INT method to provide a performance test of these estimators compared to a direct numerical integration of the fermionic sum rules. The presentation in this section is based on Ref. [P3].

The bosonic estimators derived below become particularly useful in the SSE representation where observables must be recovered from the world-line configurations. As shown in Sec. 3.4.4, the bosonic estimators remain valid and only require an easy substitution.

3.3.1. Estimators from the distribution of vertices

Expectation values of operators h_ν contained in the perturbation $\mathcal{S}_1$ can be calculated efficiently from the distribution of vertices [91]. To this end, h_ν is regarded as an additional vertex written as $h_\nu = w_\nu^{-1} \sum_{\nu_{n+1}} w_{\nu_{n+1}} h_{\nu_{n+1}} \delta_{\nu,\nu_{n+1}}$ and absorbed into the perturbation expansion:

$$\begin{aligned}\langle h_\nu \rangle &= \frac{Z_0}{Z} \sum_{n=0}^{\infty} \sum_{C_n} \frac{1}{n!} w_{\nu_1} \dots w_{\nu_n} \langle h_{\nu_1} \dots h_{\nu_n} h_\nu \rangle_0 \\ &= \frac{1}{w_\nu} \sum_{n=0}^{\infty} \sum_{C_{n+1}} \sum_{\alpha} (n+1)\, p_\alpha(C_{n+1})\, \delta_{\nu,\nu_{n+1}} \\ &= \sum_{n=0}^{\infty} \sum_{C_n} \sum_{\alpha} p_\alpha(C_n) \left[\frac{1}{w_\nu} \sum_{k=1}^{n} \delta_{\nu,\nu_k} \right].\end{aligned} \tag{3.28}$$

Here, we first identified the probability distribution $p_\alpha(C_{n+1})$ of a configuration with $n+1$ vertices and then shifted the summation index to obtain $p_\alpha(C_n)$. Finally, we included the $n = 0$ contribution to the sum and replaced the factor of n by a sum over the equivalent vertices. Comparison with Eq. (3.17) yields

$$\langle\!\langle h_\nu \rangle\!\rangle_{C_n} = \frac{1}{w_\nu} \sum_{k=1}^{n} \delta_{\nu,\nu_k} \ . \tag{3.29}$$

From here on, we drop the subscript α because it does not have any influence on the vertex measurements. From Eq. (3.29) we obtain the familiar relation between the perturbation term and the average expansion order, $\langle \mathcal{S}_1 \rangle = -\langle n \rangle$ [67]. Because $\langle \mathcal{S}_1 \rangle$ is an extensive thermodynamic quantity, the average expansion order $\langle n \rangle \sim \beta L$. In the same way, we can obtain higher-order correlation functions, e.g.,

$$\langle\!\langle h_\nu h_{\nu'} \rangle\!\rangle_{C_n} = \frac{1}{w_\nu w_{\nu'}} \sum_{k \neq l} \delta_{\nu,\nu_k} \delta_{\nu',\nu_l} \ . \tag{3.30}$$

Each variable contained in the superindex ν can be resolved from a configuration C_n, but continuous variables (e.g., imaginary time τ) have to be integrated over (at least on

a small interval) to make sense of the corresponding delta functions. The evaluation of observables via Eqs. (3.29) and (3.30) only requires $\mathcal{O}(n)$ operations since

$$\sum_{k\neq l} \delta_{i,k}\,\delta_{j,l} = \sum_{k} \delta_{i,k} \sum_{l} \delta_{j,l} - \sum_{k} \delta_{i,k}\,\delta_{j,k}\,. \tag{3.31}$$

Although the vertex measurements are restricted to operators that appear in the perturbation, the class of accessible observables grows with the complexity of the interaction, as demonstrated below for the fermion-boson problem.

3.3.2. Bosonic estimators for the Holstein model

The bosonic estimators are derived for the Holstein model using the interaction term

$$\mathcal{S}_1 = -\lambda t \iint_0^\beta d\tau d\tau' \sum_{i\sigma\sigma' s} \left[\rho_{i,\sigma}(\tau) - s\delta\right] P_+(\tau-\tau') \left[\rho_{i,\sigma'}(\tau') - s\delta\right] \tag{3.32}$$

as introduced for the CT-INT method in Sec. 3.2.2. In the vertex notation of Eq. (3.15), $\nu = \{i, \tau, \tau', \sigma, \sigma', s\}$, $w_\nu = \lambda t\, P_+(\tau-\tau')$, and

$$h_\nu = \rho_{i,\sigma}(\tau)\rho_{i,\sigma'}(\tau') + \delta^2 - s\delta\left[\rho_{i,\sigma}(\tau) + \rho_{i,\sigma'}(\tau')\right]. \tag{3.33}$$

The operators contained in Eq. (3.33) can be measured from the distribution of vertices. In particular, we have access to the dynamical charge correlations required for the calculation of the bosonic observables in Sec. 2.2.3. The estimators derived below also apply to other models with local fermion-boson coupling like the optical SSH model. For the latter, we just have to replace $\rho_{i,\sigma}(\tau) \to B_{i,\sigma}(\tau)$, $\lambda \to \lambda/4$, and set $\delta = 0$.[8]

Total energy

In the CT-INT method, the kinetic energy of the electrons is calculated from the single-particle Green's function. To recover the bosonic contributions (2.30)–(2.32) to the total energy from the distribution of vertices, we sum over the auxiliary Ising variable s in Eq. (3.33) and use Eq. (3.29) to obtain the estimator

$$\left\langle\!\!\left\langle \rho_{i,\sigma}(\tau)\rho_{i,\sigma'}(\tau') \right\rangle\!\!\right\rangle_{C_n} + \delta^2 = \sum_{k=1}^{n} \frac{\delta_{i,i_k}\delta_{\sigma,\sigma_k}\delta_{\sigma',\sigma'_k}\,\delta(\tau-\tau_k)\,\delta(\tau'-\tau'_k)}{2\lambda t\, P_+(\tau_k-\tau'_k)} \tag{3.34}$$

for the local charge-charge correlation function. Applying the sum rules (2.30)–(2.32) to Eq. (3.34), we get the estimators

$$E_{\mathrm{ph}}^{\mathrm{kin}}(C_n) = \frac{E_{\mathrm{ph}}^0}{2} - \sum_{k=1}^{n} \frac{P_-(\tau_k)P_-(\tau'_k)}{P_+(\tau_k-\tau'_k)}\,, \tag{3.35}$$

[8] If we set $\delta = 0$, the auxiliary Ising variables $s = \pm 1$ become meaningless. As a consequence, the boson propagator cannot be obtained from the distribution of vertices anymore.

$$E_{\mathrm{ph}}^{\mathrm{pot}}(C_n) = \frac{E_{\mathrm{ph}}^0}{2} + \sum_{k=1}^{n} \frac{P_+(\tau_k)P_+(\tau_k')}{P_+(\tau_k - \tau_k')} - 2\lambda t L N_\sigma^2 \delta^2 \,, \tag{3.36}$$

$$E_{\mathrm{ep}}(C_n) = -\frac{2n}{\beta} + 4\lambda t L N_\sigma^2 \delta^2 \,. \tag{3.37}$$

For the kinetic energy the term $\sim \delta^2$ vanishes due to the antisymmetry of $P_-(\tau)$. N_σ counts the number of spin components of the Holstein model, i.e., $N_\sigma = 1$ for the spinless and $N_\sigma = 2$ for the spinful model.

The estimators for $E_{\mathrm{ph}}^{\mathrm{kin}}$ and $E_{\mathrm{ph}}^{\mathrm{pot}}$ can be further improved by exploiting the global translational invariance of all vertices, i.e., $\tau_k \to \tau_k + \Delta$ and $\tau_k' \to \tau_k' + \Delta$ with $\Delta \in [0, \beta)$. We integrate over Δ to treat all the translations exactly, which allows for the transformation

$$\frac{P_\pm(\tau_k)P_\pm(\tau_k')}{P_+(\tau_k - \tau_k')} \longrightarrow \frac{1}{\beta}\int_0^\beta d\Delta \, \frac{P_\pm(\tau_k + \Delta)P_\pm(\tau_k' + \Delta)}{P_+(\tau_k - \tau_k')} = \bar{P}_\pm(\tau_k - \tau_k') \tag{3.38}$$

to the averaged propagator ($\tau \in [-\beta, \beta]$)

$$\bar{P}_\pm(\tau) = \frac{1}{2\beta} \pm \frac{\omega_0}{4}\frac{\beta - |\tau|}{\beta}\left[\coth(\omega_0\beta/2) - \frac{P_-(\tau)}{P_+(\tau)}\right] \pm \frac{\omega_0}{4}\frac{|\tau|}{\beta}\left[\coth(\omega_0\beta/2) + \frac{P_-(\tau)}{P_+(\tau)}\right]. \tag{3.39}$$

Since the substitution (3.38) applies to time differences of the same vertex, the computational cost to calculate the energies remains $\mathcal{O}(n)$. The improvement is particularly noticeable for $E_{\mathrm{ph}}^{\mathrm{kin}}$ (see Sec. 3.3.3).

Fidelity susceptibility

Recently, Wang *et al.* [81] derived a universal QMC estimator for the fidelity susceptibility χ_{F} based on the distribution of vertices. Originally, their estimator was only valid for equal-time interactions. We briefly summarize their results, focusing on the CT-INT method, and then show how this estimator applies to retarded boson-mediated interactions.

The fidelity susceptibility is a geometrical tool originating from quantum information theory [109]. It can be used to detect quantum critical points without prior knowledge of the order parameter from the change of the ground state upon changing the Hamiltonian $\hat{H}(\alpha) = \hat{H}_0 + \alpha\hat{H}_1$ via a driving parameter α. In Refs. [110–112], χ_{F} was extended to finite temperatures in terms of the structure factor

$$\chi_{\mathrm{F}}(\alpha) = \int_0^{\beta/2} d\tau \left[\left\langle \hat{H}_1(\tau)\hat{H}_1(0)\right\rangle - \left\langle \hat{H}_1(0)\right\rangle^2\right]\tau \,. \tag{3.40}$$

Wang *et al.* [81] recognized that $\chi_{\mathrm{F}}(\alpha)$ can be recovered from the distribution of vertices using Eqs. (3.29) and (3.30), leading to the covariance estimator

$$\chi_{\mathrm{F}} = \frac{\langle n_{\mathrm{L}} n_{\mathrm{R}}\rangle - \langle n_{\mathrm{L}}\rangle\langle n_{\mathrm{R}}\rangle}{2\alpha^2} \,. \tag{3.41}$$

For each vertex configuration, n_L and n_R count the number of vertices in the intervals $[0, \beta/2)$ and $[\beta/2, \beta)$, respectively.

The calculation of χ_F via Eq. (3.41) is restricted to fermionic interactions of the form $S_1 = \alpha \int d\tau H_1(\tau)$, i.e., actions that are local in time and related to a Hamiltonian $\hat{H}_1$. Using the example of the Holstein model, we generalize the fidelity susceptibility to retarded boson-mediated interactions. Because χ_F is defined from a Hamiltonian, we start from Eq. (3.40) and identify the electron-phonon coupling as the driving term with $\alpha = g$ and $\hat{H}_1 = \sum_i \hat{Q}_i \hat{\rho}_i$. The displacements $\hat{Q}_i$ entering the expectation values in Eq. (3.40) via $\hat{H}_1$ can be replaced with fermionic operators using the source terms introduced in Sec. 2.2.3. $\langle H_1 \rangle$ is given by Eq. (2.32), and

$$\begin{aligned} \left\langle H_1(\tau) H_1(\tau') \right\rangle = 2 \sum_{\nu_1} w_{\nu_1} \langle h_{\nu_1} \rangle \, \delta(\tau - \tau_1) \, \delta(\tau' - \tau_1') \\ + 4 \sum_{\nu_1 \nu_2} w_{\nu_1} w_{\nu_2} \langle h_{\nu_1} h_{\nu_2} \rangle \, \delta(\tau - \tau_1') \, \delta(\tau' - \tau_2') \end{aligned} \tag{3.42}$$

in the vertex notation of the Holstein model. Continuing the derivation as in Ref. [81], we obtain an estimator very similar to Eq. (3.41),

$$\chi_\mathrm{F} = \frac{\langle \tilde{n}_\mathrm{L} \tilde{n}_\mathrm{R} \rangle - \langle \tilde{n}_\mathrm{L} \rangle \langle \tilde{n}_\mathrm{R} \rangle}{2g^2} \,. \tag{3.43}$$

However, in the present case, each vertex contains two bilinears with times τ_k and τ_k', and $\tilde{n}_\mathrm{L}$ and $\tilde{n}_\mathrm{R}$ count the numbers of these bilinears in the left and right half of the partitioned imaginary-time axis. For simplicity, we omitted a constant shift in Eq. (3.43) that arises from the δ-dependent terms in Eq. (3.33). Taking it into account leads to $\chi_\mathrm{F} \to \chi_\mathrm{F} - 2\lambda t L N_\sigma^2 \delta^2 \tanh(\beta\omega_0/4)/(\omega_0 g^2)$.

Phonon propagator

Equation (3.34) only gives access to local charge-charge correlations. For the Holstein model, we can also obtain nonlocal correlation functions from the distribution of vertices, including the phonon propagator. For this purpose, we exploit the information provided by the Ising variable s. If we consider $\sum_s s\, h_\nu$, the first two terms in Eq. (3.33) drop out and only individual charge operators are left. Analogously, by taking

$$\sum_{s_1 s_2} s_1 s_2 \, h_{\nu_1} h_{\nu_2} = 4\delta^2 \left[\rho_{i_1,\sigma_1}(\tau_1) + \rho_{i_1,\sigma_1'}(\tau_1') \right] \left[\rho_{i_2,\sigma_2}(\tau_2) + \rho_{i_2,\sigma_2'}(\tau_2') \right] , \tag{3.44}$$

we can recover nonlocal charge correlations from Eq. (3.30). The simplest estimator is the charge susceptibility

$$\begin{aligned} \chi_{ij}(C_n) &= \frac{1}{\beta} \iint_0^\beta d\tau d\tau' \left\langle\!\!\left\langle \rho_i(\tau) \rho_j(\tau') \right\rangle\!\!\right\rangle_{C_n} \\ &= \frac{1}{16(\lambda t)^2 N_\sigma^2 \delta^2 \beta^3} \sum_{k \neq l} \frac{s_k \, \delta_{i,i_k}}{P_+(\tau_k - \tau_k')} \frac{s_l \, \delta_{j,i_l}}{P_+(\tau_l - \tau_l')} \,, \end{aligned} \tag{3.45}$$

which is obtained from the summation over all variables except for the lattice sites.[9] The phonon propagators (2.27) and (2.28) take the form

$$K \left\langle\!\!\left\langle q_i(\tau)\, q_j(\tau') \right\rangle\!\!\right\rangle_{C_n} = P_+(\tau-\tau')\,\delta_{i,j} + \frac{1}{4\lambda t N_\sigma^2 \delta^2} \sum_{k\neq l} \frac{P_+(\tau-\tau_k) P_+(\tau-\tau_k')\, s_k\, \delta_{i,i_k}}{P_+(\tau_k-\tau_k')} \times \frac{P_+(\tau'-\tau_l) P_+(\tau'-\tau_l')\, s_l\, \delta_{j,i_l}}{P_+(\tau_l-\tau_l')}\,, \quad (3.46)$$

$$\frac{1}{M} \left\langle\!\!\left\langle p_i(\tau)\, p_j(\tau') \right\rangle\!\!\right\rangle_{C_n} = P_+(\tau-\tau')\,\delta_{i,j} - \frac{1}{\lambda t N_\sigma^2 \delta^2 \beta^2} \sum_{k\neq l} \frac{P_-(\tau-\tau_k)\, s_k\, \delta_{i,i_k}}{P_+(\tau_k-\tau_k')} \times \frac{P_-(\tau'-\tau_l)\, s_l\, \delta_{j,i_l}}{P_+(\tau_l-\tau_l')}\,. \quad (3.47)$$

To arrive at Eq. (3.46), we multiplied Eq. (3.44) with the symmetrized propagator P_+ for each of the four times on the r.h.s. before integrating over the imaginary times. For Eq. (3.47), we included the antisymmetrized propagator P_- only for one pair of times, but the estimator can be further improved by considering the remaining three combinations.

The simplest way to calculate the phonon propagators (3.46) and (3.47) is to fix the second time argument to $\tau' = 0$ and apply Eq. (3.31) to obtain the necessary information from the vertices in $\mathcal{O}(nN_\tau)$ operations. Here, N_τ is the number of τ points on which the correlation functions are calculated. Similar to the equal-time case, especially the estimator for the momentum correlations can be improved by using translational invariance. However, the rigorous approach of integrating over all translations increases the computational cost to $\mathcal{O}(n^2 N_\tau)$ operations since the sums in the first term of Eq. (3.31) can no longer be calculated independently. This problem can be overcome by measuring the correlation functions on an equidistant grid with spacing $\Delta\tau_{\mathrm{obs}}$ so that translations of all vertices by multiples of $\Delta\tau_{\mathrm{obs}}$ are available and the computational cost remains $\mathcal{O}(nN_\tau)$. Regardless, translational invariance can be applied rigorously to the second term in Eq. (3.31). Putting the contributions of the phonon propagator together requires another $\mathcal{O}(L^2 N_\tau^2)$ operations, where an additional factor of N_τ comes from exploiting translational invariance. This last step dominates the computational time for vertex measurements (cf. Sec. 3.3.3).

3.3.3. Performance of the vertex measurements

In the CT-INT method, the computation of the single-particle Green's function for the calculation of observables via Wick's theorem requires $\mathcal{O}(n^2 L N_\tau)$ operations, where N_τ is the number of τ points. If N_τ is scaled with β, the calculation of dynamical correlation functions is of the same order as the Monte Carlo updates. For fermion-boson problems, even the bosonic energies in Eqs. (2.30)–(2.32) require the full time dependence of $\langle \rho_i(\tau)\rho_j(0)\rangle$. On the other hand, the calculation from the vertex distribution involves only $\mathcal{O}(n)$ operations for the energies and $\mathcal{O}(nN_\tau)$ for the phonon propagator. For the latter, exploiting translational invariance leads to another $\mathcal{O}(L^2 N_\tau^2)$ operations to set

[9] Similarly, the (spin-resolved) charge correlation function can be calculated in Matsubara frequencies.

Table 3.1.: Ratios of statistical errors for averages from vertex measurements and Wick's theorem for different simulation parameters. Ratios larger than 1 mean that estimators from Wick's theorem are more precise. The reference point is the spinless Holstein model with $\omega_0/t = 0.4$, $\lambda = 0.5$, $L = \beta t = 22$, and $\delta = 0.51$. The first two rows indicate the observable and estimator used. The last column reports the average expansion order.

observable	E_{ep}	$E_{\mathrm{ph}}^{\mathrm{pot}}$			$E_{\mathrm{ph}}^{\mathrm{kin}}$			$\chi(\pi)$	$\langle n \rangle$
from Eq.	(3.37)	(3.36)	(3.38)	(3.46)	(3.35)	(3.38)	(3.47)	(3.45)	
reference	2.6	4.0	2.6	2.5	20	5.6	5.9	1.2	151
$\lambda = 1.0$	1.2	1.4	1.1	1.2	4.8	1.6	1.3	1.0	371
$\lambda = 1.5$	1.1	1.3	1.1	1.6	18	3.3	2.9	1.0	661
$L = \beta t = 14$	3.2	4.0	3.2	0.2	19	6.4	4.0	1.2	62
$L = \beta t = 30$	2.6	5.0	2.7	2.8	23	5.4	13	1.3	282
$\delta = 1.0$	3.7	7.0	4.0	2.1	32	8.5	4.4	1.2	510

up the final estimator. For large n, the computational cost for the vertex measurements becomes negligible.

The above considerations were verified for the spinless Holstein model with $\omega_0/t = 0.4$, $L = \beta t = 22$, $\lambda = 1.5$, and 1000 Monte Carlo steps between measurements. The average expansion order was $\langle n \rangle \approx 660$ and we used $\Delta\tau_{\mathrm{obs}} = 0.1$ ($N_\tau = 220$). The computation of dynamical correlation functions using Wick's theorem took 26% of the total time, of which 86% went into the matrix-vector multiplications necessary to calculate the Green's function. Only 1% of the total time was used for the vertex measurements, most of which went into the $\mathcal{O}(L^2 N_\tau^2)$ operations necessary to set up the translation-invariant phonon propagator. If we omitted this last operation, the vertex measurements only took 0.02% of the total time, and were dominated by the exact evaluation of $P_\pm(\tau)$ for each vertex. Approximately the same time would be needed for equal-time measurements from Wick's theorem using $N_\tau = 1$. Hence, further improvements through tabulation of $P_\pm(\tau)$ seem unnecessary.

Aside from the significant speed-up, another advantage of the vertex measurements is the exact calculation of imaginary-time integrals. By contrast, Wick's theorem provides $\langle \rho_i(\tau)\rho_j(0) \rangle$ only on a finite grid so that systematic errors from numerical integration can arise. For $\omega_0/t = 0.4$, using Simpson's rule on an equidistant grid with $\Delta\tau_{\mathrm{obs}} = 0.1$ was sufficient to make systematic errors irrelevant. However, more elaborate integration schemes may be necessary for larger ω_0.

Table 3.1 reports ratios of statistical errors of averages obtained from either the vertex distribution or Wick's theorem, as determined in the same simulation and hence for the same number of bins. Ratios larger than 1 mean that estimators obtained from Wick's theorem are more precise. We considered different bosonic energies, as well as the charge susceptibility $\chi(q)$ at $q = \pi$ which tracks CDW order. For $E_{\mathrm{ph}}^{\mathrm{pot}}$ and $E_{\mathrm{ph}}^{\mathrm{kin}}$ we compared three different estimators: the simple estimators (3.35) and (3.36) from one set of vertices, the improved estimators using translational invariance [Eq. (3.38)], and the estimators for the phonon propagators using the Ising spins, Eqs. (3.46) and (3.47).

The reference results are for the spinless Holstein model with $\omega_0/t = 0.4$, $\lambda = 0.5$, $L = \beta t = 22$, and $\delta = 0.51$. For the resulting rather small expansion order $\langle n \rangle \approx 151$, the estimators from Wick's theorem have better statistics, i.e., the ratios in Table 3.1 are larger than one. The vertex estimators improve significantly upon exploiting translational invariance, especially $E_{\mathrm{ph}}^{\mathrm{kin}}$. Increasing the number of vertices per phase-space volume via the interaction parameter λ levels out the differences between estimators, except for $E_{\mathrm{ph}}^{\mathrm{kin}}$ at $\lambda = 1.5$. By contrast, changing $\langle n \rangle$ via the phase-space parameters L and β leaves most of the ratios essentially unchanged. The same is true when increasing the number of vertices via the Ising-spin parameter δ. Finally, Table 3.1 confirms that $\langle n \rangle \sim \beta L$, whereas the dependence on λ is nonlinear.

Although the dependence of the statistical errors on the simulation parameters is not completely systematic, the vertex measurements become advantageous especially at large expansion orders. The errors are of the same order of magnitude, but the vertex estimators are much faster and avoid systematic integration errors.

3.4. Directed-loop algorithm for retarded interactions

In Sec. 3.2.4, we have already discussed the key ideas that underlie our formulation of the directed-loop QMC method for retarded interactions. In the following, we give a detailed description of the method using the example of the spinful Holstein model. In particular, we define the configuration space and the vertex weights, discuss the details of the diagonal and directed-loop updates, carry over the bosonic estimators derived in the previous section to the SSE representation, and present some test results that demonstrate the efficiency of the algorithm. Finally, we discuss possible extensions of our method to other models. The goal of this section is to provide the necessary theoretical background to understand and implement the directed-loop algorithm for retarded interactions. For practical information on the implementation of the method see Ref. [55]. The presentation in this section is based on Ref. [P2] and its supplemental material.

3.4.1. Configuration space and vertex weights

The directed-loop algorithm for retarded interactions is based on the generic formulation of the perturbation expansion in the path-integral representation discussed in Sec. 3.2.1. The Monte Carlo sampling is over configurations $C = \{n, C_n, |\alpha\rangle\}$ defined by the expansion order n, the ordered vertex list $C_n = \{\nu_1, \ldots, \nu_n\}$, and the state $|\alpha\rangle$ in the local occupation number basis. In Sec. 3.2.4, we defined the interaction vertex for the spinless Holstein model. In the following, we extend it to the spinful case, where each subvertex $j \in \{1, 2\}$ now has local variables $\{a_j, b, \sigma_j, \tau_j\}$ labeling its operator type, bond, spin, and imaginary-time value. The interaction (3.15) becomes

$$\mathcal{S}_1 = -\iint_0^\beta d\tau_1 d\tau_2 \, P_+(\tau_1 - \tau_2) \sum_{\substack{a_1,a_2,b,\\ \sigma_1,\sigma_2}} h^{\sigma_1\sigma_2}_{a_1 a_2,b}(\tau_1, \tau_2)\,. \tag{3.48}$$

The off-diagonal hopping vertices are now given by

$$h_{10,b}^{\sigma_1\sigma_2}(\tau_1,\tau_2) = \frac{t}{2N_\sigma} B_{b,\sigma_1}(\tau_1)\,\mathbb{1}_{b,\sigma_2}(\tau_2)\,, \tag{3.49}$$
$$h_{01,b}^{\sigma_1\sigma_2}(\tau_1,\tau_2) = \frac{t}{2N_\sigma} \mathbb{1}_{b,\sigma_1}(\tau_1)\,B_{b,\sigma_2}(\tau_2)\,,$$

whereas the diagonal interaction vertices read

$$h_{22,b}^{\sigma_1\sigma_2}(\tau_1,\tau_2) = \lambda t\left[C + \rho_{i(b),\sigma_1}(\tau_1)\,\rho_{i(b),\sigma_2}(\tau_2) + \rho_{j(b),\sigma_1}(\tau_1)\,\rho_{j(b),\sigma_2}(\tau_2)\right] \tag{3.50}$$

with $j(b) = i(b) + 1$. We introduced an additional factor N_σ in the hopping terms that counts the number of spin flavors and compensates the sum over the second spin index. For the spinful Holstein model, we have $N_\sigma = 2$, whereas the spinless case is recovered by choosing $N_\sigma = 1$ and dropping the spin indices. Note that we only consider the half-filled Holstein model. However, the chemical potential can be easily included in the diagonal term (3.50).

To calculate the Monte Carlo weight $W_\alpha(C_n)$, we map $\langle h_{\nu_1}\dots h_{\nu_n}\rangle_0$ to an operator string (see the discussion in Sec. 3.2.4). Then, the weight is given by[10]

$$W_\alpha(C_n) = \frac{1}{n!}\prod_{p=1}^{n}\mathcal{W}_{\nu_p} \quad \text{with} \quad \mathcal{W}_\nu = P_+(\tau_1-\tau_2)\,W[h_{a_1a_2,b}^{\sigma_1\sigma_2}(\tau_1,\tau_2)]\,d\tau_1 d\tau_2\,. \tag{3.51}$$

As usual for world-line representations, $W_\alpha(C_n)$ factorizes into a product of individual vertex weights $\mathcal{W}_\nu$. The explicit time dependence of the vertex is in $P_+(\tau_1-\tau_2)\,d\tau_1 d\tau_2$ which is independent of the operator type and therefore has to be considered only during the diagonal updates (see below). The remainder $W[h_{a_1a_2,b}^{\sigma_1\sigma_2}(\tau_1,\tau_2)]$ can be calculated from the propagated state $|\alpha_p\rangle$ that is included between each of the $2n$ subvertices of the operator string. Since each vertex is nonlocal in time, we use states $|\alpha_p\rangle$ and $|\alpha_q\rangle$ that belong to different positions p and q in the operator string. We obtain

$$W[h_{10,b}^{\sigma_1\sigma_2}(\tau_1,\tau_2)] = \frac{t}{2N_\sigma}\langle\alpha_{p+1}|\,\hat{B}_{b,\sigma_1}\,|\alpha_p\rangle\,\langle\alpha_{q+1}|\,\hat{\mathbb{1}}_{b,\sigma_2}\,|\alpha_q\rangle = \frac{t}{2N_\sigma}\langle\alpha_{p+1}|\,\hat{B}_{b,\sigma_1}\,|\alpha_p\rangle\,, \tag{3.52}$$
$$W[h_{01,b}^{\sigma_1\sigma_2}(\tau_1,\tau_2)] = \frac{t}{2N_\sigma}\langle\alpha_{p+1}|\,\hat{\mathbb{1}}_{b,\sigma_1}\,|\alpha_p\rangle\,\langle\alpha_{q+1}|\,\hat{B}_{b,\sigma_2}\,|\alpha_q\rangle = \frac{t}{2N_\sigma}\langle\alpha_{q+1}|\,\hat{B}_{b,\sigma_2}\,|\alpha_q\rangle\,, \tag{3.53}$$
$$W[h_{22,b}^{\sigma_1\sigma_2}(\tau_1,\tau_2)] = \lambda t\left[C + \langle\alpha_{p+1}|\,\hat{\rho}_{i(b),\sigma_1}\,|\alpha_p\rangle\,\langle\alpha_{q+1}|\,\hat{\rho}_{i(b),\sigma_2}\,|\alpha_q\rangle + (i\leftrightarrow j)\right]. \tag{3.54}$$

The individual expectation values can be calculated from the occupation-number basis and do not lead to a sign problem in one dimension.[11] The effect of each operator must

[10] Now we include the integration measures of the vertices in the definition of the weight. To keep the notation as simple as possible, we use the same label $W_\alpha(C_n)$ as before.

[11] For fermions, the ordering of the single-particle states in the occupation-number basis is important for the sign of the Monte Carlo weight. In 1D, we order the creation operators along the chain and separated with respect to their spin. For spin-$\frac{1}{2}$ particles, we have

$$|n_{1,\uparrow},\dots,n_{L,\uparrow},n_{1,\downarrow},\dots,n_{L,\downarrow}\rangle = (\hat{c}_{1,\uparrow}^\dagger)^{n_{1,\uparrow}}\dots(\hat{c}_{L,\uparrow}^\dagger)^{n_{L,\uparrow}}(\hat{c}_{1,\downarrow}^\dagger)^{n_{1,\downarrow}}\dots(\hat{c}_{L,\downarrow}^\dagger)^{n_{L,\downarrow}}|0\rangle \tag{3.55}$$

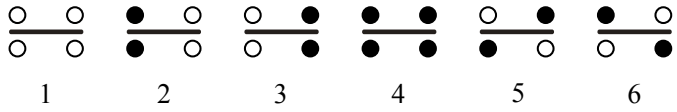

Figure 3.4.: Possible subvertex types for the Holstein model. Open (filled) symbols indicate empty (occupied) lattice sites. Note that only one spin orientation is considered.

be considered only at the two basis states defined by the bond and the spin variable of the operator. In Sec. 3.2.4, we introduced a graphical representation that illustrates the change of the occupation numbers at each subvertex due to the effect of an operator. For the Holstein model, there exist six different graphical representations for each subvertex, as shown in Fig. 3.4. Each of these graphical representations is assigned with a number $v \in \{1,\dots,6\}$ we call the subvertex type. Here, $v \in \{1,\dots,4\}$ corresponds to unit and diagonal operators ($a = 0, 2$) and $v \in \{5,6\}$ to off-diagonal ones ($a = 1$). In the end, the two subvertex types v_1, v_2 completely determine the weight of a vertex and we write $W[h^{\sigma_1\sigma_2}_{a_1a_2,b}(\tau_1,\tau_2)] = W_{v_1,v_2}$. The corresponding weights W_{v_1,v_2} are given in Table 3.2. To give an explicit example, we calculate the weight $W_{1,4}$ for a diagonal

Table 3.2.: Vertex weights W_{v_1,v_2} for the Holstein model for all possible combinations of vertex types v_1 and v_2.

v_1 \ v_2	1	2	3	4	5	6
1	$\lambda t\left(C+\frac{1}{2}\right)$	λtC	λtC	$\lambda t\left(C-\frac{1}{2}\right)$	$t/(2N_\sigma)$	$t/(2N_\sigma)$
2	λtC	$\lambda t\left(C+\frac{1}{2}\right)$	$\lambda t\left(C-\frac{1}{2}\right)$	λtC	$t/(2N_\sigma)$	$t/(2N_\sigma)$
3	λtC	$\lambda t\left(C-\frac{1}{2}\right)$	$\lambda t\left(C+\frac{1}{2}\right)$	λtC	$t/(2N_\sigma)$	$t/(2N_\sigma)$
4	$\lambda t\left(C-\frac{1}{2}\right)$	λtC	λtC	$\lambda t\left(C+\frac{1}{2}\right)$	$t/(2N_\sigma)$	$t/(2N_\sigma)$
5	$t/(2N_\sigma)$	$t/(2N_\sigma)$	$t/(2N_\sigma)$	$t/(2N_\sigma)$	0	0
6	$t/(2N_\sigma)$	$t/(2N_\sigma)$	$t/(2N_\sigma)$	$t/(2N_\sigma)$	0	0

which leads to the phase conventions [113]

$$\hat{c}^\dagger_{i,\uparrow}|\dots,n_{i,\uparrow}=0,\dots\rangle = (-1)^{n^<_{i,\uparrow}}|\dots,n_{i,\uparrow}=1,\dots\rangle\,, \tag{3.56}$$

$$\hat{c}_{i,\uparrow}|\dots,n_{i,\uparrow}=1,\dots\rangle = (-1)^{n^<_{i,\uparrow}}|\dots,n_{i,\uparrow}=0,\dots\rangle\,, \tag{3.57}$$

$$\hat{c}^\dagger_{i,\downarrow}|\dots,n_{i,\downarrow}=0,\dots\rangle = (-1)^{n_\uparrow+n^<_{i,\downarrow}}|\dots,n_{i,\downarrow}=1,\dots\rangle\,, \tag{3.58}$$

$$\hat{c}_{i,\downarrow}|\dots,n_{i,\downarrow}=1,\dots\rangle = (-1)^{n_\uparrow+n^<_{i,\downarrow}}|\dots,n_{i,\downarrow}=0,\dots\rangle\,. \tag{3.59}$$

Here, n_σ counts the total number of spin-σ electrons and $n^<_{i,\sigma}$ the number of spin-σ electrons on sites with position numbers less than i. For open boundary conditions, the hopping operators $\hat{B}_{b,\sigma}$ then do not lead to a negative weight. If we consider periodic boundary conditions $\hat{c}_{L+1,\sigma} = \hat{c}_{1,\sigma}$, the expectation value $\langle\alpha|\,\hat{B}_{b(1,L),\sigma}\,|\alpha'\rangle$ gives an additional phase of $(-1)^{n_\sigma-1}$. At half-filling, we therefore choose lattice sizes $L = 4k+2$ with $k \in \mathbb{N}$. The same is true for spinless fermions.

vertex. Here, the world-line configuration at the first subvertex is determined by $v_1 = 1$ and at the second subvertex by $v_2 = 4$. We first consider the occupation numbers at the left lattice site of each subvertex. For the first subvertex, this site is empty and we obtain $\langle\alpha_{p+1}|\,\hat{\rho}_{i(b),\sigma_1}\,|\alpha_p\rangle = -1/2$ (here $\hat{\rho}_{i,\sigma} = \hat{n}_{i,\sigma} - 1/2$), whereas for the second subvertex it is occupied and we have $\langle\alpha_{q+1}|\,\hat{\rho}_{i(b),\sigma_2}\,|\alpha_q\rangle = 1/2$. The same is true for the expectation values at the right lattice site of each subvertex. Putting everything into Eq. (3.54), we obtain $W_{1,4} = \lambda t\,(C - 1/2)$.

3.4.2. Diagonal updates

The diagonal updates involve adding or removing a single vertex $h^{\sigma_1\sigma_2}_{22,b}(\tau_1,\tau_2)$ using the Metropolis-Hastings algorithm defined in Sec. 3.1.2. We propose the addition of a new vertex with probability density

$$T_0(C_n \to C_{n+1}) = \frac{P_+(\tau_1 - \tau_2)\,d\tau_1 d\tau_2}{L\beta N_\sigma^2\,(n+1)}\,, \tag{3.60}$$

where the bond variable b, the two spin variables σ_1 and σ_2, and one time variable are chosen uniformly. The second time variable is obtained via inverse transform sampling of $P_+(\tau_1 - \tau_2)$.[12] Note that there are $n+1$ possibilities to insert the new vertex into the ordered list C_{n+1}. For the removal of a randomly chosen diagonal vertex, we get

$$T_0(C_{n+1} \to C_n) = \frac{1}{n_2 + 1}\,, \tag{3.62}$$

where n_2 is the number of diagonal vertices in C_n. With the ratio of the Monte Carlo weights in Eq. (3.51), $W_\alpha(C_{n+1})/W_\alpha(C_n) = P_+(\tau_1 - \tau_2)\,W[h^{\sigma_1\sigma_2}_{22,b}(\tau_1,\tau_2)]\,d\tau_1 d\tau_2/(n+1)$, we obtain the Metropolis acceptance rate (3.8) with the Metropolis ratios

$$R(C_n \to C_{n+1}) = \frac{L\beta N_\sigma^2\,W[h^{\sigma_1\sigma_2}_{22,b}(\tau_1,\tau_2)]}{(n_2+1)}\,, \tag{3.63}$$

$$R(C_n \to C_{n-1}) = \frac{n_2}{L\beta N_\sigma^2\,W[h^{\sigma_1\sigma_2}_{22,b}(\tau_1,\tau_2)]} \tag{3.64}$$

for the addition and removal of a vertex, respectively. Note that $P_+(\tau_1 - \tau_2)$ drops out of the acceptance rates because we have already included it in the proposal probabilities. This ensures high acceptance rates for any phonon frequency ω_0.

[12] The phonon propagator $P_+(\tau)$ can be interpreted as a probability distribution function as it is positive and normalized to one. It can be sampled exactly via inverse transform sampling because its cumulative distribution function $G(\tau) = \int_0^\tau d\tau' P_+(\tau')$ can be inverted analytically. If we choose a uniformly-distributed random number $\xi \in [0,1)$, then $G^{-1}(\xi)$ returns a random number drawn from the distribution $P_+(\tau)$. We obtain

$$\tau = \frac{\beta}{2} + \frac{1}{\omega_0}\,\mathrm{asinh}[(2\xi - 1)\sinh(\omega_0\beta/2)]\,. \tag{3.61}$$

To calculate the Metropolis ratios, we need access to the weights $W[h^{\sigma_1\sigma_2}_{22,b}(\tau_1,\tau_2)]$ at arbitrary space-time positions in the world-line configuration. A world-line configuration is determined by the initial state $|\alpha\rangle$ and the positions of the off-diagonal operators $B_{b,\sigma}(\tau)$ and therefore does not change during the diagonal updates. The occupation number at an arbitrary space-time point can therefore be calculated from $|\alpha\rangle$ and the number of off-diagonal operators that act between 0 and τ and involve site i. At the beginning of the diagonal updates, we once construct an ordered list containing the time arguments of the operators $B_{b(i)}(\tau)$ for each i. Sorting this list takes $\mathcal{O}(L\beta\log\beta)$ operations, after which any state can be quickly calculated.

3.4.3. Directed-loop updates

In Sec. 3.2.4, we have already discussed the idea behind the directed-loop updates and how they apply to retarded interactions. In the following, we give a formal derivation of the directed-loop equations from detailed balance that closely follows the presentation in Ref. [55]. We point out the differences that appear for retarded interactions and finally solve the directed-loop equations for the Holstein model. Note that for the spinful model loops are always constructed for a fixed spin orientation.

Derivation of the directed-loop equations

The idea behind the directed-loop updates is to construct a closed loop from local update rules and then flip the world-line configuration along the loop. Thereby, the Monte Carlo configuration changes globally from C to C'. The global change of configurations must fulfill the detailed-balance condition (3.7), which consists of the Monte Carlo weight (3.51) and a transition probability $T(C\to C')$. The transition probability defines the algorithm and will be constructed in such a way that the global detailed-balance condition factorizes into local conditions given by the directed-loop equations.

The transition probability from a closed world-line configuration C to another closed configuration C' can be written as follows:

$$T(C\to C') = \sum_{\text{loops}} T(e_0)\,T(C,e_0\to C_1,e_1)\times\cdots\times T(C_{k-1},e_{k-1}\to C',e_0)\,. \tag{3.65}$$

A graphical example for the construction of the directed loop is shown in Fig. 3.5. At first, a random subvertex leg e_0 is chosen with probability $T(e_0)$ that serves as the starting point for the loop construction [cf. Fig. 3.5(a)]. In the next step, we randomly choose an exit leg of the same subvertex and then proceed along the world line to the entrance e_1 of the next subvertex, as illustrated in Fig. 3.5(b). During this process, the occupation number of the world-line segment is flipped and the world-line configuration changes from the closed configuration C to the configuration C_1 that now contains two world-line discontinuities [cf. Fig. 3.5(c)]. The corresponding transition probability $T(C,e_0\to C_1,e_1)$ is completely defined by the entrance legs of the two subvertices connected by the loop segment and the configurations C and C_1. This update procedure is repeated until the loop returns to its starting point e_0 and closes [see Figs. 3.2(c) and

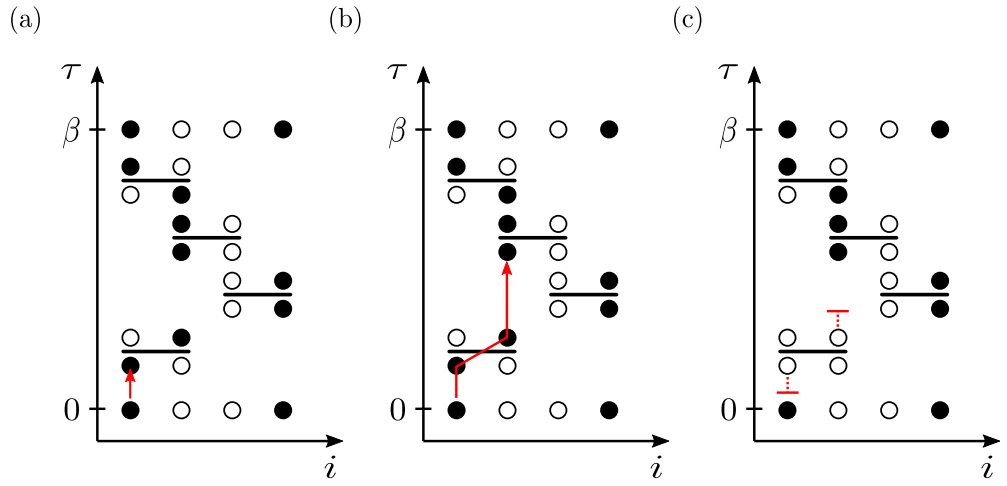

Figure 3.5.: Graphical representation of the initial steps to construct a directed loop using the world-line configuration shown in Fig. 3.2(b). (a) At first, we choose a random subvertex leg e_0 as the starting point for the loop construction (red arrow). (b) Secondly, we randomly choose an exit leg of the same subvertex and then proceed to the entrance e_1 of the next subvertex. (c) Flipping the occupation number along this loop segment generates a configuration with two world-line discontinuities near the entrance and exit leg of the first subvertex (red symbols). We only obtain a closed world-line configuration again when we proceed with the loop construction until it closes, as shown in Figs. 3.2(c) and 3.2(d).

(d) for an example]. Then, we arrive at the closed world-line configuration C'. Since there are many different ways to construct a closed loop that changes C to C', Eq. (3.65) contains a sum over all of these loops.

For the detailed-balance condition, we also need the reverse process

$$T(C' \to C) = \sum_{\text{loops}} T(e_0)\, T(C', e_0 \to C_{k-1}, e_{k-1}) \times \cdots \times T(C_1, e_1 \to C, e_0) \tag{3.66}$$

where the loop is constructed from the starting point e_0 in the opposite direction to generate configuration C from C'. Equations (3.65) and (3.66) are now inserted into the detailed balance condtion (3.7) and we multiply both sides of the equation with the weights $\prod_{i=1}^{k-1} W(C_i)$. Then, detailed balance is satisfied if

$$W(C_i)\, T(C_i, e_i \to C_{i+1}, e_{i+1}) = W(C_{i+1})\, T(C_{i+1}, e_{i+1} \to C_i, e_i) \tag{3.67}$$

holds for each update step. $W(C)$ is given by the Monte Carlo weight (3.51) and factorizes into a product of weights for each vertex. Because in each update step only one vertex is changed (more precisely only one subvertex), the weights of all the other vertices drop out of Eq. (3.67). Moreover, also the phonon propagator P_+ of the remaining vertex drops out of Eq. (3.67) as it does not depend on the operator types of the subvertices. Hence, we are left with the vertex weight W_{v_1,v_2}. It only depends on the two subvertex types v_1 and v_2 that determine the configuration of the vertex. In the following, we

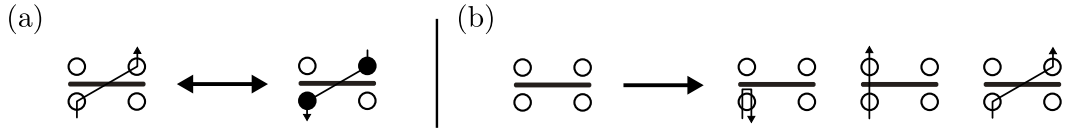

Figure 3.6.: Examples for the (a) first and (b) second directed-loop equation. The first directed-loop equation relates weights $W_{v_2}(v_1, l_1, l_2)$ with exchanged entrance and exit legs l_1 and l_2. The second directed-loop equation states that the weight W_{v_1,v_2} for a vertex without paths assigned is equal to the sum over weights for vertices with fixed entrance leg and all possible exit legs. We only show the paths assigned to subvertex v_1 because v_2 is fixed during the update step.

assume that v_1 is changed during the update step and we write $W_{v_1,v_2} T_{v_2}(v_1, e \to v_1', x) = W_{v_2}(v_1, e, x)$, whereas subvertex v_2 is fixed but still required to calculate the weight. Furthermore, e and x denote the entrance and exit leg of the same subvertex. Equation (3.67) becomes

$$W_{v_2}(v_1, l_1, l_2) = W_{v_2}(v_1', l_2, l_1)\,, \tag{3.68}$$

which is the first directed-loop equation. It states that the weights of two subvertices assigned with inverted directed paths are the same if also the occupation numbers on the sites touched by the loop are flipped [see Fig. 3.6(a) for an expample]. For the transition probability, we also require $\sum_x T_{v_2}(v_1, e \to v_{1,x}', x) = 1$ which means that the path always continues through a subvertex. The sum is over all exit legs x and $v_{1,x}$ means that also the final vertex type depends on the chosen exit leg. This requirement directly translates into the second directed-loop equation

$$\sum_x W_{v_2}(v_1, e, x) = W_{v_1,v_2}\,. \tag{3.69}$$

An example is given in Fig. 3.6(b). From Eqs. (3.68) and (3.69) we can construct the probability tables for the directed-loop updates. Note that the transition probability to choose an exit leg x given the entrance e and the initial subvertices v_1 and v_2 is given by $T_{v_2}(v_1, e \to v_1', x) = W_{v_2}(v_1, e, x)/W_{v_1,v_2}$.

All in all, the directed-loop equations for retarded interactions are almost the same as for instantaneous interactions. For the loop construction, each subvertex is regarded as an independent entity, but the transition probabilities $T_{v_2}(v_1, e \to v_1', x)$ require additional information about the vertex type v_2 of the second subvertex. Formally, this means that always the total vertex is updated [as shown in Fig. 3.7(a)], but the directed path is only assigned to one subvertex and the other subvertex remains unchanged.

Solution of the directed-loop equations for the Holstein model

For the directed-loop updates, the configuration space of subvertex types $v_i \in \{1, \ldots, 6\}$ shown in Fig. 3.4 is enlarged by assigning to subvertex v_1 directed paths that connect an entrance leg e with an exit leg x. This is reflected in the weights $W_{v_2}(v_1, e, x)$ that

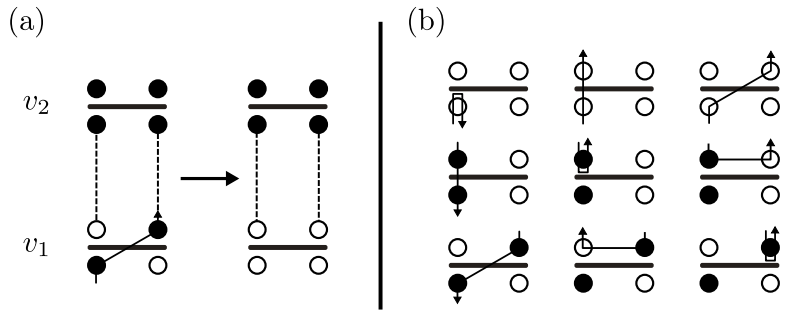

Figure 3.7.: (a) A vertex is determined by the subvertex types v_1 and v_2. The directed path is only assigned to one subvertex and flips the occupation numbers of the corresponding states. Here, we consider $h^{\sigma_1\sigma_2}_{10,b}(\tau_1,\tau_2) \to h^{\sigma_1\sigma_2}_{22,b}(\tau_1,\tau_2)$. (b) Example of an assignment table for the directed-loop equations for a subvertex of type v_1.

are determined by the directed-loop equations (3.68) and (3.69). In the following, we present a particular solution of the directed-loop equations for the Holstein model that avoids backtracking of the loop in a large parameter range.[13]

For the vertices defined by Eqs. (3.49) and (3.50), we have to distinguish two cases: the directed loop either hits a unit operator, or any other operator. For the former case, the path goes straight through the subvertex with probability 1 and changes its vertex type. For the latter case, the directed-loop equations have to be solved explicitly.

We illustrate the solution of the directed-loop equations for the assignment table given in Fig. 3.7(b). We only show the possible assignments for vertex type v_1, corresponding to the lower subvertex in Fig. 3.7(a). The second subvertex of type v_2 remains unaffected by this segment of the loop update but still enters the configuration weight.[14] Each row in Fig. 3.7(b) shows the possible assignments for a fixed entrance leg and the three possible exit legs. The associated weights are related by the second directed-loop equation (3.69). Furthermore, the assignment table is arranged in such a way that the weights are symmetric around the diagonal exploiting the first directed-loop equation (3.68). For the specific example of Fig. 3.7(b), we obtain for the corresponding weights

$$\begin{aligned} b_1 + a + b &= W_{1,v_2}\,, \\ a + b_2 + c &= W_{2,v_2}\,, \\ b + c + b_3 &= W_{5,v_2}\,. \end{aligned} \tag{3.70}$$

The bounce weights b_i, $i \in \{1,2,3\}$, are related to the assignments on the diagonal,

[13] Our derivation follows the presentation in Ref. [114] for the Hubbard model.

[14] As discussed in the main text, the world-line configuration is updated at each subvertex independently. However, while the vertex type of the other subvertex does not change, the same is not in general true for its dummy operator type a_2. For example, a_2 changes from 0 to 2 when interchanging $h^{\sigma_1\sigma_2}_{10,b}(\tau_1,\tau_2) \leftrightarrow h^{\sigma_1\sigma_2}_{22,b}(\tau_1,\tau_2)$ in Fig. 3.7(a). This corresponds to the update from a hopping operator at τ_1 and a unit operator at τ_2 to a (diagonal) density-density interaction term at times τ_1 and τ_2. Because unit operators that change into diagonal operators are relevant for the weights W_{v_1,v_2} in later updates, it is important to keep track of such changes.

whereas a, b, and c are the remaining weights. Our goal is to reduce the bounce weights and solve for a, b, and c. To this end, we write [114]

$$\begin{aligned} a &= \frac{1}{2}\left[W_{1,v_2} + W_{2,v_2} - W_{5,v_2} - b_1 - b_2 + b_3\right] , \\ b &= \frac{1}{2}\left[W_{1,v_2} - W_{2,v_2} + W_{5,v_2} - b_1 + b_2 - b_3\right] , \\ c &= \frac{1}{2}\left[-W_{1,v_2} + W_{2,v_2} + W_{5,v_2} + b_1 - b_2 - b_3\right] . \end{aligned} \tag{3.71}$$

For concreteness, we choose $v_2 = 3$ and insert the weights given in Table 3.2. This leads to

$$\begin{aligned} a &= \frac{1}{2}\left[2\lambda t C - \frac{\left(N_\sigma^{-1} + \lambda\right) t}{2} - b_1 - b_2 + b_3\right] , \\ b &= \frac{1}{2}\left[\frac{\left(N_\sigma^{-1} + \lambda\right) t}{2} - b_1 + b_2 - b_3\right] , \\ c &= \frac{1}{2}\left[\frac{\left(N_\sigma^{-1} - \lambda\right) t}{2} + b_1 - b_2 - b_3\right] . \end{aligned} \tag{3.72}$$

The bounce weights b_i and the constant $C = 1/2 + \delta$ must be chosen such that a, b, and c are positive. For $\lambda < N_\sigma^{-1}$, this is already fulfilled by $b_1 = b_2 = b_3 = 0$ and $\delta \geq (N_\sigma^{-1} - \lambda)/(4\lambda)$. In our simulations, we have chosen the lower bound. For $\lambda \geq N_\sigma^{-1}$, the positivity of c requires $b_1 \geq \left(\lambda - N_\sigma^{-1}\right) t/2$, whereas the positivity of b demands $b_1 \leq \left(\lambda + N_\sigma^{-1}\right) t/2$. We have chosen the lower bound and $\delta = 0$. This procedure has to be repeated for each type of background vertex v_2 and each possible assignment table for v_1. In the end, we find that the global constant C has to be chosen as for the example given here.

Let us point out that analytic solutions of the directed loop equations are neither common nor necessary for efficient simulations. Instead, the equations can be solved using linear programming techniques [115].

3.4.4. Observables

Electronic observables are calculated directly from the Monte Carlo configurations, e.g., from the distribution of vertices or the state $|\alpha\rangle$. Even bosonic correlation functions can be recovered from the distribution of vertices as discussed in Sec. 3.3. In the following, we briefly define the estimators used below.

Estimators for the total energy and the fidelity susceptibility were derived in Sec. 3.3.2. They carry over to the SSE representation by substituting $\delta^2 \to C/2$. For the total energy

$$E(C_n) = E_{\mathrm{el}}(C_n) + E_{\mathrm{ph}}(C_n) + E_{\mathrm{ep}}(C_n) , \tag{3.73}$$

the individual contributions are given by

$$E_{\mathrm{el}}(C_n) = -\frac{n_1}{\beta}\,, \tag{3.74}$$

$$E_{\mathrm{ph}}(C_n) = E^0_{\mathrm{ph}} + \sum_{k=1}^{n_2} \left[\bar{P}_+(\tau_k - \tau'_k) - \bar{P}_-(\tau_k - \tau'_k)\right] - \lambda t C L N_\sigma^2\,, \tag{3.75}$$

$$E_{\mathrm{ep}}(C_n) = -\frac{2n_2}{\beta} + 2\lambda t C L N_\sigma^2\,. \tag{3.76}$$

Here, n_1 and n_2 count the number of off-diagonal and diagonal vertices, respectively. For $E_{\mathrm{ph}}(C_n)$, we already exploited translational invariance of all vertices. The fidelity susceptibility (including the shift) becomes

$$\chi_{\mathrm{F}} = \frac{\langle \tilde{n}_{2,\mathrm{L}} \tilde{n}_{2,\mathrm{R}} \rangle - \langle \tilde{n}_{2,\mathrm{L}} \rangle \langle \tilde{n}_{2,\mathrm{R}} \rangle}{2g^2} - \frac{\lambda t C L N_\sigma^2 \tanh(\beta\omega_0/4)}{\omega_0 g^2}\,. \tag{3.77}$$

Note that it is important to include the shifts proportional to C in the estimators because the optimal C for the directed-loop updates changes with λ. Even the specific heat can be calculated directly from the distribution of vertices. Since the estimator for $\langle\!\langle \hat{H}^2 \rangle\!\rangle_{C_n}$ is much more complicated than for $\langle\!\langle \hat{H} \rangle\!\rangle_{C_n}$, it is given in App. C.1. The phonon propagator cannot be recovered from our choice of the vertex because we only used the constant shift C to avoid the sign problem. However, using an additional Ising variable in the Monte Carlo sampling [cf. Eq. (3.32)] should give access to the phonon propagator.

The real-space correlation function in the charge sector can be calculated via

$$S_\rho(r;\alpha) = \frac{1}{L}\sum_{j=1}^{L} \langle \alpha | \hat{\rho}_{j+r} \hat{\rho}_j | \alpha \rangle \tag{3.78}$$

from the initial state $|\alpha\rangle$. Here, $\hat{\rho}_j = \sum_\sigma (\hat{n}_{j,\sigma} - 1/2)$ is the local charge operator. The spin correlation function $S_\sigma(r;\alpha)$ can be obtained by substituting $\hat{\rho}_j \to \hat{S}^z_j = \sum_\sigma \sigma\, \hat{n}_{j,\sigma}$.

3.4.5. Application to the Peierls transition in the Holstein model

To demonstrate the potential of our new method, we first discuss its efficiency. In standard SSE simulations of the Holstein-Hubbard model, the integrated autocorrelation time τ_{int} essentially diverges with λ [28]. Although reduced by parallel tempering, τ_{int} exceeds 100 at intermediate coupling already for moderately difficult parameters ($\omega_0 = t$, $L = 16$, $\beta t = 2L$) [28]. Figure 3.8 shows τ_{int} for our method for $L = 18$ and $\beta t = 2L$,[15] covering the entire range of phonon frequencies from adiabatic to antiadiabatic and the entire range of couplings from weak to strong. Remarkably, τ_{int} is of order 1 both for the spinful and the spinless Holstein model. Autocorrelations in fact decrease with increasing λ, with no visible signature of the Peierls phase transition. The data shown are for the

[15] A sweep consisted of two blocks of diagonal and directed-loop updates. For each block of diagonal updates, we attempted approximately $2\langle n_2 \rangle$ updates. The number of loop updates was fixed by touching approximately $2\langle n \rangle$ subvertices of type $a = 1, 2$.

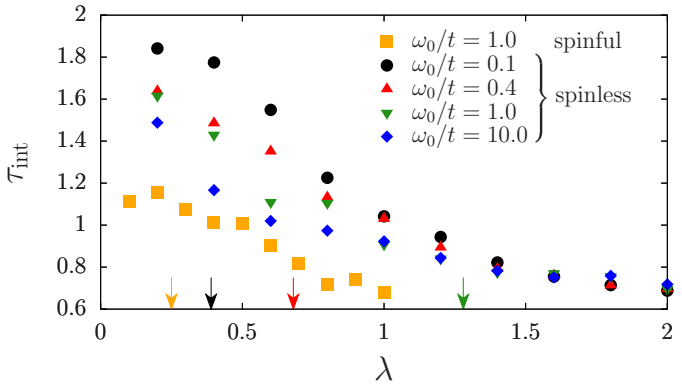

Figure 3.8.: Autocorrelation time τ_{int} for the total energy, as determined from a rebinning analysis [97], for the spinless and the spinful Holstein model. Here, $L = 18$, $\beta t = 2L$. Arrows indicate Peierls critical values $\lambda_c(\omega_0)$ [29, 30].

total energy, for other observables τ_{int} is even smaller. Similar autocorrelation times were observed for larger systems.

Having established its numerical efficiency, we used the directed-loop algorithm to obtain high-precision results for the half-filled spinless Holstein model. The latter provides a generic framework to study the Peierls transition of 1D electrons coupled to quantum phonons. From previous work [20, 26, 27, 29, 116], the model is known to exhibit a Berezinskii–Kosterlitz–Thouless quantum phase transition with dynamical exponent $z = 1$ between a Luttinger liquid and a CDW insulator with a $q = 2k_{\mathrm{F}} = \pi$ modulation of charge density and lattice deformations. Since $z = 1$ we keep $\beta/L = \mathrm{const}$.

Figure 3.9 shows the real-space density correlator $S_\rho(r)$ (using the conformal distance $\xi = L \sin(\frac{\pi r}{L})$ [117]) and the fidelity susceptibility χ_{F} [81, P3], a finite-temperature extension of the quantum fidelity and an unbiased diagnostic for quantum phase transitions [109, 118]. We simulated systems of up to $L = 1282$ sites with $\beta t \geq 2L$. Real-space correlation functions were previously reported for $L \lesssim 50$ [32], DMRG results for other quantities were available up to $L = 256$ [29].

Figure 3.9(a) reveals the theoretically predicted power-law decay of density correlations in a spinless, repulsive Tomonaga-Luttinger liquid [119]. The dominant contribution to $S_\rho(r)$ is the oscillating term $\cos(2k_{\mathrm{F}} r)\, r^{-2K}$ (we only plot even r). The nonuniversal exponent is determined by the Luttinger parameter K. As expected for the Mott transition of a spinless Luttinger liquid, K decreases with increasing λ until it reaches the critical value $K = 1/2$ for $\lambda_c = 0.68(1)$ [29]. This can be seen by comparing to the dashed line in Fig. 3.9(a) that shows a $1/r$ power law. The inset shows estimates for K from power-law fits (see caption for details). For $\lambda > \lambda_c$, K scales to zero and the system exhibits long-range CDW order.

In Fig. 3.9(b), we plot the density correlator at the largest distance $r = L/2$, whose thermodynamic limit serves as an order parameter for the quantum phase transition. We find a nonzero extrapolated order parameter for $\lambda \gtrsim 0.68$, in accordance with Fig. 3.9(a) and previous estimates [29]. The transition can also be detected from the fidelity sus-

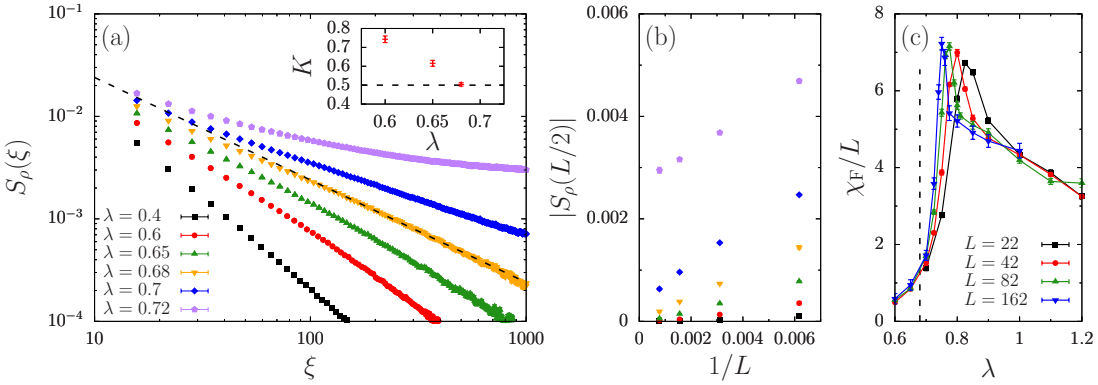

Figure 3.9.: Results for the spinless Holstein model ($\omega_0/t = 0.4$). (a) Real-space density correlator for even distances as a function of the conformal distance $\xi = L\sin(\frac{\pi r}{L})$ [117] on chains of up to $L = 1282$ sites ($\beta t = 2L$). The dashed line indicates the $1/\xi$ decay expected at λ_c. Inset: Luttinger parameter K extracted from fits of $S_\rho(L/2)$ to a/r^{2K} using $L = 162$–562. (b) Finite-size scaling of the density correlations at distance $L/2$, indicating long-range order beyond $\lambda_c = 0.68(1)$. Here, $\beta t = 2L$ and the key is the same as in (a). (c) Fidelity susceptibility for $\beta t = 4L$. The dashed line indicates λ_c.

ceptibility shown in Fig. 3.9(c). Because statistical errors are generally larger for χ_F, the maximum system size was $L = 162$. In contrast to previous work [P3], the directed-loop algorithm permits to reach sufficiently large values of L and β to observe the cusp at λ_c predicted theoretically [120]. The latter sharpens and converges (slowly, similar to other 1D models [120]) to λ_c with increasing L. More generally, Figs. 3.9(b) and (c) are important because they establish the usefulness of the order parameter and χ_F to detect the CDW transition without reference to bosonization results. They can therefore be used for spinful electron-phonon models, the analysis of which is complicated by the existence of a spin gap in the metallic phase [6, 32, 121] and the absence of a reliable theory for the Mott transition of a Luther-Emery liquid [6]. Moreover, our method can access the system sizes necessary to resolve the spin gap [32].

3.4.6. Possible extensions to other models

So far, we have formulated the directed-loop QMC method only for the Holstein model. However, the ideas presented in Sec. 3.2.4 are more general and apply to a variety of models of particles that couple to bosonic modes. A generic action that can be simulated with our directed-loop QMC method must have the form

$$\mathcal{S}_1 = -\iint_0^\beta d\tau_1 d\tau_2 \sum_{a_1,a_2,b_1,b_2} P_{b_1 b_2}(\tau_1 - \tau_2)\, h_{a_1 a_2, b_1 b_2}(\tau_1, \tau_2)\,. \tag{3.79}$$

Here, a_j, b_j, τ_j denote the operator type, bond variable, and time variable of subvertex $j \in \{1, 2\}$. The propagator $P_{b_1 b_2}(\tau_1 - \tau_2)$ can be nonlocal in space and time and must be positive. The operator part $h_{a_1 a_2, b_1 b_2}(\tau_1, \tau_2)$ must be chosen in such a way that we can

switch locally between diagonal ($a = 0, 2$) and off-diagonal ($a = 1$) operators while the configuration at the second subvertex stays the same.

We will give some examples in the following. For fermionic models, we will concentrate on the spinless case, but spin can be trivially included (as shown in Sec. 3.4.1). While fermionic models can only be simulated in 1D due to the sign problem, the corresponding bosonic models as well as spin-boson models can also be simulated in higher dimensions. Of course, all instantaneous interactions that can already be simulated in the SSE representation can also be included in our formulation using a unit operator as the second subvertex and will not be mentioned explicitly.

Fröhlich model

The Fröhlich model is very similar to the Holstein model, but has a long-range electron-phonon interaction of the form $\hat{H}_{\mathrm{ep}} = \gamma \sum_{i,r} f(r) \, (\hat{b}^\dagger_{i+r} + \hat{b}_{i+r}) \, \hat{\rho}_i$. After integrating out the phonons, we obtain the fermionic action

$$\mathcal{S} = -2\lambda t \iint_0^\beta d\tau d\tau' \sum_{ij} \rho_i(\tau) \, P_{ij}(\tau - \tau') \, \rho_j(\tau') \,, \tag{3.80}$$

which is nonlocal in space and time. The phonon propagator has the form $P_{ij}(\tau - \tau') = F(i-j) \, P_+(\tau - \tau')$, where $P_+(\tau - \tau')$ is the same propagator as for the Holstein model and $F(i-j) = \sum_r f(r+i-j) f(r)$ [105]. To rewrite the action into the form of Eq. (3.79), we have to choose $f(r)$ such that $\sum_r F(r) = \bar{F}$ and $F(r) \geq 0$. Then, the vertices for our Monte Carlo method become

$$\begin{aligned} h_{10,b_1 b_2}(\tau_1, \tau_2) &= \frac{t}{2\bar{F}} \, B_{b_1}(\tau_1) \, \mathbb{1}_{b_2}(\tau_2) \,, \\ h_{01,b_1 b_2}(\tau_1, \tau_2) &= \frac{t}{2\bar{F}} \, \mathbb{1}_{b_1}(\tau_1) \, B_{b_2}(\tau_2) \,, \end{aligned} \tag{3.81}$$

as well as

$$h_{22,b_1 b_2}(\tau_1, \tau_2) = \lambda t \left[C + \rho_{i_1(b_1)}(\tau_1) \, \rho_{i_2(b_2)}(\tau_2) + \rho_{j_1(b_1)}(\tau_1) \, \rho_{j_2(b_2)}(\tau_2) \right] \tag{3.82}$$

with $j_1(b) = i_1(b) + 1$ and $j_2(b) = i_2(b) + 1$. These vertices are very similar to those in the Holstein model with the difference that the subvertices are located at different bonds and the phonon propagator has a spatial dependence. All the other details of the algorithm stay the same.

Su-Schrieffer-Heeger model

Our directed-loop method is not restricted to density-density-type interactions, but can also be used to simulate bond-bond couplings

$$\mathcal{S} = -\frac{\lambda t}{2} \iint_0^\beta d\tau d\tau' \sum_b B_b(\tau) \, P_+(\tau - \tau') \, B_b(\tau') \tag{3.83}$$

that appear in the SSH model. Here, we use optical phonons with a local interaction between bond operators [see Eq. (2.7) for the definition of the model], where the propagator is defined as for the Holstein model.[16] For the SSH model, the off-diagonal hopping vertices are the same as for the Holstein model

$$h_{10,b}(\tau_1,\tau_2) = \frac{t}{2} B_b(\tau_1)\,\mathbb{1}_b(\tau_2)\,, \qquad (3.84)$$
$$h_{01,b}(\tau_1,\tau_2) = \frac{t}{2} \mathbb{1}_b(\tau_1)\,B_b(\tau_2)\,,$$

but also the interaction is now given by an off-diagonal term, i.e.,

$$h_{11,b}(\tau_1,\tau_2) = \frac{\lambda t}{2} B_b(\tau_1)\,B_b(\tau_2)\,. \qquad (3.85)$$

In the directed-loop updates, we can perform local updates to switch between $h_{11,b}$ and $h_{10,b}$. However, we also have to include a diagonal operator to change the number of vertices during the diagonal updates. The simplest choice is just a constant shift in energy given by

$$h_{00,b}(\tau_1,\tau_2) \propto \mathbb{1}_b(\tau_1)\,\mathbb{1}_b(\tau_2)\,, \qquad (3.86)$$

but could also be a Hubbard interaction for the spinful model. Again, the diagonal updates include the retardation of the phonon propagator. With this additional term, we can include the local updates $h_{00,b} \leftrightarrow h_{10,b}$ to reach every configuration in the directed-loop updates. Of course, the configurational weights are different for this model and the directed-loop equations have to be solved again.

Spin-Peierls model

We can also consider a spin-Peierls models of the form

$$\hat{H} = J \sum_i \left[1 + \alpha\left(\hat{b}_i^\dagger + \hat{b}_i\right)\right] \hat{\vec{S}}_i \hat{\vec{S}}_{i+1} + \omega_0 \sum_i \hat{b}_i^\dagger \hat{b}_i\,. \qquad (3.87)$$

Also for spin-boson models, the bosons can be integrated out leading to the retarded interaction[17]

$$\mathcal{S} = -\lambda J \iint_0^\beta d\tau d\tau' \sum_b \left[\vec{S}_{i(b)}(\tau)\,\vec{S}_{i(b)+1}(\tau)\right] P_+(\tau-\tau') \left[\vec{S}_{i(b)}(\tau')\,\vec{S}_{i(b)+1}(\tau')\right], \qquad (3.88)$$

[16] In contrast to the optical SSH model (2.7), the original SSH model (2.5) with acoustic phonons leads to a sign problem because the phonon propagator $P_{ij}(\tau)$ that appears in the retarded interaction (2.17) contains negative contributions for $i \neq j$.

[17] The spins can be integrated out using for example a fermionic representation of the spin operators to formulate the path integral. However, a retarded interaction for the spins can also be obtained from the interaction picture without referring to the path integral, as discussed in App. A.

where $\lambda = \alpha^2 J/\omega_0$. For the spin-$\frac{1}{2}$ representation, we split the spin operator into the diagonal and off-diagonal parts as follows

$$\frac{1}{4} - \hat{\vec{S}}_{i(b)}\hat{\vec{S}}_{i(b)+1} = \underbrace{\frac{1}{4} - \hat{S}^z_{i(b)}\hat{S}^z_{i(b)+1}}_{\hat{D}_b} + \underbrace{\frac{1}{2}\left(\hat{S}^+_{i(b)}\hat{S}^-_{i(b)+1} + \hat{S}^-_{i(b)}\hat{S}^+_{i(b)+1}\right)}_{\hat{O}_b}. \tag{3.89}$$

We included a shift of 1/4 to get a positive diagonal weight and used a sublattice rotation to obtain a positive weight for the off-diagonal term (which is possible on a bipartite lattice). In the vertex notation introduced above, we end up with the following terms

$$\begin{aligned}
h_{20,b}(\tau_1,\tau_2) &= \frac{J}{2}\, D_b(\tau_1)\, \mathbb{1}_b(\tau_2)\,, & h_{22,b}(\tau_1,\tau_2) &= \lambda J\, D_b(\tau_1)\, D_b(\tau_2)\,,\\
h_{02,b}(\tau_1,\tau_2) &= \frac{J}{2}\, \mathbb{1}_b(\tau_1)\, D_b(\tau_2)\,, & h_{21,b}(\tau_1,\tau_2) &= \lambda J\, D_b(\tau_1)\, O_b(\tau_2)\,,\\
h_{10,b}(\tau_1,\tau_2) &= \frac{J}{2}\, O_b(\tau_1)\, \mathbb{1}_b(\tau_2)\,, & h_{12,b}(\tau_1,\tau_2) &= \lambda J\, O_b(\tau_1)\, D_b(\tau_2)\,,\\
h_{01,b}(\tau_1,\tau_2) &= \frac{J}{2}\, \mathbb{1}_b(\tau_1)\, O_b(\tau_2)\,, & h_{11,b}(\tau_1,\tau_2) &= \lambda J\, O_b(\tau_1)\, O_b(\tau_2)\,.
\end{aligned} \tag{3.90}$$

Again, the diagonal terms can be easily added and removed during the diagonal updates, whereas every off-diagonal term can be obtained from the diagonal ones by changing one subvertex configuration in the directed-loop updates. With these ideas, the formulation of the update rules is straightforward.

4. Thermodynamic and spectral properties of Peierls chains

In 1D systems, the Peierls instability can lead to a periodic lattice distortion and thereby drive a metal-insulator transition to a state with long-range CDW order. Experimental realizations include the organic charge-transfer salts such as TTF-TCNQ [122, 123] or the blue bronze $K_{0.3}MoO_3$ [124], but similar phenomena can also be found in spin-Peierls materials such as $CuGeO_3$ [125]. Real Peierls compounds can only be regarded as quasi-1D systems because they always couple to an environment. For example, many 1D conductors crystallize in stacks of molecules or atomic clusters where neighboring chains couple weakly [126]. A consequence of the small but finite interchain coupling is that all quasi-1D materials show a crossover and finally a transition to a 3D ordered Peierls state. This ordered state exists below the experimentally observed Peierls transition temperature T_{3D} [126]. Only for temperatures $T \gg T_{3D}$ do these quasi-1D materials resemble the physics of truly 1D systems, including the 1D Peierls physics.

The formation of the Peierls state as a function of temperature is qualitatively understood from the adiabatic approximation, where the phonon dynamics is neglected. Accordingly, the lattice displacements are considered as classical variables and the ground-state of the 1D system is well described by mean-field theory. The temperature scale where the Peierls ordering sets in is then often estimated from the mean-field transition temperature T_{1D}^{MF}. However, thermal fluctuations forbid a finite-temperature phase transition in 1D and only permit a crossover to dominant CDW correlations. The effect of thermal fluctuations on the ordered state was previously studied using a functional Ginzburg-Landau approach [127, 128]. For the specific heat C_V of a Peierls chain it was shown that the discontinuity at T_{1D}^{MF} predicted by mean-field theory is smeared out by thermal fluctuations and the corresponding peak position is shifted to lower temperatures [127]. The peak in C_V also signals a significant increase of the correlation length and the formation of a pseudogap in the density of states [128]. Long-range order and a finite Peierls gap can only appear at $T = 0$ for a truly 1D system. For weakly-coupled chains, a finite-temperature phase transition towards 3D Peierls order takes place. At T_{3D}, experiments show a peak-like anomaly in C_V [129–133] that can be explained by a Ginzburg-Landau approach for weakly coupled chains [134].

The adiabatic approximation is justified for low phonon frequencies and deep in the Peierls phase. In this regime, quantum lattice fluctuations mainly reduce the dimerization [135, 136]. However, in some materials like $CuGeO_3$, where the relevant phonon frequencies are comparable to the spin exchange constant [137], a classical treatment of the phonons is not a priori justified. Historically, the quantum mechanical description of lattice fluctuations was particularly important to explain the low-temperature features

of C_V, which was a key experimental confirmation of early quantum theory [138]. Exact results including quantum lattice fluctuations are rare and often require numerical simulations for microscopic models. Numerical studies of 1D electron-phonon models, for example, showed that quantum lattice fluctuations can destroy the Peierls phase and lead to a metallic ground state (see Ref. [31] for a detailed discussion). A comprehensive study of both thermal and quantum lattice fluctuations was out of reach so far and is the goal of this chapter.

For electron-phonon models, the numerical calculation of thermodynamic properties is challenging and only few results exist for the spin-Peierls problem for selected parameters [83, 84, 139]. DMRG calculations at finite temperatures—successfully carried out for fermionic systems [140]—are so far inhibited by the large Hilbert space of the phonons. The determination of C_V from QMC simulations is affected by long autocorrelation times [44], large fluctuations, and Trotter discretization errors [141]. Moreover, the thermodynamic Bethe ansatz only applies to the classical-phonon limit of the spin-Peierls problem [142]. Our development of the directed-loop algorithm for retarded interactions solves the problem from a QMC point of view: autocorrelation times become negligible (cf. Fig. 3.8 in Sec. 3.4.5), C_V can be calculated directly from the Monte Carlo configurations (see App. C.1), and due to the efficiency of the method statistical fluctuations are under control for sufficiently large system sizes.

In this chapter, we calculate the specific heat of the spinless Holstein model covering the full parameter range of the phase diagram: from the adiabatic to the antiadiabatic regime and from weak to strong coupling. One particular goal is to identify the characteristic low-temperature signatures in C_V for the different regimes in the phase diagram. Figure 4.1 shows the phase diagram of the spinless Holstein model as obtained from DMRG simulations [29] and includes the paths in parameter space along which we carry out our studies.

In Sec. 4.1, we discuss the thermodynamic and spectral properties of Peierls chains in the adiabatic limit (blue arrow in Fig. 4.1). For this purpose, we consider the spinless Holstein model and the spinless SSH model. Their ground states are ordered for any $\lambda > 0$ and described exactly by mean-field theory. In Sec. 4.1.1, we briefly discuss their ground-state properties with respect to the Peierls instability as well as relations to symmetry-protected topological insulators. For the special case of $\omega_0 = 0$, we implemented a Monte Carlo method that makes use of the classical nature of adiabatic phonons (as outlined in Sec. 4.1.2). We apply this method to calculate C_V as a function of the electron-phonon coupling λ (see Sec. 4.1.3). Although we cannot reach larger systems sizes than with the directed-loop algorithm, the classical Monte Carlo method has the advantage that it has direct access to spectral functions on the real-frequency axis. In Secs. 4.1.4 and 4.1.5, we analyze the temperature dependence of the single- and two-particle spectra to explain the key features of the C_V data. Finally, we discuss some relations to disorder problems in Sec. 4.1.6.

The combined effects of thermal and quantum lattice fluctuations on Peierls chains are studied in Sec. 4.2, where we restrict our discussion on the spinless Holstein model.[1]

[1]The SSH model with acoustic phonons cannot be simulated efficiently with the action-based QMC

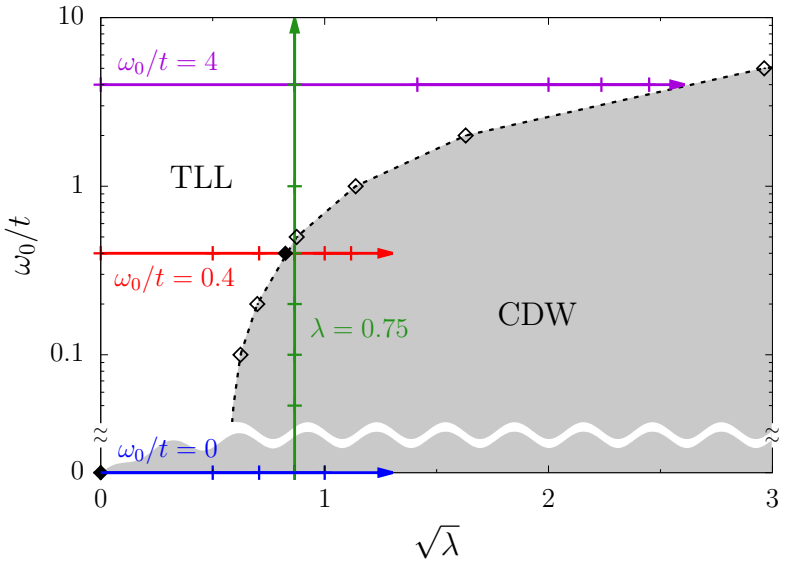

Figure 4.1.: Ground-state phase diagram of the half-filled spinless Holstein model as a function of the electron-phonon coupling λ and the phonon frequency ω_0. Critical values are from DMRG calculations (open symbols) [29]. Additionally, we show our SSE estimate $\lambda_c = 0.68(1)$ at $\omega_0/t = 0.4$ and the exact value $\lambda_c = 0$ at $\omega_0 = 0$ (filled symbols). At $\omega_0 = 0$, the spinless Holstein model shows CDW order for any $\lambda > 0$, whereas for $\omega_0 > 0$ and small λ, quantum lattice fluctuations destroy the ordered state and lead to a Tomonaga-Luttinger-liquid (TLL) phase. For $\omega_0 \to \infty$, the spinless Holstein model maps to free fermions and is always in the metallic phase. Arrows indicate the paths in parameter space along which we discuss the thermodynamic properties of the Holstein model in this chapter. The simulation parameters are indicated by additional markers attached to the arrows.

In Sec. 4.2.1, we study the effect of quantum lattice fluctuations on the specific heat by tuning the phonon frequency ω_0 for a fixed coupling $\lambda = 0.75$ (green arrow in Fig. 4.1). In particular, we test the validity of the adiabatic approximation as ω_0 is increased. The Peierls phase is destroyed at $\omega_{0,c}/t \approx 0.5$ where the system enters the metallic Tomonaga-Luttinger liquid phase. The transition between the metallic and the ordered phase is also studied for a fixed phonon frequency $\omega_0/t = 0.4$ (red arrow in Fig. 4.1). In Sec. 4.2.2, we first consider the single-particle spectral functions of electrons and phonons in the adiabatic regime. In particular, we first discuss the characteristic spectral features in the metallic and in the ordered phase to explain the evolution of C_V as a function of λ in Sec. 4.2.3. In order to unambiguously resolve the $C_V \sim T$ behavior for $T \to 0$ in the Tomonaga-Luttinger liquid phase, we study C_V in Sec. 4.2.4 for $\omega_0/t = 4$ (purple arrow in Fig. 4.1). In the metallic phase of the antiadiabatic regime, C_V also shows the crossover to small polarons as a function of λ.

methods discussed in this thesis because the phonon dispersion leads to negative contributions to the phonon propagator and therefore to a severe sign problem. By contrast, the optical SSH model does not have a sign problem. However, we expect the thermodynamic properties of the optical SSH model to be very similar to the Holstein model because both models have similar phase diagrams [P6].

4.1. Adiabatic Peierls chains

We present exact numerical results for the effects of thermal fluctuations on the thermodynamic and spectral properties of Peierls chains. To this end, a combination of classical Monte Carlo sampling and exact diagonalization is used to study adiabatic half-filled Holstein and SSH models. The classical nature of the lattice displacements in combination with parallel tempering permit simulations on large system sizes and a direct calculation of spectral functions in the frequency domain. Most notably, the long-range order and the associated Peierls gap give rise to a distinct low-temperature peak in the specific heat. The closing of the gap and suppression of order by thermal fluctuations involves in-gap excitations in the form of soliton-antisoliton pairs, and is also reflected in the dynamic charge and bond structure factors as well as in the optical conductivity. We compare our data to the widely used mean-field approximation, and highlight relations to symmetry-protected topological phases and disorder problems. The presentation of this section is based on Ref. [P4].

4.1.1. Electron-phonon models and the Peierls instability

In this section, we define the adiabatic limits for the spinless Holstein and SSH models. Furthermore, we briefly discuss the Peierls instability as well as relations to symmetry-protected topological insulators.

Electron-phonon models in the adiabatic limit

We briefly define the adiabatic limits of the spinless Holstein and SSH models introduced in Sec. 2.1. To simplify the notation for the classical Monte Carlo method discussed below, we split the Hamiltonian

$$\hat{H} = \hat{H}_{\mathrm{ph}} + \hat{H}_{\mathrm{el+ep}} \tag{4.1}$$

into the lattice contribution $\hat{H}_{\mathrm{ph}}$ and the remainder $\hat{H}_{\mathrm{el+ep}}$ that contains the electronic and electron-phonon parts. In general, $\hat{H}_{\mathrm{ph}}$ depends on the lattice displacements $\hat{Q}_i$ and momenta $\hat{P}_i$. In the adiabatic limit, the lattice is static ($M \to \infty$) and the displacements become classical variables q_i, allowing us to replace $\hat{H}_{\mathrm{ph}} \to H_{\mathrm{ph}}$ in Eq. (4.1).

For the spinless Holstein model (2.3), we have the quadratic potential

$$H_{\mathrm{ph}} = \frac{K}{2} \sum_i q_i^2 \tag{4.2}$$

with spring constant K and the electronic part

$$\hat{H}_{\mathrm{el+ep}} = -t \sum_i \left(\hat{c}_i^\dagger \hat{c}_{i+1} + \hat{c}_{i+1}^\dagger \hat{c}_i \right) + g \sum_i q_i \left(\hat{n}_i - 1/2 \right) . \tag{4.3}$$

For the Holstein model, the adiabatic limit follows from Eq. (2.3) by choosing $M \to \infty$ and $\omega_0 \to 0$ at fixed $K = M\omega_0^2$.

In the spinless SSH model (2.5), the lattice energy depends on the relative displacements of neighboring sites,

$$H_{\mathrm{ph}} = \frac{K}{2} \sum_i \left(q_{i+1} - q_i\right)^2 . \tag{4.4}$$

The electronic part,

$$\hat{H}_{\mathrm{el+ep}} = \sum_i \left[-t + \alpha \left(q_{i+1} - q_i\right)\right] \left(\hat{c}_i^\dagger \hat{c}_{i+1} + \hat{c}_{i+1}^\dagger \hat{c}_i\right) , \tag{4.5}$$

describes the modulation of the hopping amplitude by the coupling of the lattice displacements to the bond density. The adiabatic limit follows from Eq. (2.5) by choosing $M \to \infty$ and $\omega_\pi \to 0$ at fixed $K = M\omega_\pi^2/4$. In this limit, the acoustic phonons of the SSH model lose their dispersion. Because the length of the chain is fixed for the SSH model, it has one lattice degree of freedom less than its optical analog (2.7).

For both models, we introduce a dimensionless coupling parameter λ by rescaling the displacement fields. It is defined as in Sec. 2.1: for the Holstein model $\lambda = g^2/(4Kt)$, whereas for the SSH model $\lambda = \alpha^2/(Kt)$. We use t as the unit of energy, set the lattice constant and $\hbar$ to one, and consider half-filling (one electron per two sites).

The Peierls instability and topological excitations

The Fermi surface of the 1D tight-binding model only consists of two points at $k = \pm k_{\mathrm{F}}$, where $k_{\mathrm{F}} = \pi/2$ is the Fermi vector at half-filling. The simplest excitation of a 1D system is the creation of an electron-hole pair with momentum transfer q. Due to perfect nesting between the Fermi points, the charge susceptibility has a $\log \beta$ divergence at the wavevector $q = 2k_{\mathrm{F}}$. This logarithmic divergence drives the Peierls instability at $q = 2k_{\mathrm{F}}$ and the electronic system becomes unstable when coupled to the lattice [126]. This is the case for the spinless Holstein model as well as the spinless SSH model studied in this chapter. At $\omega_0 = 0$ and zero temperature, the exact properties of both models can be obtained from mean-field theory [20,143,144]. For any $\lambda > 0$, the Peierls instability leads to a dimerization of the lattice that is captured by the ansatz $q_i = (-1)^i \Delta/(2g)$ for the Holstein model and $q_i = (-1)^i \Delta/(8\alpha)$ for the SSH model. Here, Δ is the gap calculated self-consistently from the gap equation. The lattice dimerization is accompanied by charge-density-wave order in the Holstein model and bond-density-wave order in the SSH model that has $2k_{\mathrm{F}}$ periodicity. Commensurability with the lattice pins the phase of the order parameter to π [145], so that the ground state is twofold degenerate under $\Delta \to -\Delta$. While exact at $T = 0$, mean-field theory predicts a finite Peierls transition temperature $T_{\mathrm{1D}}^{\mathrm{MF}}$, in violation of the Mermin-Wagner theorem [146]. The adiabatic limit is expected to capture the physics of the dimerized phase [147].

While the Holstein and the SSH model both describe Peierls insulators, important differences arise from their different symmetries. The mean-field SSH Hamiltonian is often considered as the simplest model of a symmetry-protected topological band insulator [148], as reviewed in Ref. [149]. It obeys time-reversal, particle-hole, and chiral

symmetry. Explicitly, under time reversal, $\mathcal{T}\hat{c}_j\mathcal{T}^{-1} = \hat{c}_j$ with $\mathcal{T}\mathrm{i}\mathcal{T}^{-1} = -\mathrm{i}$, whereas for a particle-hole transformation $\mathcal{P}\hat{c}_j\mathcal{P}^{-1} = (-1)^j\hat{c}_j^\dagger$ with $\mathcal{P}\mathrm{i}\mathcal{P}^{-1} = \mathrm{i}$. The chiral symmetry operator is given by $\mathcal{C} = \mathcal{T}\mathcal{P}$. These symmetries put the SSH model into the so-called BDI class of the general classification of symmetry-protected topological phases [150–152] which in 1D allows for a nontrivial topological invariant. The two degenerate ground states of the SSH model belong to different topological sectors. The symmetry-protected zero-energy states of the topological phase are identical to the soliton excitations at domain walls introduced in Refs. [8, 153]. For periodic boundaries, domain walls can only occur as soliton-antisoliton pairs. Depending on their size, such pairs may form bound polaron states with nonzero energy [9]. The Hamiltonian of the Holstein model belongs to the AI symmetry class with broken chiral (and particle-hole) symmetry as a result of the density-displacement coupling. The two degenerate ground states are therefore trivial and do not support topologically protected zero-energy states at domain walls. While the topological classification is strictly valid only at $T = 0$, the electronic symmetries persist for any configuration of displacements generated by thermal fluctuations.

4.1.2. Classical Monte Carlo method

To solve the adiabatic electron-phonon problem at finite temperatures, we used the Monte Carlo method of Ref. [154]. We did not include it in Chap. 3, because it is not based on a perturbation expansion. In the adiabatic limit, and using the notation of Ref. [155], the partition function of Hamiltonian (4.1) takes the form

$$Z = \int_{-\infty}^{\infty} dq_1 \ldots \int_{-\infty}^{\infty} dq_L \, e^{-\beta H_{\mathrm{ph}}} \, Z_{\mathrm{el+ep}}[q_1, \ldots, q_L] \,, \tag{4.6}$$

where $Z_{\mathrm{el+ep}} = \mathrm{Tr}\exp[-\beta(\hat{H}_{\mathrm{el+ep}} - \mu\hat{N})]$ is the grand-canonical partition function of the electronic subsystem, $\beta = 1/k_{\mathrm{B}}T$ the inverse temperature, μ the chemical potential and $\hat{N}$ the total particle-number operator.

For each configuration $C = \{q_1, \ldots, q_L\}$ of the classical displacements, $\hat{H}_{\mathrm{el+ep}}$ is a noninteracting Hamiltonian that can be diagonalized exactly. The Monte Carlo method of Ref. [154] samples the continuous space of displacement configurations C. Expectation values take the form

$$\langle\hat{O}\rangle = \sum_C W(C) \, \langle\!\langle \hat{O} \rangle\!\rangle_C \tag{4.7}$$

with the weight of the configuration

$$W(C) = \frac{1}{Z} \, e^{-\beta H_{\mathrm{ph}}(C)} \, Z_{\mathrm{el+ep}}(C) \tag{4.8}$$

and the corresponding value of the observable

$$\langle\!\langle \hat{O} \rangle\!\rangle_C = \frac{1}{Z_{\mathrm{el+ep}}(C)} \, \mathrm{Tr}\left\{ e^{-\beta[\hat{H}_{\mathrm{el+ep}}(C) - \mu\hat{N}]} \, \hat{O}(C) \right\} . \tag{4.9}$$

The weight $W(C)$ is always positive and can be sampled using the Metropolis-Hastings algorithm, cf. Sec. 3.1.2. For each configuration, observables are calculated from Eq. (4.9). Both quantities are obtained from a diagonalization of the $L \times L$ matrix representation of $\hat{H}_{\mathrm{el+ep}}(C)$ which dominates the computational complexity of the algorithm.

Technically, Monte Carlo simulations of Eq. (4.7) are related to disorder problems at finite temperature [147]. For each configuration C, we solve an Anderson model [156] with either diagonal (site) disorder for the Holstein model or off-diagonal (bond) disorder for the SSH model. In contrast to common disorder problems, the probability distribution $W(C)$ has a nontrivial dependence on $Z_{\mathrm{el+ep}}(C)$. However, in the high-temperature limit, $Z_{\mathrm{el+ep}}(C) \approx 1$ and $W(C)$ becomes a Gaussian distribution. We will revisit this analogy below.

Sampling

Simulations were started from random configurations which were then updated by randomly picking a single q_i and proposing a change Δq. Δq was drawn from a Gaussian distribution with variance σ_q^2. Because at high temperatures $W(C)$ is dominated by $\exp[-\beta H_{\mathrm{ph}}(C)]$, $\sigma_q \sim \sqrt{T}$ is a natural choice. However, at low temperatures, the distribution of displacements evolves into a two-peak structure [157] and $\sigma_q \sim \sqrt{T}$ becomes too sharp. Therefore, for each temperature, we performed a warmup to estimate the actual distribution of displacements. At low temperatures, the algorithm suffers from long autocorrelation times due to the local phonon updates. In our simulations, they were overcome by parallel tempering [158]. For each coupling parameter λ, the data shown were generated from a fixed temperature grid with at least 64 points. A switch of configurations at adjacent temperatures was proposed every 500 updates. We set $\mu = 0$ for half-filling and simulated lattices of length $L = 162$ with periodic boundary conditions.

Observables

In the following, we define the relevant static and dynamic observables. For each configuration C, they were calculated from the single-particle basis of $\hat{H}_{\mathrm{el}}(C)$ given by the eigenvalues E_λ and eigenvectors $|\lambda\rangle$.

The specific heat C_V was calculated via

$$C_V(C) = k_{\mathrm{B}}\beta^2 \left[\left\langle\!\left\langle \hat{H}^2 \right\rangle\!\right\rangle_C - \left\langle\!\left\langle \hat{H} \right\rangle\!\right\rangle_C^2 \right]. \tag{4.10}$$

To study the ordering of the electronic subsystem, we used the static structure factors

$$S_\alpha(q; C) = \frac{1}{L} \sum_{ij} e^{\mathrm{i}q(i-j)} \left\langle\!\left\langle \hat{O}_i^\alpha \hat{O}_j^\alpha \right\rangle\!\right\rangle_C \tag{4.11}$$

as a function of transferred momentum q. The subscript $\alpha = \rho$ ($\alpha = b$) denotes the charge (bond) structure factor. The corresponding operators $\hat{O}_i^\alpha$ are the local charge density $\hat{n}_i$ and bond density $\hat{B}_i$.

Importantly, spectral functions can be calculated directly for real frequencies, without the need of numerical analytic continuation. For the single-particle spectral function $A(k,\omega)$, the Lehmann representation reads[2]

$$A(k,\omega;C) = \sum_{\lambda} \left|\langle 0|\,\hat{c}_k\,|\lambda\rangle\right|^2 \delta(\omega - E_\lambda)\,. \tag{4.12}$$

From Eq. (4.12), the density of states $N(\omega)$ was obtained by summation over momentum k. Two-particle spectra were calculated from the dynamic structure factors

$$\begin{aligned} S_\alpha(q,\omega;C) = &\Big|\sum_{\lambda} n_{\mathrm{F}}(E_\lambda)\,\langle\lambda|\,\hat{O}_q^\alpha\,|\lambda\rangle\Big|^2 \delta(\omega) \\ &+ \sum_{\lambda\nu} n_{\mathrm{F}}(E_\nu)\,[1-n_{\mathrm{F}}(E_\lambda)]\,\left|\langle\lambda|\,\hat{O}_q^\alpha\,|\nu\rangle\right|^2 \delta(E_\lambda - E_\nu - \omega)\,, \end{aligned} \tag{4.13}$$

where $n_{\mathrm{F}}(E_\lambda) = \{\exp[\beta(E_\lambda-\mu)]+1\}^{-1}$ is the Fermi function and $\alpha = \rho, b$ as before. We also consider the real part of the optical conductivity

$$\sigma(\omega;C) = \frac{1}{\omega}\sum_{\lambda\nu}[n_{\mathrm{F}}(E_\nu) - n_{\mathrm{F}}(E_\lambda)]\,\left|\langle\lambda|\,\hat{J}\,|\nu\rangle\right|^2 \delta(E_\lambda - E_\nu - \omega)\,, \tag{4.14}$$

where $\hat{J} = \mathrm{i}\sum_i t_i(\hat{c}_i^\dagger \hat{c}_{i+1} - \hat{c}_{i+1}^\dagger \hat{c}_i)$ is the current operator; here $t_i = t$ for the Holstein model and $t_i = t - \alpha(q_{i+1} - q_i)$ for the SSH model, respectively.

Spectral functions were measured on a discrete frequency grid. Each data point represents the averaged spectral weight in an interval of width $\Delta\omega$. Unless stated otherwise we used $\Delta\omega/t = 0.04$.

4.1.3. Thermodynamics

We first discuss thermodynamic properties, focusing on the specific heat. The latter is an integrated quantity accessible to experiments that already captures the relevant temperature scales of the physical system.

Figure 4.2 shows the specific heat of both models as a function of temperature and for different couplings λ. For the large lattice size $L = 162$ used, only minor finite-size effects appear (see App. C.3). Note that adjacent data points in Fig. 4.2 are not statistically independent since they were generated by parallel tempering.

At $\lambda = 0$, the specific heat is the sum of contributions from the phonons and the electrons. In the adiabatic limit, the phonons are described by classical harmonic oscillators. According to the equipartition theorem, each phonon mode contributes $k_{\mathrm{B}}/2$, which leads to the constant background in Fig. 4.2. (For the SSH model, the $k = 0$ mode does not contribute because the length of the chain was fixed.) Therefore, C_V does

[2] For the classical Monte Carlo method, we define the spectral functions from a single-particle basis. In this form, they can be easily implemented in the algorithm. For a general many-body problem, these definitions do not hold. Rigorous definitions of spectral functions using a many-particle Fock basis are given in App. B.1.

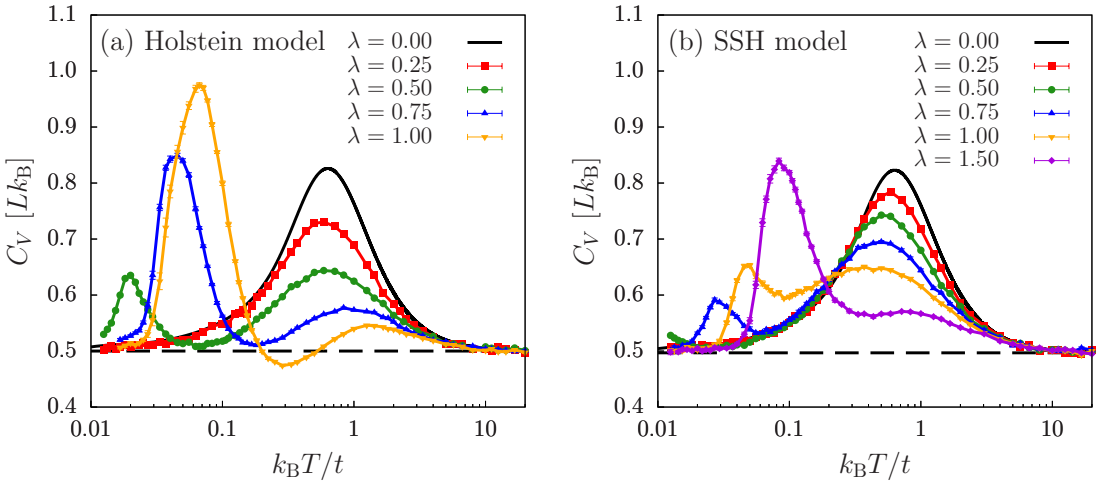

Figure 4.2.: Specific heat per site for (a) the spinless Holstein and (b) the spinless SSH model with $L = 162$. The dashed lines indicate the respective free-phonon contributions.

not vanish for $T \to 0$, in violation of the third law of thermodynamics. The electronic contribution reaches a maximum at the coherence temperature $k_BT/t \approx 0.63$ for free electrons and vanishes for $T \to 0$ and $T \to \infty$. The maximum is related to the thermal activation of charge fluctuations across the entire band width of our lattice model. The expected linear free-fermion contribution is visible in the interval $0.03 < k_BT/t < 0.1$ (for the system size $L = 162$ used) in a different representation.[3]

For $\lambda > 0$, the electronic and phononic contributions to C_V can no longer be separated. For the Holstein model, a small coupling $\lambda = 0.25$ suppresses C_V over the entire temperature range shown in Fig. 4.2(a). With increasing λ, the free-electron peak loses weight and shifts to higher temperatures. At $\lambda = 1$ and intermediate temperatures, the specific heat even falls below the free-phonon contribution. For the SSH model [Fig. 4.2(b)], C_V is also suppressed at high temperatures, but its maximum shifts to slightly lower temperatures. Moreover, C_V remains almost constant at intermediate temperatures.

For both models, an additional peak emerges in C_V at low temperatures. While for small λ the peak cannot be observed in the accessible temperature range, it shifts to higher temperatures and grows with increasing λ. This feature is robust against finite-size effects, only the downturn towards $T \to 0$ where the electronic contribution vanishes is not yet fully converged with L. For a detailed finite-size analysis see App. C.3.

The appearance of the low-temperature peak can be attributed to an enhancement of order as temperature is decreased. Figure 4.3 shows the static charge structure factor $S_\rho(q)$ for the Holstein model at $\lambda = 0.5$. At low temperatures, $S_\rho(q)$ develops a peak at $q = 2k_F = \pi$ that indicates the formation of a charge-density wave. Simultaneously, the peak in C_V arises, as shown in the two insets of Fig. 4.3. Its maximum at $k_BT/t \simeq 0.02$

[3] The representation chosen in Fig. 4.2 does not show the linear contribution to C_V for free fermions. However, it will become visible in the inset of Fig. 4.16 when we discuss the specific heat of the Holstein model in the antiadiabatic regime (cf. Sec. 4.2.4).

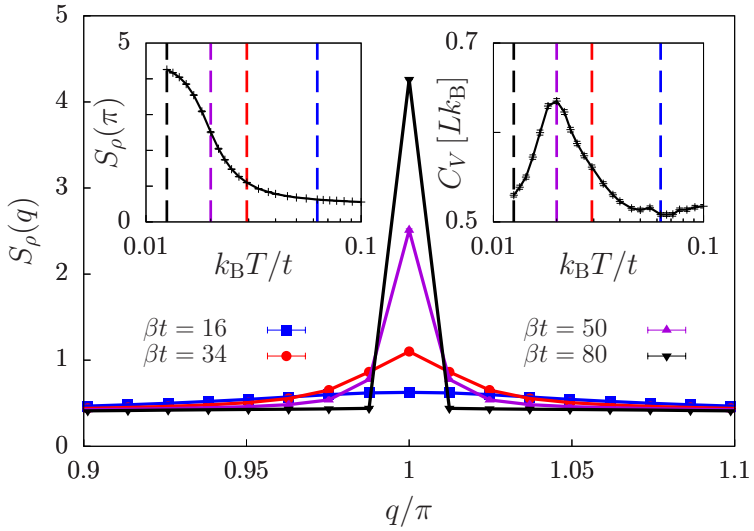

Figure 4.3.: Charge structure factor $S_\rho(q)$ of the spinless Holstein model around the ordering vector $q = 2k_\mathrm{F} = \pi$ for selected temperatures. The full temperature dependence of $S_\rho(\pi)$ is shown in the left inset. Dashed lines mark the temperatures for which $S_\rho(q)$ is shown in the main panel and match the evolution of the low-temperature peak in C_V, as shown in the right inset. Here, $\lambda = 0.5$ and $L = 162$.

corresponds with the inflection point of $S_\rho(\pi)$. The width of the peak is related to the temperature range where $2k_\mathrm{F}$ correlations become prominent. The same behavior is expected for the SSH model and the bond structure factor $S_b(q)$.

While true long-range order only exists at $T = 0$, the position of the low-temperature peak in C_V can be regarded as a coherence scale at which pronounced $2k_\mathrm{F}$ correlations set in and which marks the emergence of a clear Peierls energy gap. The thermal crossover is described by a correlation length $\xi(T)$ [159]. While $\xi(T) \to \infty$ for $T \to 0$, corresponding to long-range order, the correlation length is finite at $T > 0$ where charge or bond correlations decay exponentially. Similar results have been obtained from a Ginzburg-Landau approach [127]. While a saddle-point approximation gives a second-order phase transition at a finite $T_\mathrm{1D}^\mathrm{MF}$ and a jump in C_V [160], Scalapino *et al.* [127] used a functional method to treat fluctuations in the Ginzburg-Landau fields. Thereby, they mapped the 1D electron-phonon problem to a single quantum mechanical anharmonic oscillator [161]. In this approach, long-range order is destroyed at $T > 0$, and C_V is continuous with a peak similar to our results. The maximum in C_V may be located well below the mean-field value for $T_\mathrm{1D}^\mathrm{MF}$ [161]. For the electron-phonon models considered here, the mean-field critical temperature is an order of magnitude larger than the peak positions in our C_V data.

The results in Fig. 4.2 are very similar for the two models considered. With increasing λ, the free-electron contribution is suppressed and an additional low-temperature peak emerges that can be attributed to enhanced $2k_\mathrm{F}$ charge or bond correlations, respectively. The same temperature scales will also be relevant for the spectral properties discussed

in Sec. 4.1.4 and Sec. 4.1.5. The relation between C_V and the spectral function becomes apparent by considering the relation $C_V = \partial E/\partial T$ and using the equation of motion [162] to write the total energy as[4]

$$E = \frac{N_{\mathrm{ph}}}{2\beta} + \sum_k \int_{-\infty}^{\infty} d\omega \, \frac{\omega + \epsilon_k}{2} \, n_F(\omega) \, A(k,\omega) \, . \tag{4.15}$$

Here, $N_{\mathrm{ph}} = L$ for the Holstein model and $N_{\mathrm{ph}} = L - 1$ for the SSH model. According to Eq. (4.15), the total energy can be expressed as a sum rule of the single-particle spectrum weighted with the Fermi function $n_F(\omega)$ and the bare dispersion $\epsilon_k = -2t \cos k$. Thus, the specific heat measures the change of the density of states around the Fermi energy with temperature. The decrease of the free-electron peak in C_V with increasing λ therefore corresponds to a reduction of spectral weight across a broad region of energies and temperature, whereas the sharp low-temperature peak signals a sudden change in the single-particle spectrum. In particular, we will show that the emergence of the low-temperature peak is related to the Peierls gap.

4.1.4. Spectral properties of the Holstein model

In this and the next subsection, we investigate how the temperature-driven suppression of $2k_{\mathrm{F}}$ charge or bond order manifests itself in the single-particle and two-particle spectral functions [Eqs. (4.12)–(4.14)]. While at $T = 0$ the spectral functions can be calculated exactly using mean-field theory, finite temperatures require numerical simulations.

For the Holstein model, the electron-phonon coupling is chosen as $\lambda = 0.5$, for which the mean-field gap $\Delta/t \approx 0.68$ and the interesting temperature scale set by the corresponding peak in C_V is well accessible.

Temperature dependence of the density of states

We begin with the density of states plotted in Fig. 4.4. The filled curve shows the exact mean-field result at $T = 0$ which in the thermodynamic limit is given by

$$N(\omega) = \frac{L}{\pi} \frac{|\omega|}{\sqrt{\omega^2 - \left(\frac{\Delta}{2}\right)^2} \sqrt{(2t)^2 + \left(\frac{\Delta}{2}\right)^2 - \omega^2}} \tag{4.16}$$

for $\Delta/2 < |\omega| < \sqrt{(2t)^2 + (\Delta/2)^2}$, and zero else. Hence, at the mean-field level, the electron-phonon interaction opens a gap Δ at the Fermi level and shifts the upper edge of the band to higher energies. At the band edges, square-root singularities appear.

Thermal fluctuations lead to a broadening of the band edges and the singularities become finite peaks. At the lowest temperature considered in our simulation, $\beta t = 80$, $N(\omega)$ is still close to the result at $T = 0$, but spectral weight enters the mean-field gap exponentially. The fine structure visible in the middle of the bands is a finite-size effect and is partly smeared due to the use of a frequency grid with spacing $\Delta\omega$.

[4] For the Holstein model, a collection of sum rules for the total energy is given in App. B.3.

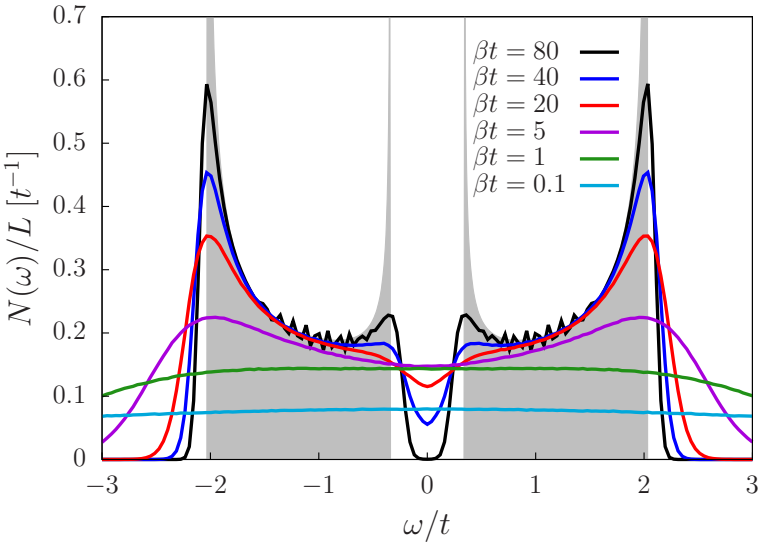

Figure 4.4.: Density of states of the spinless Holstein model for $\lambda = 0.5$ and $L = 162$. The filled curve corresponds to the $T = 0$ mean-field result (4.16).

With increasing temperature, the peak at the lower edge of the spectrum is strongly suppressed. At the same time, the $T = 0$ gap is filled in and has disappeared at $\beta t = 5$. At even higher temperatures, also the peak at the upper edge is entirely washed out. The weight is shifted to higher frequencies and the spectrum flattens completely.

The temperature of the gap closing in Fig. 4.4 coincides with the position of the low-temperature peak in C_V and the suppression of $2k_\mathrm{F}$ correlations in $S_\rho(q)$ in Fig. 4.3. According to Eq. (4.15), the change of $N(\omega)$ near the Fermi level is largest at $k_\mathrm{B}T/t \approx 0.02$ where C_V has its maximum. The peak in C_V directly signals the formation of the Peierls gap and the corresponding temperature can be regarded as the coherence scale at which the 1D Peierls physics appears. This temperature scale is considerably lower than the mean-field gap $\Delta/(2t) \approx 0.34$ or the critical temperature $k_\mathrm{B}T_\mathrm{1D}^\mathrm{MF}/t \approx 0.2$, similar to the reduction of the transition temperature due to 1D fluctuations in the functional Ginzburg-Landau approach of Refs. [127, 128].

Momentum dependence of the spectral functions

The single-particle spectrum $A(k,\omega)$ and the dynamic charge structure factor $S_\rho(q,\omega)$ are shown in Fig. 4.5. The temperatures were chosen to capture the interesting regions defined by the results for C_V in Fig. 4.2.

For $\beta t = 80$ [Fig. 4.5(a)], $A(k,\omega)$ closely follows the mean-field dispersion indicated by the dashed line. The imbalance of spectral weight between the original cosine dispersion and the shadow bands is characteristic for systems with competing periodicities and only disappears for $\lambda \to \infty$ [163]. Due to the finite temperature, the peaks in $A(k,\omega)$ are broadened and their positions deviate slightly from the mean-field dispersion at the

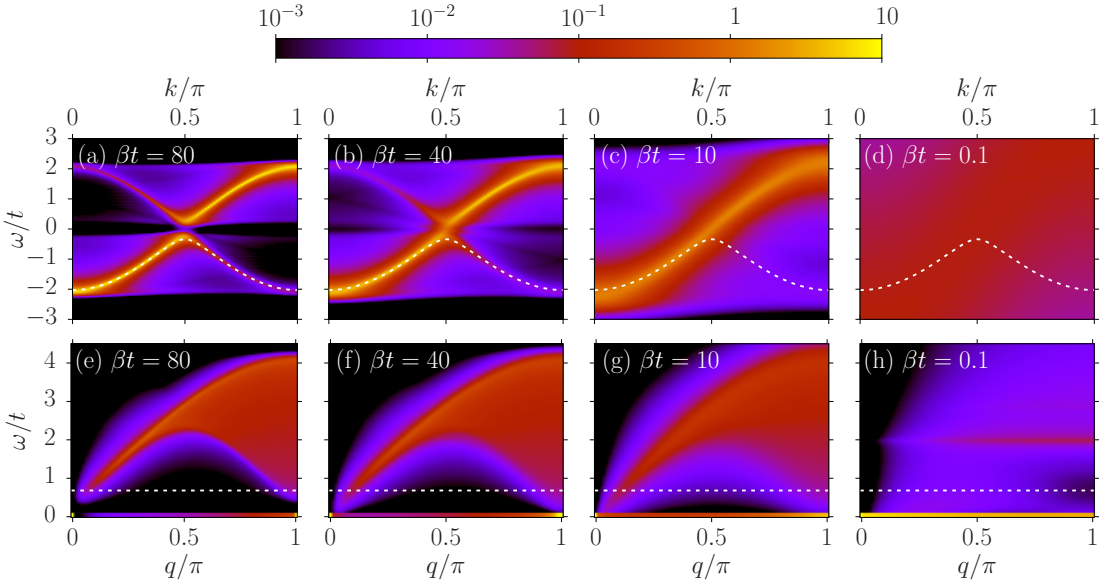

Figure 4.5.: (a)–(d) Single-particle spectral function $A(k,\omega)$ and (e)–(h) dynamic charge structure factor $S_\rho(q,\omega)$ of the spinless Holstein model for $\lambda = 0.5$ and $L = 162$. Dashed lines correspond to the $T = 0$ mean-field dispersion and gap, respectively. For better visibility, the $\omega = 0$ contributions to $S_\rho(q,\omega)$ are shown as a bar of width $\Delta\omega/t = 0.1$ in (e)–(h).

band edges. There are additional features of minor weight that disperse from the edges of the original cosine band forming a continuum of excitations.

With increasing temperature [Fig. 4.5(b)], the broadening of the single-particle spectrum becomes larger and the shadow bands less pronounced. Inside the mean-field gap, two dispersing bands appear with dominant weight around $k_\mathrm{F} = \pi/2$ (see also the discussion below). At $\beta t = 10$ [Fig. 4.5(c)], the gap and the shadow bands have disappeared completely, and the locus of spectral weight follows the cosine dispersion of the noninteracting system. Further increasing the temperature only leads to a broadening of the spectrum until it becomes washed out completely, see Fig. 4.5(d).

Figures 4.5(e)–(h) show the dynamic charge structure factor $S_\rho(q,\omega)$ at the same temperatures. At $\beta t = 80$, $S_\rho(q,\omega)$ exhibits a particle-hole continuum but with a gap comparable to the mean-field gap (dashed line). Moreover, there is a sharp central (Bragg) peak at $q = 2k_\mathrm{F} = \pi$ associated with CDW order. At higher temperature [Figs. 4.5(f)–(g)], the edges of the particle-hole continuum diffuse, the gap is filled in, and the central peak becomes a Lorentzian of width $\xi^{-1}(T)$ in momentum space (cf. Fig. 4.3) where $\xi(T)$ is the correlation length introduced at the beginning of Sec. 4.1.3. In the high-temperature limit [Fig. 4.5(h)] the particle-hole continuum is washed out completely, and $S_\rho(q,\omega)$ contains (i) a spatially localized (i.e., q-independent) zero-energy Einstein phonon mode, and (ii) an additional mode at $\omega = 2t$ related to the strong onsite disorder generated for the fermions by the lattice fluctuations (see Sec. 4.1.6).

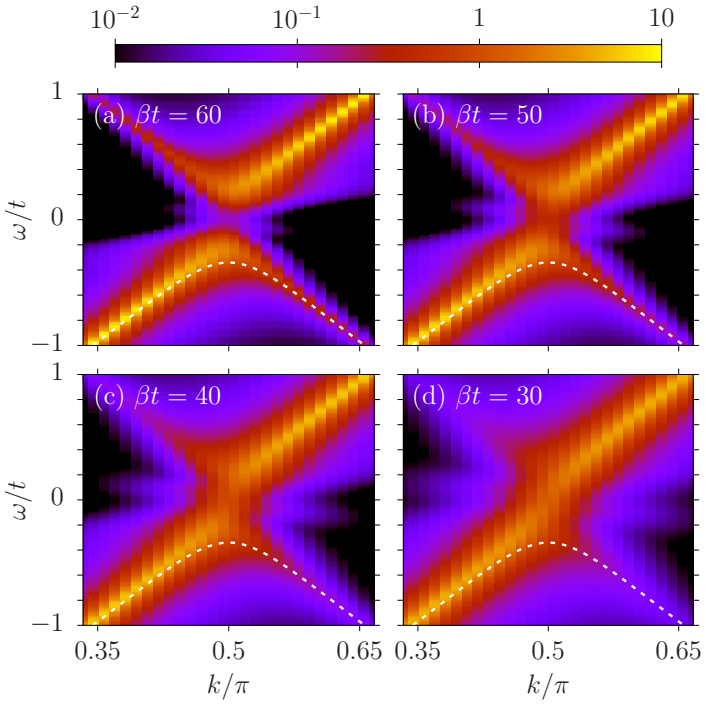

Figure 4.6.: Close-up of the single-particle spectral function $A(k,\omega)$ around $k_\mathrm{F} = \pi/2$ for the same parameters as in Fig. 4.5. The dashed lines correspond to the mean-field dispersion at $T = 0$. Here, we used a discretization $\Delta\omega/t = 0.01$.

Closing of the single-particle gap

The closing of the single-particle gap in Fig. 4.5 is the result of two effects: (i) a spatially homogeneous renormalization of the $T = 0$ mean-field order parameter and (ii) thermally induced defects in the lattice dimerization with energies below the band gap.

A closeup of the thermally induced low-energy excitations is shown in Fig. 4.6. For $\beta t = 60$ [Fig. 4.6(a)], we see a band above (below) the mean-field main band for $k < k_\mathrm{F}$ ($k > k_\mathrm{F}$), as well as a weaker band below (above) the mean-field shadow band for $k < k_\mathrm{F}$ ($k > k_\mathrm{F}$) that extends only over a small range of k around k_F. Both features merge with the mean-field bands near k_F. With increasing temperature, the additional excitations gain spectral weight (especially close to k_F) and the feature following the shadow bands extends over a large k-range. Eventually, the gap is filled in and the linear dispersion near k_F is restored, cf. Figs. 4.6(c), 4.6(d), and 4.5(c).

At low temperatures [Fig. 4.5(a)], the spectral function has a close resemblance with that of the spinless Holstein model with quantum phonons, which is shown in Fig. 4.13(b) and will be discussed in detail in Sec. 4.2.2. At finite phonon frequencies, $A(k,\omega)$ exhibits dispersive excitations with energy smaller than the mean-field gap that have been interpreted as polaron excitations [71]. While quantum fluctuations reduce the minimal energy for polaron excitations [71], the latter coincides with the mean-field gap in the adiabatic limit [Fig. 4.5(a)].

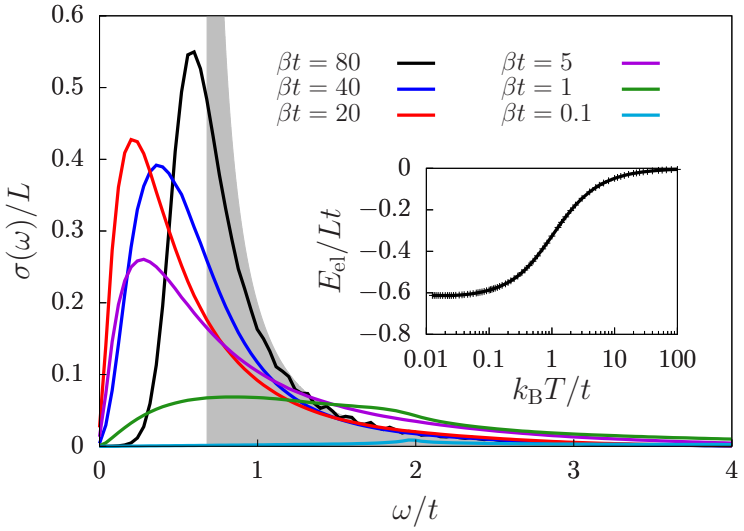

Figure 4.7.: Optical conductivity of the spinless Holstein model for $\lambda = 0.5$ and $L = 162$. The filled curve is the $T = 0$ mean-field result (4.17). The inset shows the kinetic energy of the electrons as a function of temperature. It is related to $\sigma(\omega)$ by the sum rule (4.18).

Optical conductivity

Finally, we consider the optical conductivity $\sigma(\omega)$ in Fig. 4.7. At $T = 0$, mean-field theory gives

$$\sigma(\omega) = \frac{L\Delta^2}{4\pi\omega^2}\sqrt{\frac{(4t)^2 + \Delta^2 - \omega^2}{\omega^2 - \Delta^2}} \tag{4.17}$$

for $\Delta < |\omega| < \sqrt{(4t)^2 + \Delta^2}$. The filled curve in Fig. 4.7 clearly shows the square-root singularity at the lower edge $\omega = \Delta$. In contrast to the density of states, there is no singularity at the upper edge where $\sigma(\omega) = 0$. At $\beta t = 80$, the lower edge of $\sigma(\omega)$ has already broadened significantly. As a function of temperature, we first observe a decrease of the optical gap due to the suppression of charge order. While this shift is qualitatively captured by a temperature-dependent mean-field gap $\Delta(T)$, the latter does not account for the nontrivial broadening due to fluctuations. Although the single-particle gap is filled in at high temperatures, there is no Drude peak. The absence of the latter, and the shift of the peak in $\sigma(\omega)$ back to larger frequencies for $\beta t \lesssim 20$, can be attributed to the onset of incoherence. By contrast, in the mean-field CDW approximation, $\Delta = 0$ at $T > T_{\mathrm{1D}}^{\mathrm{MF}}$ so that the electrons can move coherently. At even higher temperatures, the strong lattice fluctuations act as essentially random disorder. A characteristic peak emerges at $\omega = 2t$ that becomes more pronounced as temperature increases further. The relation to a disorder problem will be discussed in more detail in Sec. 4.1.6.

The integrated optical conductivity is related to the kinetic energy of the electrons

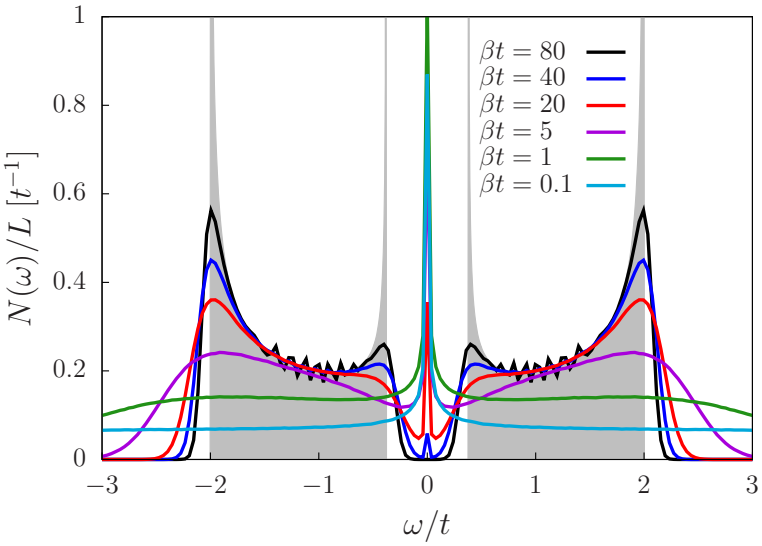

Figure 4.8.: Density of states of the spinless SSH model for $\lambda = 0.75$ and $L = 162$. The filled curve corresponds to the $T = 0$ mean-field result (4.19).

via the f-sum rule [164]

$$\int_0^\infty d\omega\, \sigma(\omega) = -\frac{\pi}{2} E_{\mathrm{el}}\,. \tag{4.18}$$

The results for E_{el} in the inset of Fig. 4.7 reveal that up to $\beta t \approx 20$ spectral weight is merely redistributed, whereas it is significantly reduced at higher temperatures and vanishes for $T \to \infty$.

4.1.5. Spectral properties of the Su-Schrieffer-Heeger model

The spectral properties of the SSH model are in many aspects similar to the Holstein model, and we therefore focus on the differences. To facilitate a comparison with the results for the Holstein model we take $\lambda = 0.75$ for which the mean-field gap $\Delta/t \approx 0.76$.

Temperature dependence of the density of states

Figure 4.8 shows the density of states, including the $T = 0$ mean-field result given by

$$N(\omega) = \frac{L}{\pi} \frac{|\omega|}{\sqrt{\omega^2 - \left(\frac{\Delta}{2}\right)^2}\sqrt{(2t)^2 - \omega^2}} \tag{4.19}$$

for $\Delta/2 < |\omega| < 2t$, and zero otherwise. Equation (4.19) has the same form as Eq. (4.16), but the upper edge of the spectrum remains at $\omega = 2t$ independent of λ. The temperature dependence of the mean-field bands, i.e., the broadening of the singularities and the closing of the gap, is similar to the Holstein model. However, there is an additional

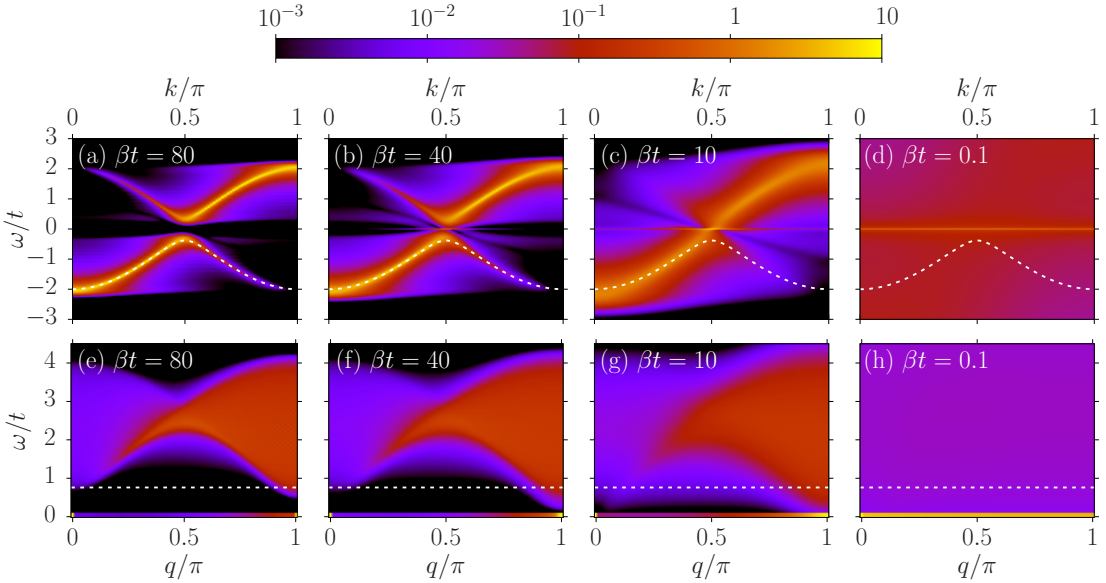

Figure 4.9.: (a)–(d) Single-particle spectral function $A(k,\omega)$ and (e)–(h) dynamic bond structure factor $S_b(q,\omega)$ of the spinless SSH model for $\lambda = 0.75$ and $L = 162$. The dashed lines correspond to the $T = 0$ mean-field dispersion and gap, respectively. For better visibility, the $\omega = 0$ contributions to $S_b(q,\omega)$ are shown as a bar of width $\Delta\omega/t = 0.1$ in (e)–(h).

peak at $\omega = 0$ that grows and broadens with increasing temperature. It survives even at the highest temperature considered where the rest of the spectrum has been completely washed out by thermal fluctuations. As discussed below, the peak is related to topologically protected midgap states of the SSH Hamiltonian.

Momentum dependence of the spectral functions

The single-particle spectral function $A(k,\omega)$ shown in Figs. 4.9(a)–(d) is again very similar to the Holstein model, except for the zero-energy peak. The latter is absent at $\beta t = 80$ [Fig. 4.9(a)], where the spectrum closely follows the mean-field dispersion. It first emerges at $\beta t \simeq 40$ when the gap starts to be filled in by thermal excitations [Fig. 4.9(b)]. At $\beta t = 10$ [Fig. 4.9(c)], the mean-field gap is filled in but signatures of the shadow bands remain. More noticeably, the zero-energy peak is well visible for all k with maximal spectral weight at k_F. Finally, increasing the temperature further to $\beta t = 0.1$ completely smears out the spectrum except for the $\omega = 0$ peak [Fig. 4.9(d)]; in this regime, the spectral weight of the peak becomes independent of k.

The results for the dynamic bond structure factor are shown in Figs. 4.9(e)–(h). At the lowest temperature considered [Fig. 4.9(e)], it has a continuum of excitations above the mean-field gap and zero-energy peaks at $q = 0$ and $q = 2k_\mathrm{F} = \pi$. The evolution with temperature is similar to Fig. 4.5. In particular, the gap is filled in and the Lorentzian central peak widens due to the decrease of $\xi(T)$. In the high-temperature limit [Fig. 4.9(h)], sharp excitations exist only at $\omega = 0$.

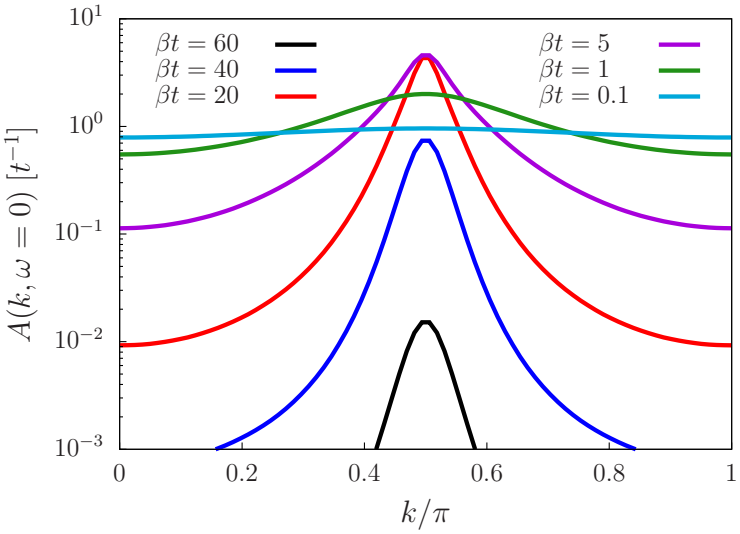

Figure 4.10.: Temperature dependence of the zero-energy peak in $A(k,\omega)$ as a function of momentum k for the spinless SSH model for $\lambda = 0.75$ and $L = 162$. The spectrum was averaged over an interval $\Delta\omega/t = 0.04$ around $\omega = 0$. Hence, the extent of the peak in frequency is not captured.

Localization of the zero-energy mode

We attribute the zero-energy mode in the single-particle spectrum to soliton states at thermally generated domain walls between different lattice dimerizations [8, 143]. We can estimate the spatial extent of these states from their momentum dependence, which is shown in Fig. 4.10. At low temperatures, the shape of the peak hardly changes, only its spectral weight becomes larger. A comparison with the analytic result for the soliton wave function [143], $\phi_0(n) \sim \mathrm{sech}(n/l)\cos(\pi n/2)$, gives a localization length of $l \approx 5$ in units of the lattice spacing, in agreement with Ref. [143]. As the temperature exceeds $\beta t = 20$, the peak in Fig. 4.10 broadens in k-space and the localization length becomes smaller. In the high-temperature limit, the zero-energy state becomes completely localized. Although the picture of domain walls between ordered regions breaks down when the single-particle gap closes, the zero mode persists at higher temperatures [Fig. 4.9(d)] where it can be understood as a disorder effect, see Sec. 4.1.6.

Optical conductivity

The optical conductivity $\sigma(\omega)$ is shown in Fig. 4.11. At $T = 0$, the mean-field result is given by

$$\sigma(\omega) = \frac{4L\Delta^2 t^2}{\pi\omega^2} \frac{1}{\sqrt{\omega^2 - \Delta^2}} \frac{1}{\sqrt{(4t)^2 - \omega^2}} \tag{4.20}$$

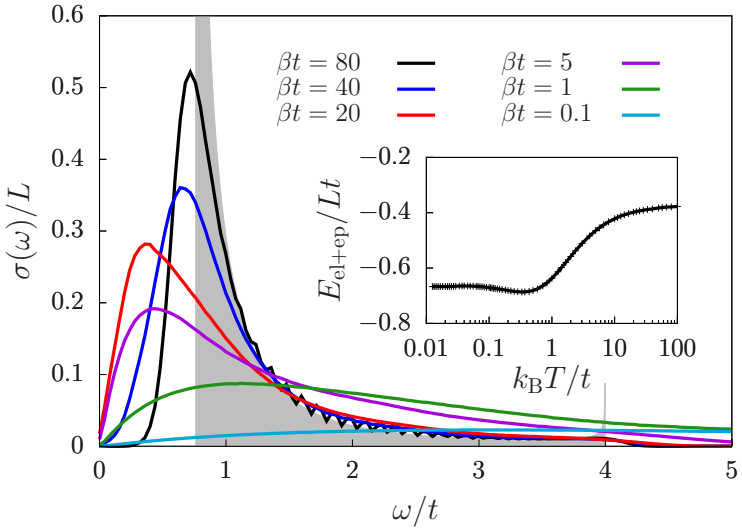

Figure 4.11.: Optical conductivity of the spinless SSH model for $\lambda = 0.75$ and $L = 162$. The filled curve is the $T = 0$ mean-field result (4.20). The inset shows the energy of the electronic subsystem as a function of temperature. It is related to $\sigma(\omega)$ by the sum rule (4.21).

for $\Delta < |\omega| < 4t$, otherwise it is zero. Compared to the Holstein model, it has an additional square-root singularity at the upper edge of the spectrum. However, its integrated weight is too small to be visible even at the lowest temperature considered. The lower edge first broadens and then also shifts to lower frequencies. Similar to the Holstein model, up to $\beta t \approx 10$ spectral weight is only redistributed, as visible from the inset of Fig. 4.11. The integrated spectrum is related to the energy of the electronic subsystem via the sum rule [164]

$$\int_0^\infty d\omega\, \sigma(\omega) = -\frac{\pi}{2} E_{\mathrm{el+ep}}\,. \tag{4.21}$$

In contrast to the Holstein model, the sum rule also includes the interaction energy of electrons and phonons. Because of this contribution, the integrated weight slightly increases between $\beta t \approx 10$ and $\beta t \approx 3$. Further increasing the temperature leads to a reduction of spectral weight at small ω and a substantial enhancement of the tail at large ω. In contrast to the Holstein model, the integrated weight does not vanish for $T \to \infty$.

4.1.6. Relation to disorder problems

At high temperatures, the essentially random lattice distortions act as disorder for the electrons [147], corresponding to site disorder for the Holstein model, and bond disorder for the SSH model. The probability distribution $W(C)$ [Eq. (4.8)] becomes a Gaussian and the disorder strength scales as $\sqrt{\lambda T}$. The connection to disordered noninteracting models explains some of the spectral features observed above.

For the Holstein model, the strong onsite disorder leads to two distinct peaks in the two-particle spectra [Figs. 4.5(h) and 4.7], one at $\omega = 0$ in $S_\rho(q,\omega)$, and another at $\omega = 2t$ both in $S_\rho(q,\omega)$ and $\sigma(\omega)$. The zero-energy peak in $S_\rho(q,\omega)$ does not show any q dependence, whereas the peak at $\omega = 2t$ is strongest around $q = \pi$, but vanishes at $q = 0$. The latter signature also appears in $\sigma(\omega)$, where it has already been observed for the t–V model at strong disorder [165] and the Holstein polaron in the adiabatic regime [166]. This signature becomes even sharper as temperature is increased further. In Ref. [166], the resonance at $\omega = 2t$ has been explained from an effective two-site model, where the bonding and antibonding eigenstates of the electron perfectly overlap with the current operator. In the same way, $\hat{n}_q$ connects the different-parity states at $q = \pi$, whereas the overlap is zero at $q = 0$.

For the SSH model, only the zero-energy peak appears in the high-temperature limit of $S_b(q,\omega)$. Moreover, an excitation with $\omega = 0$ is visible in the single-particle spectrum and persists for $T \to \infty$. Such a peak has previously been observed for the SSH polaron [155] and explained as a disorder effect [167–170]. For the tight-binding model, any finite off-diagonal disorder leads to a zero-energy peak in the density of states that becomes larger and broadens as the disorder strength increases [168]. The appearance of the peak is related to the chiral symmetry of the SSH Hamiltonian. The latter is broken by onsite disorder, and the zero mode disappears accordingly [168]. Moreover, no zero mode exists for the Holstein model for which chiral symmetry is broken already at the mean-field level. While we have so far interpreted the zero-energy excitations at low temperatures in terms of topologically protected soliton states located at domain walls, such states can also be induced by off-diagonal disorder acting on the dimerized ground state [171–174].

At low temperatures, the broadening of the spectral functions can be considered as a disorder effect, including the tail of the optical conductivity extending into the mean-field gap. For the Holstein model, it is related to the weak pinning of a charge-density wave by onsite disorder [175]. For the SSH model, similar results were also obtained from the fluctuating gap model, where order parameter fluctuations are modeled as off-diagonal disorder [173, 174, 176–178].

4.2. Quantum Peierls chains

In the previous section, we investigated the effects of thermal fluctuations on the dimerized ground state of adiabatic Peierls chains. For the Holstein model as well as the SSH model we found a low-temperature peak in C_V related to the closing of the single-particle gap by soliton-antisoliton excitations that appear at domain walls and considerably reduce the $2k_\mathrm{F}$ correlations. In real materials, phonon frequencies are often small but finite, and numerical simulations show that quantum lattice fluctuations can even drive a phase transition to a metallic state. To obtain a comprehensive understanding of 1D Peierls materials, it is therefore necessary to study the effects of finite phonon frequencies.

In the following, we show results for the specific heat of the spinless Holstein model as a function of the phonon frequency ω_0 and discuss for which parameters the adiabatic

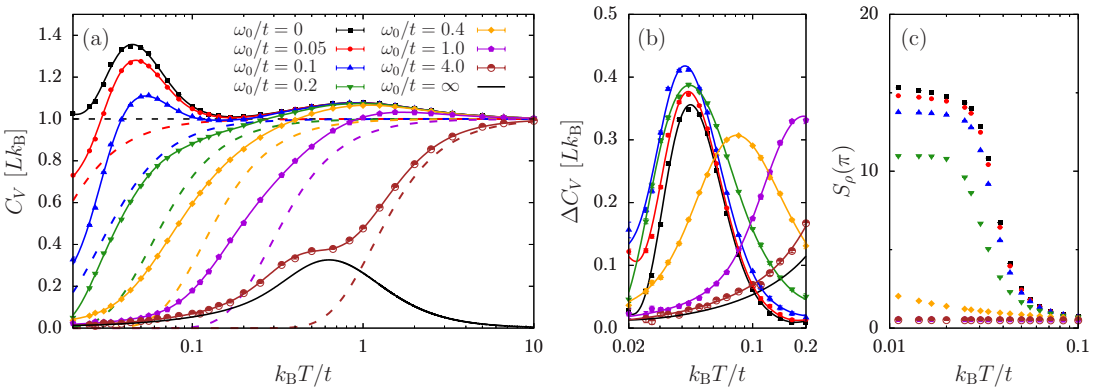

Figure 4.12.: (a) Specific heat of the spinless Holstein model for different ω_0. Data points correspond to direct estimates of C_V, whereas straight lines are obtained from fits to the total energy using the maximum entropy method (for details see App. C). Dashed lines indicate the free-phonon contributions. (b) Specific heat subtracted by the corresponding free-phonon contribution. (c) Charge structure factor at the ordering vector $q = \pi$. We used $\lambda = 0.75$ and $L = 162$. Results were obtained using the SSE representation.

approximation is satisfied. We also study C_V in the adiabatic and antiadiabatic regimes. In the adiabatic regime, we use the single-particle spectral functions obtained from the CT-INT method [71] to explain the key effects of quantum lattice fluctuations at low-temperatures. In contrast to the adiabatic limit, we do not show results for the SSH model. Since the phase diagram of the spinless SSH model with optical phonons is very similar to the spinless Holstein model [P6], we expect similar thermodynamic properties. A study of the SSH model with acoustic phonons is out of reach due to a sign problem.

4.2.1. Crossover from the adiabatic to the antiadiabatic regime

Figure 4.12(a) shows C_V as a function of the phonon frequency ω_0 ranging from the adiabatic to the antiadiabatic limit. We fixed the electron-phonon coupling to $\lambda = 0.75$. Here and in the following, simulations were performed using the directed-loop algorithm presented in Sec. 3.4 and reached lattice sizes of up to $L = 162$. Data points in Fig. 4.12(a) correspond to direct measurements of C_V from the covariance estimator $C_V = k_B\beta^2(\langle\hat{H}^2\rangle - \langle\hat{H}\rangle^2)$, whereas solid lines serve as a guide to the eye and are obtained from fits to the total energy using the maximum entropy method [179] and applying $C_V = \partial E/\partial T$. A detailed discussion of both estimators is given in App. C.

Starting from the adiabatic limit at $\omega_0 = 0$, Fig. 4.12(a) reveals that quantum lattice fluctuations successively reduce the specific heat for temperatures $k_BT < \omega_0$ as ω_0 becomes larger. By contrast, the adiabatic approximation is satisfied for $k_BT \gtrsim \omega_0$, where the data for different ω_0 coincide. As expected from the fundamental laws of thermodynamics, we find $C_V \to 0$ for $T \to 0$ and $C_V \to Lk_B$ for $T \to \infty$. These limiting cases already are a feature of free phonons with $\omega_0 > 0$ and their contributions to C_V for different ω_0 are illustrated by dashed lines in Fig. 4.12(a). As a function of ω_0, the maximum

of the low-temperature peak in C_V is reduced and finally disappears when approaching the critical value $\omega_{0,c}/t \approx 0.5$, where a $T = 0$ transition from a Peierls insulator to a Luttinger liquid takes place. In the Luttinger liquid phase, the low-temperature behavior of C_V is fundamentally different from the Peierls phase and is expected to show a linear temperature dependence. This contribution will be discussed in detail in the subsequent sections. By further increasing the phonon frequency, we enter the antiadiabatic regime ($\omega_0 > t$). Here, the electron and phonon contributions to C_V separate and are approximately described by their noninteracting contributions, e.g., at $\omega_0/t = 4.0$. Finally, the spinless Holstein model maps to free electrons for $\omega_0 \to \infty$.

To test the validity of the adiabatic approximation in the Peierls phase, we take a closer look at the low-temperature behavior of C_V for phonon frequencies $\omega_0/t \lesssim 0.2$. In Fig. 4.12(a), the C_V data for different ω_0 are difficult to compare, because already the contributions of free phonons (dashed lines) drop to zero at different energy scales. We can get rid of this effect by subtracting the free-phonon contributions from C_V. The resulting ΔC_V is shown in Fig. 4.12(b) and suggests that the adiabatic approximation is excellent for phonon frequencies $\omega_0/t \lesssim 0.1$ and still satisfactory for $\omega_0/t = 0.2$.[5] In particular, the coherence temperature below which the 1D Peierls physics can be observed is related to the peak position in ΔC_V (cf. Sec. 4.1.3) and appears to be the same for all $\omega_0/t \leq 0.2$. Further evidence for a fixed coherence scale comes from the charge structure factor $S_\rho(\pi)$ at the ordering vector $q = 2k_\mathrm{F} = \pi$ shown in Fig. 4.12(c). For every $\omega_0/t \leq 0.2$, the onset of enhanced CDW correlations takes place at the same temperature scale. Furthermore, at low temperatures the absolute values of $S_\rho(\pi)$ are very similar for $\omega_0/t \leq 0.1$. The relation between enhanced CDW correlations and the peak position in C_V was also demonstrated in Fig. 4.3 for the adiabatic limit.

4.2.2. Spectral functions in the adiabatic regime

The specific heat is fully determined by the single-particle spectral functions $A(k,\omega)$ and $B(q,\omega)$ of electrons and phonons. A collection of exact sum rules is given in App. B.1. In the adiabatic limit, $C_V(T)$ can be understood solely from the electronic spectral function $A(k,\omega)$ and its temperature dependence, as shown in Sec. 4.1. In the presence of quantum lattice fluctuations, also the phonon dynamics contained in $B(q,\omega)$ must be considered to explain the temperature dependence of C_V. Unlike in the adiabatic limit where a classical Monte Carlo method provided access to spectral functions directly on the real-frequency axis, QMC methods can only access correlation functions in imaginary time. $A(k,\omega)$ and $B(q,\omega)$ are then obtained from numerical analytic continuation which is an ill-posed numerical problem. For this reason, the spectral functions discussed below cannot show the same accuracy as in the adiabatic limit and a study of their temperature dependence is out of reach. However, our results for $\omega_0 = 0$ revealed that thermal fluctuations mainly lead to a broadening of the $T = 0$ spectra, with some additional features related to thermally generated lattice defects. Therefore, we believe that already

[5] Note that subtracting the free-phonon contribution from C_V is only satisfied deep in the Peierls phase, where renormalization effects of the phonon dispersion are small. By further increasing ω_0, this approximation breaks down as shown for the phonon spectral functions in Sec. 4.2.2.

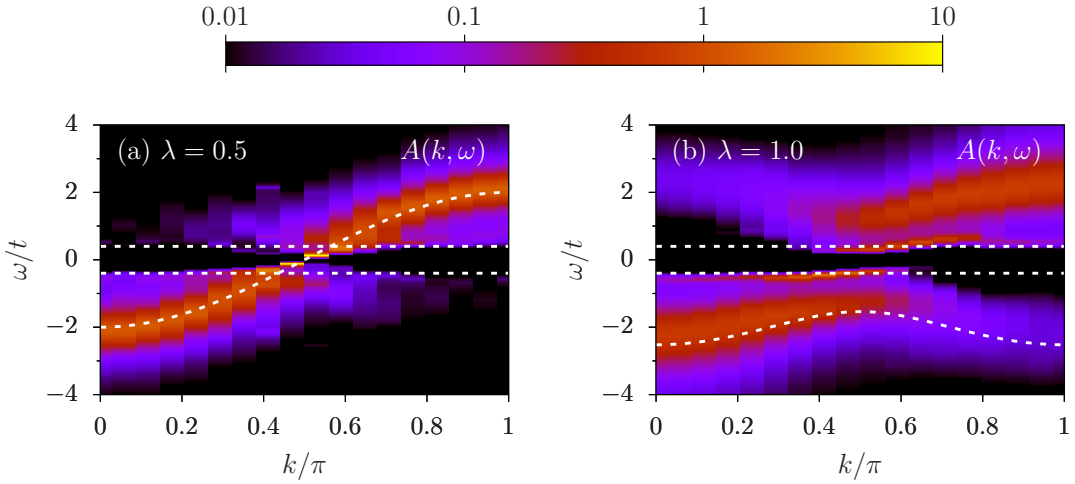

Figure 4.13.: Electronic single-particle spectral function $A(k,\omega)$ of the spinless Holstein model in the (a) Luttinger liquid phase ($\lambda = 0.5$) and (b) Peierls phase ($\lambda = 1.0$). Dashed lines indicate $\omega = \pm\omega_0$ as well as the free-electron dispersion in (a) and the lower band of the mean-field dispersion in (b). Here, $\omega_0/t = 0.4$ and $L = \beta t = 34$. Data are taken from Ref. [71] and were obtained using the CT-INT method.

the low-temperature properties of $A(k,\omega)$ and $B(q,\omega)$ will give considerable insight for the interpretation of the C_V data.

In this section, we discuss the electronic and phononic single-particle spectra for $\omega_0/t = 0.4$, as obtained from the CT-INT method. A brief discussion of spectral features in the antiadiabatic regime is included in Sec. 4.2.4. A short summary of the analytic continuation problem and references to the methods used can be found in App. B.1.

Electronic spectral function

We study the single-particle spectral function as defined by the Lehmann representation

$$A(k,\omega) = \frac{1}{Z}\sum_{mn} e^{-\beta E_m}\left(1 + e^{-\beta\omega}\right)\left|\langle m|\,\hat{c}_k\,|n\rangle\right|^2 \delta[\omega - (E_n - E_m)]\,. \tag{4.22}$$

Here, $|m\rangle$ is a many-particle eigenstate of the Hamiltonian and E_m the corresponding eigenvalue. For further details see App. B.1.

Figure 4.13(a) shows $A(k,\omega)$ in the Luttinger liquid phase for $\lambda = 0.5$. The dominant part of the spectrum closely follows the free-electron dispersion indicated by a dashed line. Almost all spectral features are substantially broadened by incoherent phonon scattering [180] and thermal fluctuations, only inside an energy window $\omega \in [-\omega_0, \omega_0]$ around the Fermi level and near $k_F = \pi/2$ $A(k,\omega)$ has sharp and gapless excitations. As discussed in Ref. [71], these low-energy excitations are very similar to bosonization results [181]. At $k = k_F$, the bosonization results of Ref. [181] include a sharp and dominant peak at $\omega = 0$ as well as additional phonon satellites at $\omega = \pm\omega_0$ of low spectral

weight. When $|k - k_F|$ increases, the sharp excitation at the Fermi level disperses with a renormalized velocity, loses spectral weight, and broadens. Simultaneously, the phonon peaks at $\omega = \pm\omega_0$ increase in spectral weight and finally merge into the broad cosine band. The QMC results at finite system sizes $L = \beta t = 34$ shown in Fig. 4.13(a) are consistent with those obtained from bosonization. In particular, one can infer a renormalization of the Fermi velocity from the QMC data. This renormalization is caused by the formation of polarons—electrons that are dressed by phonons—with an increased effective mass. The reduction of the charge velocity will be discussed below with our results for C_V.

Figure 4.13(b) shows $A(k, \omega)$ in the Peierls phase for $\lambda = 1$. The spectrum is gapped and consists of four well-separated features that appear symmetrically around $\omega = 0$: two high-energy bands and two low-energy bands (near $\omega = 0$). The high-energy bands follow the mean-field dispersion (drawn as a dashed line in the lower half of the spectrum) and include the shadow bands characteristic for the doubling of the unit cell. The broadening of these bands is again a result of thermal fluctuations and incoherent phonon scattering [180]. In contrast to the mean-field result, $A(k, \omega)$ shows additional dispersing features inside the mean-field gap that define the real Peierls gap. In Ref. [71], these features were identified as polaron bands. In contrast to the adiabatic limit, where polarons are only observed as thermal excitations, these features are expected to remain at zero temperature. However, with increasing λ their weight will become smaller.

Reference [71] establishes a connection between the spectral features of the Peierls phase and the Luttinger liquid phase. In the latter, the bosonization results of Ref. [181] essentially show two features: the phonon peaks at $\omega = \pm\omega_0$ and the gapless low-energy contribution identified as the polaron band. Because the Peierls transition is a continuous phase transition, the low-energy feature continuously evolves into the gapped polaron band with a finite Peierls gap, whereas the high-energy feature becomes the mean-field band at large λ [71]. Thereby, the Peierls gap is expected to open exponentially slowly, as it is characteristic for a Berezinskii-Kosterlitz-Thouless transition.

Phonon spectral function

Previous results for the spinless Holstein model suggest that in the adiabatic regime, the phonon dispersion softens at and around the ordering wavevector $q = \pi$ on approaching λ_c from the metallic phase [27, 71, 182, 183, P5]. For a soft-mode transition, the phonon mode should become completely soft at $q = \pi$ and $\lambda = \lambda_c$, and subsequently harden for $\lambda > \lambda_c$. Indications for such a hardening were recently observed for the spinful Holstein model [P5], but a clear identification is complicated by the dominant central peak in the Peierls phase [71, P5] and—in the case of exact diagonalization—the small system sizes accessible at strong coupling [27].

Here, we consider the phonon spectral functions

$$B_\alpha(q, \omega) = \frac{1}{Z} \sum_{mn} e^{-\beta E_m} \left| \langle m | \hat{O}_q^\alpha | n \rangle \right|^2 \delta[\omega - (E_n - E_m)] \tag{4.23}$$

calculated either from the displacement [$\alpha = Q$, Eq. (2.27)] or the momentum correlation function [$\alpha = P$, Eq. (2.28)], with $\hat{O}^Q = K^{1/2}\hat{Q}$ and $\hat{O}^P = M^{-1/2}\hat{P}$. In principle,

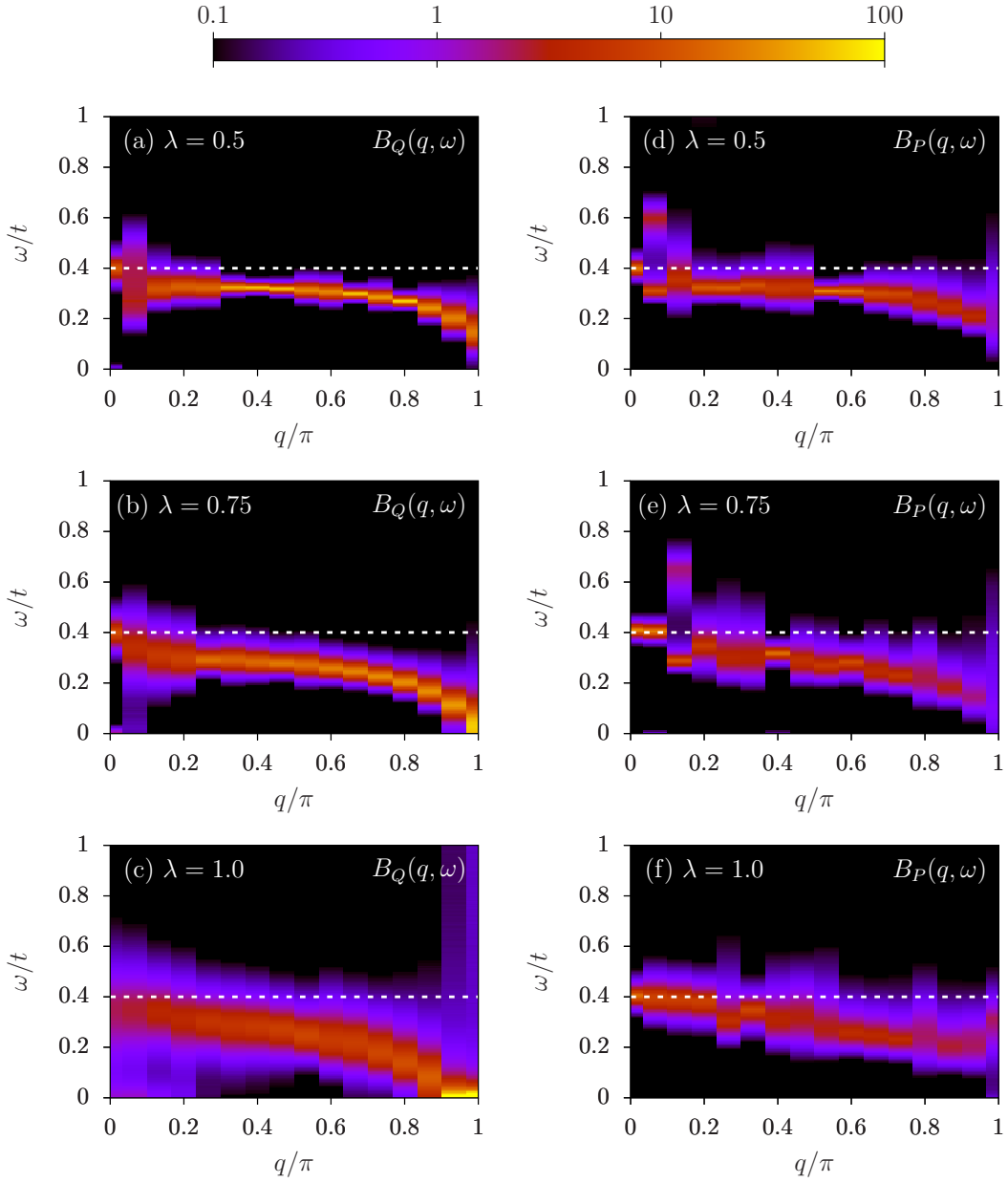

Figure 4.14.: Phonon spectral functions $B_Q(q,\omega)$ [(a)–(c)] and $B_P(q,\omega)$ [(d)–(f)] for the spinless Holstein model. Dashed lines correspond to $\omega_0/t = 0.4$. Here, $L = \beta t = 30$. Results were obtained with the CT-INT method.

both spectral functions contain the same information, but spectral weights may differ significantly. In particular, the QMC estimators (3.46) and (3.47) derived in the previous chapter may be subject to different statistical fluctuations that affect the analytic continuation. Our discussion of the phonon spectral functions is based on Ref. [P3].

The displacement spectrum $B_Q(q,\omega)$ in Fig. 4.14(a) reveals the softening of the phonons near $q = \pi$ in the metallic phase. Near the critical point, the dispersion appears completely soft at $q = \pi$ [Fig. 4.14(b)], and the spectrum is dominated by a central peak at $\omega = 0$ associated with the long-range charge order. This peak grows strongly with λ and introduces strong fluctuations in the dynamic displacement correlation function (2.27) at all momenta q. The fluctuations cause a significant broadening of the spectrum obtained by analytic continuation, and in particular make it virtually impossible to resolve finite-frequency contributions at $q = \pi$, cf. Fig. 4.14(c).

To follow the phonon dispersion in the ordered phase, we instead consider the spectral function $B_P(q,\omega)$ shown in Figs. 4.14(d)–(f). The use of the momentum correlation function (2.28) filters out the central mode, and allows us to unambiguously identify the hardening of the phonon dispersion at $q = \pi$ in the Peierls phase [Fig. 4.14(f)]. Hence, the Peierls transition in the adiabatic regime can be classified as a soft-mode transition. Further evidence for the soft-mode behavior comes from a minimum in the phonon kinetic energy that appears in the vicinity of λ_c (for details see our discussion of sum rules in App. B.3.2 and the results in Ref. [P3]).

The phonon spectral functions $B_Q(q,\omega)$ and $B_P(q,\omega)$ are directly related to the charge structure factor $S_\rho(q,\omega)$ by an exact mapping that is given in App. B.2. Therefore, the renormalization of the phonon dispersion is also contained in $S_\rho(q,\omega)$ [71]. However, the study of the phonon hardening from $S_\rho(q,\omega)$ is more elaborate than from $B(q,\omega)$ because in addition to the central peak at $\omega = 0$ in the Peierls phase, also the particle-hole continuum has substantial spectral weight. On the other hand, the particle-hole continuum also enters the phonon spectra, but its high-energy contributions are filtered out. Nonetheless, the phonon spectral functions must contain gapless excitations at $q = \pi$ throughout the metallic phase that are related to particle-hole excitations.[6] The mixing of particle-hole and phonon excitations leads to another feature at small momenta q where the phonon dispersion in Figs. 4.14(a) and 4.14(d) seems to be discontinuous. In Ref. [P5] this feature is explained as a hybridization effect between coherent particle-hole and phonon excitations. For an unambiguous identification of this feature, large lattice sizes are required. The hybridization feature at small momenta vanishes in the Peierls phase, as can be seen in Figs. 4.14(c) and 4.14(f). For a detailed discussion of the phonon spectral function and its relations to charge excitations see Ref. [P5].

4.2.3. Specific heat in the adiabatic regime

Figure 4.15(a) shows the evolution of the specific heat from weak to strong electron-phonon coupling λ at an intermediate phonon frequency $\omega_0/t = 0.4$. The parameters chosen in Fig. 4.15(a) are very similar to those in Fig. 4.2(a) in the adiabatic limit. For temperatures $k_\mathrm{B}T \gg \omega_0$, we expect the adiabatic approximation to be valid and indeed we find that the high-temperature fermionic peak at $k_\mathrm{B}T = \mathcal{O}(t)$ is suppressed by the electron-phonon interaction, exactly as for $\omega_0 = 0$. However, quantum lattice fluctuations lead to a very different behavior at $k_\mathrm{B}T \lesssim \omega_0$. Most notably, $C_V \to 0$ for $T \to 0$ as

[6] Note that for finite lattice sizes, $S_\rho(q,\omega)$ has a finite-size gap at $q = \pi$. For a discussion of finite-size effects see Ref. [P5].

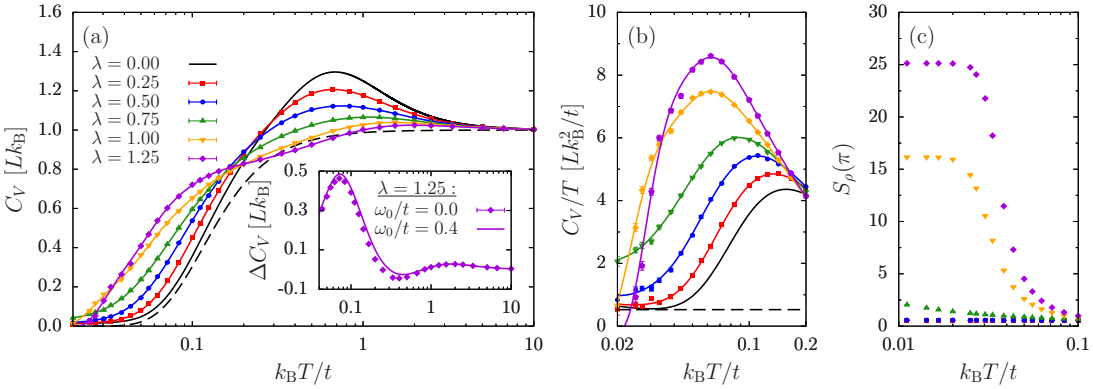

Figure 4.15.: (a) Specific heat of the spinless Holstein model in the adiabatic regime. Data points correspond to direct estimates of C_V, whereas straight lines are obtained from fits to the total energy using the maximum entropy method (for details see App. C). The dashed line corresponds to the free-phonon contribution. The inset shows C_V subtracted by the free-phonon contribution for $\lambda = 1.25$ and compares it to the adiabatic approximation. (b) C_V/T for the same data. (c) Charge structure factor at the ordering vector $q = \pi$. Here, $\omega_0/t = 0.4$ and $L = 162$. Results were obtained using the SSE representation.

expected from the third law of thermodynamics. Moreover, at $\omega_0/t = 0.4$ the ground state is metallic for $\lambda < \lambda_c = 0.68(1)$ and a Peierls insulator for $\lambda > \lambda_c$. At low temperatures, C_V is therefore expected to exhibit a linear fermionic contribution in the metallic phase, and an exponential contribution due to the Peierls gap in the insulating phase. Figure 4.15(a) shows that in the temperature interval $0.05 < k_BT/t < 0.1$ C_V is enhanced with increasing λ up to the strongest coupling considered, whereas for $k_BT/t < 0.05$ C_V is suppressed between $\lambda = 1.0$ and $\lambda = 1.25$ in the Peierls phase. In the following, we explain the low-temperature behavior of the specific heat using the predictions of Luttinger liquid theory, our previous results for the adiabatic limit, and our knowledge of the spectral features of $A(k,\omega)$ and $B(q,\omega)$.

The metallic phase that exists for $\lambda < \lambda_c$ as a result of quantum lattice fluctuations has been identified as a repulsive Luttinger liquid with $K < 1$ [29,32]. Consequently, the fermionic contribution to the specific heat should be given by [184]

$$C_V^{\mathrm{el}} = \frac{\pi}{3}\frac{Lk_B^2T}{u}\,, \tag{4.24}$$

with the renormalized charge velocity u. For the present case, $u \to v_F = 2t$ for either $\lambda \to 0$ or $\omega_0 \to \infty$. Equation (4.24) holds for an infinitely wide band, whereas a finite band width gives rise to the high-temperature peak discussed in Sec. 4.1.3. The linear contribution (4.24) will hence only be observable at low temperatures. To test the specific heat for this contribution, Fig. 4.15(b) shows C_V/T in the low-temperature regime. Already for the noninteracting case $\lambda = 0$, it is difficult to detect the constant electronic contribution to C_V/T defined by Eq. (4.24) with $u = v_F$ (dashed line). As temperature is decreased, our result at $\lambda = 0$ first converges to this constant, but below

$k_\mathrm{B}T/t \approx 0.03$ it starts to deviate. The latter is a result of the finite lattice size $L = 162$. When we increase the electron-phonon coupling up to $\lambda = 0.75$, the absolute value of C_V/T becomes larger in the entire temperature range shown in Fig. 4.15(b). From the maximum entropy fits to the total energy (straight lines) we conclude that the charge velocity is reduced with increasing λ. However, we cannot unambiguously determine u from the QMC data because C_V/T does not yet reach a plateau for the temperatures considered and at $L = 162$. Note that at $\lambda = 0.75$, the system is already in the Peierls phase, but the gap is exponentially small and cannot be detected in Fig. 4.15(b). Deep in the Peierls phase, i.e., at $\lambda = 1.0$ and $\lambda = 1.25$, C_V/T drops down to zero for $T \to 0$, as expected for a gapped system.

In the adiabatic limit, the appearance of a low-temperature peak in C_V signalled the onset of enhanced CDW correlations as temperature was decreased (see the discussion in Sec. 4.1.3). We found the same behavior for small but finite ω_0 (see Fig. 4.12) as long as the system was deep enough in the Peierls phase. For $\omega_0/t = 0.4$, the free-phonon contribution indicated by a dashed line in Fig. 4.15(a) as well as the phonon renormalization across the Peierls transition make it difficult to detect a clear signature of the Peierls ordering in the specific heat. Therefore, Fig. 4.15(c) shows the charge structure factor $S_\rho(\pi)$ at the ordering vector $q = 2k_\mathrm{F} = \pi$ as a function of temperature. In the metallic phase, $S_\rho(\pi)$ does not show any signature of CDW ordering, but already at $\lambda = 0.75$, close to the critical coupling $\lambda_c = 0.68(1)$, $S_\rho(\pi)$ slowly increases with decreasing temperature. However, the temperature scale where $S_\rho(\pi)$ starts to increase is too small to detect any signature of enhanced CDW correlations in our C_V data shown in Fig. 4.15(a). Deeper in the Peierls phase, $S_\rho(\pi)$ is strongly enhanced at temperatures $k_\mathrm{B}T/t < 0.1$ and reaches a plateau at even lower temperatures, very similar to our results in the adiabatic limit. The onset of dominant CDW correlations in $S_\rho(\pi)$ suggests that we find a related signature in C_V. Indeed, for the strongest coupling considered, i.e., $\lambda = 1.25$, and for $k_\mathrm{B}T/t \lesssim 0.1$, we find that the difference ΔC_V between C_V and the free-phonon contribution closely follows the result in the adiabatic approximation, as shown in the inset of Fig. 4.15(a). In particular, ΔC_V only shows small deviations between $\omega_0/t = 0.4$ and $\omega_0 = 0$ at intermediate temperatures.

Finally, the specific heat is also related to the single-particle spectral functions $A(k,\omega)$ and $B(q,\omega)$ via the sum rules given in App. B.1. In the metallic phase, the increase of C_V as a function of λ that appears in the entire low-temperature regime can be attributed to three effects: (i) the reduction of the charge velocity u, as apparent from the renormalization of $A(k,\omega)$ around the Fermi level in Fig. 4.13(a); (ii) the phonon softening towards the Peierls transition shown in Fig. 4.14; and (iii) the formation of a second band in $A(k,\omega)$ that originates from the phonon satellites at $k = k_\mathrm{F}$ and $\omega = \pm\omega_0$ and merges into the cosine band away from k_F, as discussed in Sec. 4.2.2. In the Peierls phase, the hardening of the phonon dispersion as well as the opening of the Peierls gap in the low-energy bands of $A(k,\omega)$, cf. Fig. 4.13(b), lead to a suppression of C_V at very low temperatures for $\lambda \gtrsim 1.0$. However, C_V further increases around $k_\mathrm{B}T/t \approx 0.1$ which is very similar to the adiabatic limit shown in Fig. 4.2(a), where the low-temperature peak appears. For $\omega_0 = 0$, we have mainly attributed this contribution to the formation of the mean-field gap as temperature is decreased. The comparison of C_V for $\omega_0/t = 0.4$

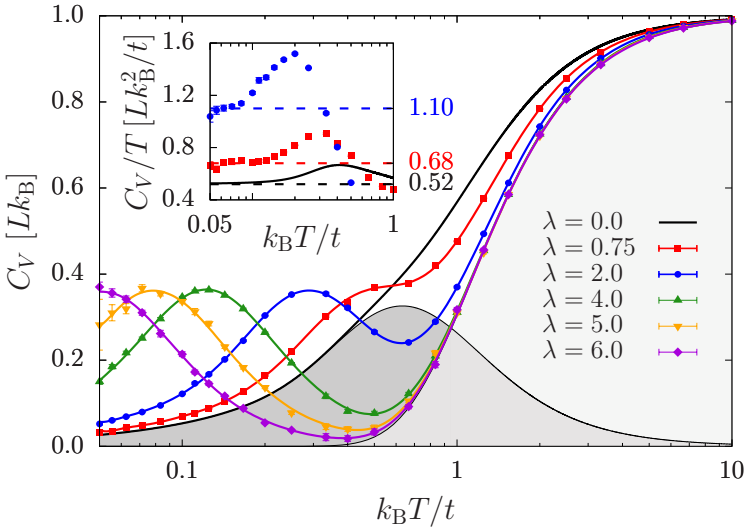

Figure 4.16.: Specific heat of the spinless Holstein model in the antiadiabatic regime. Data points correspond to direct estimates of C_V, whereas straight lines are obtained from fits to the total energy using the maximum entropy method (for details see App. C). The shaded areas indicate the free-electron and free-phonon contributions. The inset shows C_V/T for weak couplings. The dashed lines correspond to fits to the total energy of the form $E(T) = E_0 + \frac{1}{2}aT^2$. Here, $\omega_0/t = 4$ and $L = 162$. Results were obtained using the SSE representation.

and $\omega_0 = 0$ in the inset of Fig. 4.15(a) reveals that the formation of the mean-field bands may be the dominant contribution to C_V at strong coupling.

4.2.4. Specific heat in the antiadiabatic regime

In the antiadiabatic regime, the formation of the Peierls state is conceptually different from the adiabatic regime discussed before. Here, the electrons first undergo a crossover to small polarons with an effective mass that is significantly increased. In a second step, the polarons order and form a polaronic superlattice [27]. In this section, we study the formation of small polarons in the metallic phase from a thermodynamic perspective.

Figure 4.16 shows C_V at $\omega_0/t = 4$ for different electron-phonon couplings λ. At $\lambda = 0$, C_V is the sum of the free-electron and free-phonon contributions indicated by the shaded areas in Fig. 4.16. As λ is increased, the high-temperature part of C_V converges to the free-phonon contribution, whereas the free-electron part is mainly shifted to lower temperatures. Thereby, the charge velocity u characteristic for the Luttinger liquid regime is significantly reduced, as confirmed for small couplings λ in the inset of Fig. 4.16. In contrast to the adiabatic regime, C_V/T unambiguously reaches a constant at low temperatures that increases with increasing λ. From fitting the total energy to the form $E(T) = E_0 + \frac{1}{2}aT^2$ for temperatures $\beta t \in [10, 20]$ and using Eq. (4.24), we obtain estimates for the renormalized charge velocities. For example, at $\lambda = 2$ we get $u \approx 0.47\, v_F$.

The shift of the electronic contribution to C_V towards lower temperatures as well as the reduction of the charge velocity with increasing λ can be related to the electronic spectral function $A(k,\omega)$. As a result of small polaron formation, the band width of the electronic dispersion in $A(k,\omega)$ shrinks with increasing λ as observed numerically in Refs. [27, 185]. The effective mass of the polarons increases and the resulting dispersion can—as a first approximation—be modeled by an effective hopping $\tilde{t} = u/2$. On the one hand, $\tilde{t}$ can be estimated by extracting u from the low-temperature behavior of C_V as shown in the inset of Fig. 4.16. On the other hand, the position of the peak in the electronic contribution of C_V should give a good estimate for $\tilde{t}$. At $\lambda = 0$, the peak position is related to the coherence scale of free fermions, $k_\mathrm{B}T/t \approx 0.63$, whereas at $\lambda = 2$ we have $k_\mathrm{B}T/t \approx 0.29$ which reproduces our estimate of $u \approx 0.47\, v_\mathrm{F}$ very well. Note that the renormalization of the effective hopping for a single polaron can also be estimated using the Lang-Firsov transformation and approximately calculating the polaron ground state from the zero-phonon sector [186]. However, the resulting $\tilde{t} = \exp(-\lambda W/2\omega_0)$ overestimates the renormalization of the charge velocity. Here, $W = 4t$ is the band width of the electronic dispersion at $\lambda = 0$. The suppression of the charge velocity is in accordance with previous estimates of the Luttinger liquid parameters from bosonization [187] and QMC simulations [25, 26].

In contrast to the adiabatic regime, the influence of the phonon spectral function $B(q,\omega)$ on C_V seems to be limited. A finite electron-phonon interaction leads to a hardening of the phonon dispersion at $q = \pi$ as well as the appearance of the electronic particle-hole continuum in $B(q,\omega)$ [27, 185]. The latter is a consequence of the exact relation between $B(q,\omega)$ and the dynamic charge structure factor (see App. B.2). However, with increasing electron-phonon coupling the high-temperature part of C_V only approaches the free-phonon contribution.

5. Conclusions and outlook

Thus far, the efficient simulation of fermion-boson models has posed a difficult problem for numerical methods. While DMRG studies were hindered by the unbound bosonic Hilbert space, QMC methods often suffered from large autocorrelation times as a consequence of local boson updates. These difficulties in simulating fermion-boson models were summarized in Chap. 1. In this thesis, we worked on a QMC approach that aims to overcome these issues by simulating the fermion-boson problem in the form of a retarded fermionic interaction. Our starting point was the CT-INT method that had been successfully applied to the simulation of fermion-boson models [67, 70, 71]. In the course of this work, we extended the action-based QMC formalism to the measurement of bosonic observables, developed an efficient directed-loop QMC algorithm, and provided a comprehensive study of the thermodynamic properties of Peierls chains.

The primary goal of this thesis was the further development of the action-based QMC approach to simulate fermion-boson lattice models. As a first step, we introduced the path-integral formalism for a generic fermion-boson model in Chap. 2. By integrating out the bosonic degrees of freedom, we derived a retarded fermionic interaction that is mediated by the free boson propagator. Using the concept of generating functionals, we showed that bosonic observables can be recovered from fermionic correlation functions. In particular, we derived sum rules for the phonon propagator and the total energy of the Holstein model. The action-based QMC approach to retarded interactions was discussed in Chap. 3 using the example of the Holstein model. Starting from a unified picture of QMC methods based on a perturbation expansion, we outlined three representations to treat retarded interactions: the diagrammatic determinantal representation used in the CT-INT method, the world-line representation used for the worm algorithm, and the SSE representation used for the directed-loop algorithm. For convenience, we introduced these methods in their original formulation and then showed how they apply to retarded interactions. While the CT-INT method had already been used to simulate retarded interactions [70, 71], the worm algorithm has only recently been applied to systems coupled to a bosonic bath [72]. The directed-loop algorithm for retarded interactions is one of the key achievements of this work [P2]. In the overview section, we only discussed the basic ideas that allow an efficient treatment of retarded interactions in the SSE representation. The development of the directed-loop algorithm was closely related to our second algorithmic achievement, i.e., the derivation of bosonic estimators that exploit the information provided by the interaction vertices. This technique is frequently used in world-line or SSE representations. Inspired by the work of Wang *et al.* [81], who derived a universal estimator for the fidelity susceptibility applicable to many different QMC methods, we generalized their estimator to the case of boson-mediated retarded interactions [P3]. Furthermore, we used the same techniques to estimate the phonon

propagator and the total energy of the Holstein model from the Monte Carlo configurations. We tested our new estimators for the CT-INT method and compared our results to measurements from Wick's theorem. The analogy between the different QMC methods led us to the development of the directed-loop algorithm for retarded interactions. At the end of Chap. 3, we provided a detailed description of the directed-loop algorithm using the example of the spinful Holstein model. We derived the Monte Carlo weights, discussed the diagonal and directed-loop updates, and defined efficient estimators based on the distribution of vertices. In particular, we derived a direct estimator for the specific heat. Applications to the Holstein model showed that autocorrelation times are negligibly small for the entire parameter range, even in the vicinity of the phase transition. For the spinless Holstein model, we estimated the critical coupling $\lambda_c = 0.68(1)$ for a fixed phonon frequency $\omega_0/t = 0.4$ from the real-space correlation functions and a cusp in the fidelity susceptibility. In the end, we discussed possible extensions of the directed-loop algorithm to other models of particles or spins coupled to a bosonic bath.

The second part of this thesis dealt with the thermodynamic and spectral properties of Peierls chains and was presented in Chap. 4. Based on our algorithmic developments we provided a comprehensive study of the specific heat across the entire phase diagram of a 1D Peierls system. We first considered the adiabatic limit of the spinless Holstein and SSH models. Here, a dimerized Peierls state exists for any nonzero electron-phonon coupling at zero temperature, as described by mean-field theory. Using a classical Monte Carlo method, we studied the effects of thermal fluctuations on the specific heat, the electronic single-particle spectrum, the dynamic charge and bond structure factors, and the optical conductivity [P4]. In the adiabatic limit, we were able to calculate exact spectral functions for different temperatures without using analytic continuation. We found that thermal fluctuations destroy long-range order at finite temperatures and give rise to a low-temperature peak in the specific heat. A comparison to the electronic single-particle spectral function revealed that this peak is related to the temperature scale where the Peierls gap is filled in by thermal fluctuations. In particular, thermally-excited solitons manifest themselves as in-gap excitations. In the Holstein model, they appear symmetrically around the Fermi level, whereas in the SSH model they are pinned to zero energy and protected by chiral symmetry. The filling of the Peierls gap is also reflected in the two-particle spectra and in the optical conductivity. Moreover, high-temperature features in the spectral functions were related to disorder models. Having investigated the effects of thermal fluctuations on the Peierls state, we also considered the combined effects of thermal and quantum lattice fluctuations. The latter destroy the ordered phase at a critical value of the phonon frequency and lead to a metallic Tomonaga-Luttinger liquid phase. We studied the specific heat of the spinless Holstein model covering the entire parameter range from low to high phonon frequencies ω_0 and from weak to strong electron-phonon coupling λ. We verified that the adiabatic approximation is accurate for $k_\mathrm{B}T \gtrsim \omega_0$ and deep in the Peierls phase. Studying the effect of quantum lattice fluctuations as a function of ω_0, we found that the low-temperature peak in the specific heat remains for small but finite phonon frequencies and only disappears in the vicinity of the Peierls transition. In the low-temperature regime of the metallic phase, bosonization predicts a linear dependence of the specific heat on temperature with a

prefactor that is inversely proportional to the charge velocity. We found evidence for $C_V \sim T$ in the adiabatic regime, but unambiguous verification was only possible in the antiadiabatic regime of high phonon frequencies. In both regimes, electron-phonon interaction leads to a reduction of the charge velocity that is particularly strong in the antiadiabatic regime. At high phonon frequencies and as a function of λ, we found that the electronic contribution to C_V is shifted towards lower temperatures, whereas the phonon contribution hardly changes. The shift of the electronic feature is a consequence of small polaron formation with a significantly increased effective mass. In the adiabatic regime, the evolution of C_V as a function of λ was found to be very different and was explained with the help of the single-particle spectral functions of electrons and phonons. We discussed three relevant effects: (i) the renormalization of the charge velocity in the metallic phase and the subsequent splitting of the polaron bands in the Peierls phase, (ii) the additional formation of the mean-field bands including the shadow bands, and (iii) the softening of the phonon dispersion at the Brillouin zone boundary towards the Peierls transition as well as the subsequent hardening in the Peierls phase. As a result, C_V monotonically increases with λ in the temperature interval $0.05 < k_\mathrm{B}T/t < 0.1$ (here $\omega_0/t = 0.4$). This trend continues in the Peierls phase, where C_V is only suppressed at even lower temperatures $k_\mathrm{B}T/t < 0.05$. Deep in the Peierls phase, we found that C_V is again well described by the adiabatic approximation.

The calculation of the specific heat for the spinless Holstein model combined all the algorithmic developments of this thesis. On the one hand, it was the first application of our directed-loop algorithm for retarded interactions. The efficiency of the method made it possible to simulate temperatures and system sizes that could not be reached with the CT-INT method. Therefore, finite-size effects were under control for all our results. On the other hand, we used generating functionals and the information provided by the vertex distribution to derive a QMC estimator for C_V, a complicated observable that is a combination of fermionic and bosonic operators. However, spectral functions have only been calculated from the CT-INT method on much smaller system sizes. As a future project, we consider the calculation of dynamical correlation functions from the directed-loop algorithm to reach larger system sizes and lower temperatures. For example, the electronic single-particle Green's function can be obtained during the construction of the loop [188, 189], whereas the phonon propagator of the Holstein model can be accessed from the world-line configurations. For the latter, it would also be interesting to implement the retarded interaction with additional Ising fields from which we calculated the phonon propagator using the CT-INT method.

In 1D, the directed-loop algorithm for retarded interactions can be applied to the same class of fermion-boson models as the CT-INT method. Therefore, many previous studies can be extended to much larger system sizes. We showed that the basic idea behind our algorithm carries over to various models, for example, a Fröhlich model with a nonlocal diagonal interaction in space and imaginary time or the optical SSH model with a retarded interaction between off-diagonal bond operators. Instantaneous interactions like the Hubbard interaction can also be added. The subvertex structure introduced for retarded interactions can even be applied to certain nonlocal interactions at equal times. Furthermore, open quantum systems in equilibrium coupled to a bosonic bath can be

simulated by replacing the phonon propagator in the retarded interaction [72]. The directed-loop algorithm is not restricted to fermionic models. If we replace the fermionic operators by hard-core bosons, the method can be applied to similar bosonic models, even in higher dimensions. Additionally, the simulation of spin-boson models may have great potential.

There are some restrictions on the scope of the directed-loop algorithm. Similar to the CT-INT method, the SSH model with acoustic phonons will generate a sign problem because the nonlocal phonon propagator has negative contributions [P6]. Moreover, our method is based on a world-line representation. Therefore, fermion-boson models in more than one dimension will generate a severe sign problem as well. For the latter case, the CT-INT method may be an appropriate alternative and has recently been applied to the 2D Holstein model [P1]. For simulations with the CT-INT method, our developments on measuring bosonic observables from the vertex distribution are relevant. We have already applied our estimator for the fidelity susceptibility to the 2D Holstein model [P1]. Future applications may include the phonon propagator. Moreover, our SSE estimator for the specific heat directly transfers to the CT-INT method and may be used to study finite-temperature phase transitions in 2D.

Finally, the thermodynamic properties of Peierls chains may be further investigated by adding an interchain coupling to address the dimensional crossover to three dimensions. To circumvent the fermionic sign problem, a study of spin-Peierls models is favorable. This application has the potential to study the experimentally observed low-temperature peak in C_V using exact simulations.

A. Interaction picture and retardation

In this work, we used the coherent-state path-integral formulation of the partition function. This is a natural choice for fermion-boson models because the Gaussian integrals over the bosonic fields can be calculated exactly. This leads to a retarded fermionic action that can be simulated with the action-based CT-INT method discussed in Sec. 3.2.2. Moreover, the concept of generating functionals provides an easy formalism to derive sum rules for bosonic observables. In this way, the latter can be calculated only from the knowledge of fermionic correlation functions. However, world-line QMC methods like the worm algorithm or the directed-loop algorithm are usually based on a Hamiltonian formulation. We have shown in Sec. 3.2 that these methods can be recovered from the action-based formulation by mapping expectation values of Grassmann variables to time-ordered products of operators. In the following, we show how retarded interactions can be obtained from the interaction picture without referring to the path integral.

In the interaction picture, the Hamiltonian $\hat{H} = \hat{H}_0 + \hat{V}$ is usually split into the unperturbed part $\hat{H}_0$ and the perturbation $\hat{V}$. The partition function can be written as

$$Z = \mathrm{Tr}\left[e^{-\beta \hat{H}_0} \mathcal{T}_\tau \, e^{-\int_0^\beta d\tau \, \hat{V}(\tau)} \right] = Z_0 \left\langle \mathcal{T}_\tau \, e^{-\int_0^\beta d\tau \, \hat{V}(\tau)} \right\rangle_0 , \tag{A.1}$$

where the time evolution of the perturbation $\hat{V}(\tau) = e^{\tau \hat{H}_0} \hat{V} e^{-\tau \hat{H}_0}$ is performed according to the unperturbed part of the Hamiltonian. Here, we introduced the time-ordering operator $\mathcal{T}_\tau$ and we defined $\langle \hat{O} \rangle_0 = Z^{-1} \mathrm{Tr}\, e^{-\beta \hat{H}_0} \hat{O}$ with $Z = \mathrm{Tr}\, e^{-\beta \hat{H}_0}$. The Dyson expansion of Eq. (A.1) becomes

$$\frac{Z}{Z_0} = \sum_{n=0}^{\infty} \frac{(-1)^n}{n!} \int_0^\beta d\tau_1 \cdots \int_0^\beta d\tau_n \left\langle \mathcal{T}_\tau \, \hat{V}(\tau_1) \dots \hat{V}(\tau_n) \right\rangle_0 . \tag{A.2}$$

The expansion in Eq. (A.2) is the starting point to formulate the worm algorithm as reviewed in Sec. 3.2.3 [53]. Moreover, also the SSE representation discussed in Sec. 3.2.4 follows from the interaction picture by choosing $\hat{H}_0 = 0$ [91].

Consider the generic fermion-boson model (2.1). We choose $\hat{H}_0 = \hat{H}_\mathrm{f} + \hat{H}_\mathrm{b}$ and $\hat{V} = \hat{H}_\mathrm{fb}$. To simplify the notation in the following, we write $\hat{V} = \sum_{q,a} V_q^a = \sum_{q,a} \gamma_q^a \hat{\varrho}_q^a \hat{b}_q^a$, where the superscript a is, i.a., used to distinguish between bosonic creation and annihilation operators, i.e., $V_q^1 = \gamma_q \hat{\varrho}_q \hat{b}_q^\dagger$ and $V_q^2 = \bar{\gamma}_q \hat{\varrho}_q^\dagger \hat{b}_q$. The interaction expansion becomes

$$\begin{aligned} \frac{Z}{Z_0} = \sum_{n=0}^{\infty} \frac{(-1)^n}{n!} \int_0^\beta d\tau_1 \, \dots \int_0^\beta d\tau_n \sum_{q_1 \dots q_n} \sum_{a_1 \dots a_n} \gamma_{q_1}^{a_1} \dots \gamma_{q_n}^{a_n} \\ \times \left\langle \mathcal{T}_\tau \, \hat{\varrho}_{q_1}^{a_1}(\tau_1) \dots \hat{\varrho}_{q_n}^{a_n}(\tau_n) \right\rangle_\mathrm{f} \left\langle \mathcal{T}_\tau \, \hat{b}_{q_1}^{a_1}(\tau_1) \dots \hat{b}_{q_n}^{a_n}(\tau_n) \right\rangle_\mathrm{b} . \end{aligned} \tag{A.3}$$

Here, $\langle \ldots \rangle_0$ splits into separate expectation values for fermions and bosons.[1] Due to particle-number conservation, $\left\langle \mathcal{T}_\tau \, \hat{b}^{a_1}_{q_1}(\tau_1) \ldots \hat{b}^{a_n}_{q_n}(\tau_n) \right\rangle_\mathrm{b}$ only gives a nonzero contribution if $n = 2m$ and the number of creation and annihilation operators is the same. The bosonic expectation value can be further simplified using Wick's theorem. For example, consider the bosonic correlation function with operators ordered as follows:

$$\left\langle \mathcal{T}_\tau \, \hat{b}^\dagger_{q_1}(\tau_1) \ldots \hat{b}^\dagger_{q_m}(\tau_m) \, \hat{b}_{q_{m+1}}(\tau_{m+1}) \ldots \hat{b}_{q_{2m}}(\tau_{2m}) \right\rangle_\mathrm{b} = \sum_{\pi \in \mathcal{S}_m} \prod_{k=1}^{m} \omega_{q_k}^{-1} \, P_{q_k}(\tau_k - \tau_{m+\pi[k]}) \, \delta_{q_k, q_{m+\pi[k]}} \, . \tag{A.4}$$

Here, $\mathcal{S}_m$ is the symmetric group of order m and $\pi \in \mathcal{S}_m$ is a permutation of m objects. We introduced the free boson propagator P_q and the boson frequency ω_q defined in Sec. 2.2. The l.h.s. of Eq. (A.4) represents only one possible combination of choosing $\{a_1, \ldots, a_n\}$ such that we obtain the same number of creation and annihilation operators. In total, there are $\binom{2m}{m}$ combinations. Inserting Eq. (A.4) into the perturbation expansion (A.3), we obtain (we define $\tau'_k = \tau_{m+k}$)

$$\begin{aligned} \frac{Z}{Z_0} = \sum_{m=0}^{\infty} \frac{1}{(2m)!} \binom{2m}{m} \iint_0^\beta d\tau_1 \, d\tau'_1 \, \ldots \iint_0^\beta d\tau_m \, d\tau'_m \sum_{q_1 \ldots q_m} \frac{|\gamma_{q_1}|^2}{\omega_{q_1}} \ldots \frac{|\gamma_{q_m}|^2}{\omega_{q_m}} \sum_{\pi \in \mathcal{S}_m} \\ \times P_{q_1}(\tau_1 - \tau'_{\pi[1]}) \ldots P_{q_m}(\tau_m - \tau'_{\pi[m]}) \left\langle \mathcal{T}_\tau \, \hat{\varrho}_{q_1}(\tau_1) \, \hat{\varrho}^\dagger_{q_1}(\tau'_{\pi[1]}) \ldots \hat{\varrho}_{q_m}(\tau_m) \, \hat{\varrho}^\dagger_{q_m}(\tau'_{\pi[m]}) \right\rangle_\mathrm{f} . \end{aligned} \tag{A.5}$$

The sum over all permutations can be evaluated by relabeling the variables, which gives another factor of $m!$ in Eq. (A.5). The perturbation expansion finally becomes

$$\begin{aligned} \frac{Z}{Z_0} = \sum_{m=0}^{\infty} \frac{1}{m!} \iint_0^\beta d\tau_1 \, d\tau'_1 \sum_{q_1} \frac{|\gamma_{q_1}|^2}{\omega_{q_1}} P_{q_1}(\tau_1 - \tau'_1) \, \ldots \iint_0^\beta d\tau_m \, d\tau'_m \frac{|\gamma_{q_m}|^2}{\omega_{q_m}} P_{q_m}(\tau_m - \tau'_m) \\ \times \left\langle \mathcal{T}_\tau \, \hat{\varrho}_{q_1}(\tau_1) \, \hat{\varrho}^\dagger_{q_1}(\tau'_1) \ldots \hat{\varrho}_{q_m}(\tau_m) \, \hat{\varrho}^\dagger_{q_m}(\tau'_m) \right\rangle_\mathrm{f} \end{aligned} \tag{A.6}$$

and can be rewritten in an exponential form again, i.e.,

$$\frac{Z}{Z_0} = \left\langle \mathcal{T}_\tau \, \exp\left[\iint_0^\beta d\tau \, d\tau' \sum_q \frac{|\gamma_q|^2}{\omega_q} \hat{\varrho}_q(\tau) \, P_q(\tau - \tau') \, \hat{\varrho}^\dagger_q(\tau') \right] \right\rangle_0 . \tag{A.7}$$

The exponent in Eq. (A.7) has the same form as the retarded interaction (2.12) derived from the path-integral approach, only the Grassmann fields are replaced by operators. This derivation shows that one does not need an action-based formulation to obtain retarded interactions. Sum rules for the bosonic operators can also be derived from the equations of motion instead of using generating functionals [88].

[1] Now the imaginary-time evolution of fermionic (bosonic) operators is with respect to $\hat{H}_\mathrm{f}$ ($\hat{H}_\mathrm{b}$).

B. Spectral functions and sum rules

Spectral functions are very important for our understanding of quantum many-particle systems because they give direct access to the momentum- and frequency-resolved excitations of a system. In the following, we define the spectral functions for the spinless Holstein model and discuss the problem of numerical analytic continuation. Furthermore, we derive exact relations between the phonon spectral function and the charge structure factor and discuss the implications for the spectra. Finally, we specify relations between the total energy and the spectral functions of the Holstein model.

B.1. Spectral functions and analytic continuation

Spectral functions are usually defined from a Lehmann representation and give direct access to real frequencies ω. For the fermionic single-particle spectrum, we have

$$A(k,\omega) = \frac{1}{Z}\sum_{mn} e^{-\beta E_m}\left(1+e^{-\beta\omega}\right)\left|\langle m|\,\hat{c}_k\,|n\rangle\right|^2 \delta[\omega-(E_n-E_m)]\,, \tag{B.1}$$

whereas the bosonic single-particle spectrum is defined as

$$B(q,\omega) = \frac{1}{Z}\sum_{mn} e^{-\beta E_m}\left(1-e^{-\beta\omega}\right)\left|\langle m|\,\hat{b}_q\,|n\rangle\right|^2 \delta[\omega-(E_n-E_m)]\,. \tag{B.2}$$

Here, $\hat{c}_k$ is the fermionic annihilation operator at momentum k and $\hat{b}_q$ is the bosonic annihilation operator with momentum transfer q. Furthermore, $|m\rangle$ is a many-particle eigenstate of the Hamiltonian and E_m the corresponding energy eigenvalue. Note that the chemical potential is included in the Hamiltonian and therefore also in E_m. In the same way, we define the charge structure factor

$$S_\rho(q,\omega) = \frac{1}{Z}\sum_{mn} e^{-\beta E_m}\left|\langle m|\,\hat{\rho}_q\,|n\rangle\right|^2 \delta[\omega-(E_n-E_m)]\,, \tag{B.3}$$

where $\hat{\rho}_q$ creates a charge excitation with momentum transfer q.

For fermion-boson models defined in first quantization, it is useful to split $B(q,\omega)$ into its momentum and displacement contributions. For the Holstein model, we have

$$B_Q(q,\omega) = \frac{K}{Z}\sum_{mn} e^{-\beta E_m}\left|\langle m|\,\hat{Q}_q\,|n\rangle\right|^2 \delta[\omega-(E_n-E_m)]\,, \tag{B.4}$$

$$B_P(q,\omega) = \frac{1}{MZ}\sum_{mn} e^{-\beta E_m}\left|\langle m|\,\hat{P}_q\,|n\rangle\right|^2 \delta[\omega-(E_n-E_m)]\,, \tag{B.5}$$

where $\hat{Q}_q$ and $\hat{P}_q$ are the bosonic displacement and momentum operators, respectively. We included the stiffness constant K and the mass M in the spectral functions to be consistent with the definitions of the phonon propagators in Eqs. (2.27) and (2.28). In contrast to the definition of $B(q,\omega)$, we omitted the factor $(1-e^{-\beta\omega})$ because it is problematic for the numerical analytic continuation of imaginary-time correlation functions. $B_Q(q,\omega)$ and $B_P(q,\omega)$ have the same form as $S_\rho(q,\omega)$ and should therefore be regarded as structure factors. To include the additional factor in the spectral functions, we define $\bar{B}_Q(q,\omega) = (1-e^{-\beta\omega})\, B_Q(q,\omega)$ and $\bar{B}_P(q,\omega) = (1-e^{-\beta\omega})\, B_P(q,\omega)$. In the same way, we define $\bar{S}_\rho(q,\omega) = (1-e^{-\beta\omega})\, S_\rho(q,\omega)$ for the charge structure factor.

QMC methods do not provide direct access to spectral functions. They only give access to dynamical correlation functions in imaginary time. However, these correlation functions are related to spectral functions via sum rules. For example, we have

$$G(k,\tau) = \int_{-\infty}^{\infty} d\omega\, \frac{e^{-\tau\omega}}{1+e^{-\beta\omega}}\, A(k,\omega) \tag{B.6}$$

for the electronic single-particle Green's function as well as

$$C_\rho(q,\tau) = \int_0^{\infty} d\omega \left[e^{-\tau\omega} + e^{-(\beta-\tau)\omega}\right] S_\rho(q,\omega) \tag{B.7}$$

for the dynamical charge-charge correlation function. Equivalent relations are obtained by replacing $C_\rho(q,\tau)$ in Eq. (B.7) with the phonon propagator $D_Q(q,\tau)$ $[D_P(q,\tau)]$ and $S_\rho(q,\omega)$ with the phonon spectral function $B_Q(q,\omega)$ $[B_P(q,\omega)]$. Analytic continuation considers the inversion of these integral equations to obtain the spectral functions $A(k,\omega)$ or $S_\rho(q,\omega)$ on the real-frequency axis. Mathematically, this problem corresponds to the numerical calculation of a two-sided Laplace transform, which is known to be ill-posed [190]. Moreover, the imaginary-time correlation functions obtained from QMC simulations are only exact within statistical errors. These problems require numerical regularization schemes for the analytic continuation of QMC data. One approach that is often used is the maximum entropy method. In its original formulation, it is based on Bayesian inference (see Ref. [190] for an introduction). To calculate the spectral functions presented in Sec. 4.2.2 of this thesis, we used stochastic analytic continuation [191, 192]. However, we also used the maximum entropy method to fit the total energy and calculate the specific heat [179]. The latter approach is outlined in App. C.2.

B.2. Exact relations between the phonon and charge spectra

For the Holstein model, the phonon spectral function $B(q,\omega)$ and the dynamic charge structure factor $S_\rho(q,\omega)$ in principle contain the same information. Here, starting from the relation (2.27) between the corresponding imaginary-time correlation functions, we derive an exact relation between the spectral functions as well as additional sum rules, and discuss the implications. We only consider $\bar{B}_Q(q,\omega)$, but similar relations can also be derived for $\bar{B}_P(q,\omega)$. To simplify the notation, we include the factor $(1-e^{-\beta\omega})$ in the spectra. Our presentation is based on Ref. [P5].

B.2.1. Analytic properties of the spectral functions

The phonon spectral function $\bar{B}_Q(q,\omega)$ can be obtained from the Lehmann representation of the phonon propagator

$$D_Q(q,z) = -\int_{-\infty}^{\infty} d\omega \; \frac{\bar{B}_Q(q,\omega)}{z-\omega} \tag{B.8}$$

by analyzing its pole structure in the complex-frequency plane. For simplicity, we restrict our considerations to finite Hilbert spaces, where $D(q,z)$ has only simple poles on the real axis[1] determined by the exact relation

$$D_Q(q,z) = P_+(z) + 4\lambda t\, P_+(z)^2\, C_\rho(q,z)\,. \tag{B.9}$$

The term depending on the electron-phonon coupling λ in Eq. (B.9) gives rise to a product of poles arising from the free phonon propagator $P_+(z) = \omega_0^2/(\omega_0^2 - z^2)$ and the charge susceptibility

$$C_\rho(q,z) = \langle \rho_q(z)\rho_{-q}\rangle = -\int_{-\infty}^{\infty} d\omega \; \frac{\bar{S}_\rho(q,\omega)}{z-\omega}\,. \tag{B.10}$$

A partial-fraction decomposition and comparison of the pole structure of the two sides of Eq. (B.9) gives

$$\bar{B}_Q(q,\omega) = \bar{B}_Q^0(q,\omega) + 4\lambda t\, P_+(\omega)^2\, \bar{S}_\rho(q,\omega) + \bar{B}_Q^1(q,\omega)\,. \tag{B.11}$$

For $\lambda = 0$, the phonon spectral function is given by

$$\bar{B}_Q^0(q,\omega) = \frac{\omega_0}{2}\left[\delta(\omega-\omega_0) - \delta(\omega+\omega_0)\right], \tag{B.12}$$

which describes excitations at the bare phonon frequency $\omega = \pm\omega_0$. Any finite electron-phonon coupling leads to the appearance of two additional terms in Eq. (B.11): The first contains the whole charge spectrum $\bar{S}_\rho(q,\omega)$ reweighted by the free phonon propagator, while

$$\bar{B}_Q^1(q,\omega) = -\frac{4\lambda t}{\omega_0}\left[\delta(\omega-\omega_0) - \delta(\omega+\omega_0)\right] \mathcal{P}\int_0^{\infty} d\omega'\, \omega'\, P_+(\omega')^2\, \bar{S}_\rho(q,\omega') \tag{B.13}$$

gives an additional contribution at $\omega = \pm\omega_0$. Here, $\mathcal{P}$ denotes the principal value.

To derive Eq. (B.11), we used a partial-fraction decomposition, leading to poles of both first and second order. However, poles of second order are forbidden by the Lehmann representation (B.8). Therefore, their weights have to vanish, which (for $\omega_0 > 0$) leads

[1] We consider finite lattices with an arbitrary cutoff for the phonons. The same results can be obtained by evaluating $\bar{B}_Q(q,\omega) = \mathrm{Im}[D_Q(q,\omega+\mathrm{i}\eta)]/\pi$ for the general case, where $D_Q(q,z)$ has a branch cut on the real axis.

to the sum rule

$$\mathcal{P}\int_0^\infty d\omega\ \frac{\omega}{\omega^2-\omega_0^2}\ \bar{S}_\rho(q,\omega)=0\,. \tag{B.14}$$

From Eqs. (B.11) and (B.14), we obtain an equivalent sum rule for $\bar{B}_Q(q,\omega)$,

$$\int_0^\infty d\omega\ \omega\left(\omega^2-\omega_0^2\right)\bar{B}_Q(q,\omega)=0\,, \tag{B.15}$$

which is just a combination of the first and third moment of $\bar{B}_Q(q,\omega)$. In the same way, the absence of higher-order poles requires $\bar{S}_\rho(q,\omega=\pm\omega_0)=0$.

For finite electron-phonon coupling, Eq. (B.9) can also be used to obtain the charge spectrum

$$\bar{S}_\rho(q,\omega)=\frac{1}{4\lambda t\,\omega_0^4}\left(\omega^2-\omega_0^2\right)^2\bar{B}_Q(q,\omega) \tag{B.16}$$

from the phonon spectral function. Here, contributions at $\omega=\pm\omega_0$ are removed from $\bar{S}_\rho(q,\omega)$ by the prefactor.

B.2.2. Implications for the spectral properties

In the following, we discuss the implications for the structure factors defined without the factor $(1-e^{-\beta\omega})$. Hence, we use the original symbols $B_Q(q,\omega)$ and $S_\rho(q,\omega)$.

According to Eqs. (B.11) and (B.16), $B_Q(q,\omega)$ and $S_\rho(q,\omega)$ share the same spectral information, up to an additional contribution to $B_Q(q,\pm\omega_0)$ that consists of the free phonon spectrum $B_Q^0(q,\omega)$ and a compensating term $B_Q^1(q,\omega)$ due to finite interactions.

For $q=0$, because of charge conservation, $S_\rho(q,\omega)$ only has a static contribution at $\omega=0$. Thus, $B_Q^1(q=0,\omega)=0$ and the full phonon spectrum is given by the free part at $\omega=\pm\omega_0$ and the static contribution to $S_\rho(q,\omega)$.

For $q\neq 0$, any finite electron-phonon coupling seems to shift the phonon dispersion away from $\omega=\pm\omega_0$, cf. Fig. 4.14. Exact diagonalization data for the spinless Holstein model [27] suggest that $B_Q(q,\pm\omega_0)$ vanishes and therefore $B_Q^0(q,\omega)$ and $B_Q^1(q,\omega)$ compensate each other.[2] In general, for $q\neq 0$, both $B_Q(q,\omega)$ and $S_\rho(q,\omega)$ contain signatures of the phonon dispersion as well as the particle-hole continuum, although the spectral weights may be very different.

The condition $B_Q(q,\omega_0)\geq 0$ sets an upper bound to the integral in Eq. (B.13),

$$\mathcal{P}\int_0^\infty d\omega\ \frac{\omega}{\left(\omega^2-\omega_0^2\right)^2}\,S_\rho(q,\omega)\leq\frac{1}{8\lambda t\,\omega_0^2}\,. \tag{B.17}$$

For the integral to converge, $S_\rho(q,\omega)$ has to vanish when approaching ω_0. Thus, a nonzero electron-phonon interaction splits the charge spectrum at $\omega=\omega_0$.

[2] In general, this need not be the case.

Further insight into the distribution of spectral weight can be obtained from the sum rules (B.14) and (B.15). We restrict our discussion to $B_Q(q,\omega)$, but the same arguments hold for $S_\rho(q,\omega)$. For $\omega > 0$, $B_Q(q,\omega) \geq 0$ but the prefactor $(\omega^2 - \omega_0^2)$ changes sign at ω_0. This sign change divides the frequency axis into regions $\omega < \omega_0$ and $\omega > \omega_0$, whose integrated spectral weights have to compensate each other in the sum rule.[3] Note that spectral weight at $\omega = 0$ and $\omega = \omega_0$ does not contribute to the sum rule, therefore the noninteracting phonon dispersion fulfills Eq. (B.15) trivially. By adiabatically switching on the electron-phonon coupling, the particle-hole continuum enters $B_Q(q,\omega)$ and spectral weight has to be redistributed to fulfill Eq. (B.15). For wave vectors such that the particle-hole continuum only enters one of the two regions, spectral weight has to appear in the other region. This can be most easily achieved by shifting the phonon dispersion. Both the hardening of the phonon dispersion for $\omega_0 \gg t$ [27, 185], and the hybridization with the particle-hole continuum as well as the phonon softening for $\omega_0 \ll t$, are consistent with the sum rule (B.15). Furthermore, in the Peierls phase, the charge gap (the lowest excitation at $q = \pi$) cannot become larger than ω_0, as the central peak does not contribute to the sum rule (B.15).

B.3. Sum rules for the total energy

In this section, we specify sum rules for the total energy of the Holstein model. In a first step, we show that the total energy can be calculated from the single-particle spectral functions of electrons and phonons. In a second step, we relate the bosonic parts of the total energy to the charge structure factor. The latter subsection is based on Ref. [P3].

B.3.1. Relations to the single-particle spectral functions

The total energy of the Holstein model can be calculated exactly from the single-particle spectra $A(k,\omega)$ and $B(q,\omega)$. Following Ref. [162], we use the fermionic and bosonic equations of motion to derive the sum rules

$$E_{\mathrm{el}} + E_{\mathrm{ep}} = \sum_k \int_{-\infty}^{\infty} d\omega\, \omega\, n_{\mathrm{F}}(\omega)\, A(k,\omega)\,, \tag{B.18}$$

$$E_{\mathrm{ph}} = \omega_0 \sum_q \int_{-\infty}^{\infty} d\omega\, n_{\mathrm{B}}(\omega)\, B(q,\omega)\,. \tag{B.19}$$

Here, $n_{\mathrm{F}}(\omega)$ and $n_{\mathrm{B}}(\omega)$ are the Fermi and Bose functions, respectively. The individual contributions to the total energy can also be split in a different way so that we obtain

$$E_{\mathrm{el}} + \frac{1}{2} E_{\mathrm{ep}} = \sum_k \int_{-\infty}^{\infty} d\omega\, \frac{\omega + \epsilon_k}{2}\, n_{\mathrm{F}}(\omega)\, A(k,\omega)\,, \tag{B.20}$$

$$E_{\mathrm{ph}} + \frac{1}{2} E_{\mathrm{ep}} = \sum_q \int_{-\infty}^{\infty} d\omega\, \omega\, n_{\mathrm{B}}(\omega)\, B(q,\omega)\,. \tag{B.21}$$

[3] However, the integrated weight $\int d\omega\, B_Q(q,\omega)$ may be very different for $\omega < \omega_0$ and $\omega > \omega_0$.

Here, $\epsilon_k = -2t\cos k$ is the free-electron dispersion. In the adiabatic limit ($\omega_0 = 0$), where the phonons lose their dynamics, Eq. (B.21) simplifies to

$$E_{\mathrm{ph}} + \frac{1}{2}E_{\mathrm{ep}} = E_{\mathrm{ph}}^0 = \frac{N_{\mathrm{ph}}}{\beta}\,, \tag{B.22}$$

where N_{ph} counts the number of bosonic degrees of freedom. This simplification can be proven using the sum rules for the bosonic energies in Eqs. (2.30)–(2.32). Together with Eq. (B.20), we obtain the sum rule (4.15) for the total energy in the adiabatic limit.[4]

B.3.2. Relations to the charge structure factor

For the Holstein model, the phonon propagators (2.27) and (2.28) as well as the bosonic energies (2.30)–(2.32) are determined by the time-displaced charge correlation function $C_\rho(q,\tau-\tau') = \langle\rho_q(\tau)\rho_{-q}(\tau')\rangle$. Therefore, the entire single-particle dynamics of the phonons is contained in $S_\rho(q,\omega)$. In particular, $B(q,\omega)$ is directly related to $S_\rho(q,\omega)$, as it was shown in the previous section. The energies (2.30)–(2.32) can be calculated from $S_\rho(q,\omega)$ via

$$E_{\mathrm{ph}}^{\mathrm{kin}} = \frac{E_{\mathrm{ph}}^0}{2} - 2\lambda t\int_0^\infty d\omega\, K_{--}(\omega/\omega_0,\beta\omega_0)\sum_q S_\rho(q,\omega)\,, \tag{B.23}$$

$$E_{\mathrm{ph}}^{\mathrm{pot}} = \frac{E_{\mathrm{ph}}^0}{2} + 2\lambda t\int_0^\infty d\omega\, K_{++}(\omega/\omega_0,\beta\omega_0)\sum_q S_\rho(q,\omega)\,, \tag{B.24}$$

$$E_{\mathrm{ep}} = -4\lambda t\int_0^\infty d\omega\, K_{+}(\omega/\omega_0,\beta\omega_0)\sum_q S_\rho(q,\omega)\,, \tag{B.25}$$

with the kernels ($x = \omega/\omega_0$, $y = \beta\omega_0$, $\omega_0 > 0$)

$$K_{\pm\pm}(x,y) = \frac{1}{4\pi\,(x^2-1)}\left\{x\tanh(xy/2)\coth(y/2) \pm \frac{xy\tanh(xy/2)}{2\sinh^2(y/2)}\right. \\ \left. \mp\frac{2x}{(x^2-1)}\left[\tanh(xy/2)\coth(y/2) - x^{\mp 1}\right]\right\}\,, \tag{B.26}$$

and $K_+ = K_{++} + K_{--}$, with

$$K_+(x,y) = \frac{x\tanh(xy/2)\coth(y/2) - 1}{2\pi\,(x^2-1)}\,. \tag{B.27}$$

The kernels are plotted in Fig. B.1 for different temperatures. At $T = 0$, K_{++} and K_+ are largest at $\omega = 0$ and decrease monotonically with increasing ω, whereas K_{--} is zero at $\omega = 0$ and has a maximum at $\omega = \omega_0$. Therefore, $E_{\mathrm{ph}}^{\mathrm{pot}}$ and E_{ep} mainly capture the

[4] In Eq. (B.22), both the kinetic and the potential energy of the phonons contribute with $E_{\mathrm{ph}}^0/2$. By contrast, Eq. (4.15) only contains the contribution of the potential energy, because the trivial kinetic term was already omitted at the level of the Hamiltonian (cf. Sec. 4.1.1). For the Holstein model, we have $N_{\mathrm{ph}} = L$.

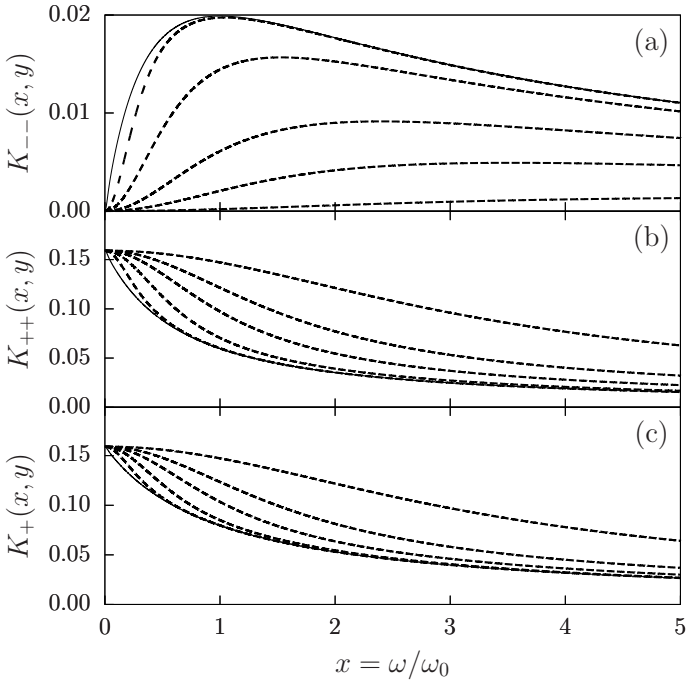

Figure B.1.: The kernels K_{--}, K_{++}, and K_{+}. Solid lines correspond to $T = 0$ results, whereas dashed lines correspond to $y = \beta\omega_0 = \{10, 5, 3, 2, 1\}$ as shown from the top in (a) and from the bottom in (b)–(c).

charge ordering. By contrast, because K_{--} filters out the zero-frequency contributions to $S_\rho(q,\omega)$, $E_{\text{ph}}^{\text{kin}}$ reveals the softening of the phonons and the opening of the Peierls gap. The same reasoning applies to the phonon spectral function. If calculated from $D_Q(q,\tau)$ [cf. Eq. (2.27)] it is dominated by the central mode in the Peierls phase. This mode is filtered out when using $D_P(q,\tau)$ [cf. Eq. (2.28)]. The kernels broaden significantly when the temperature becomes comparable to ω_0 but the qualitative behavior for $\omega \ll \omega_0$ remains unchanged.

C. Calculation of the specific heat from quantum Monte Carlo simulations

A reliable and precise calculation of the specific heat is a demanding task and strongly depends on the QMC method used. For QMC methods with an inherent Trotter discretization like the auxiliary-field QMC method [46], estimators for C_V may suffer from unphysical divergencies at low temperatures [141], but even for exact continuous-time QMC methods, the calculation of C_V remains challenging. There are mainly two approaches to calculate C_V. The first approach is based on a direct evaluation of C_V for any given temperature from the variance of the Hamiltonian,

$$C_V = k_B \beta^2 \left[\left\langle \hat{H}^2 \right\rangle - \left\langle \hat{H} \right\rangle^2 \right]. \tag{C.1}$$

This estimator is subject to large statistical fluctuations because of a mismatch of length scales that enter its calculation: while C_V itself scales linearly with system size L and vanishes for $T \to 0$,[1] we calculate C_V from the difference of two large numbers where each of them scales as $(\beta L)^2$ [193]. Particularly strong fluctuations at low temperatures therefore require very precise simulations. The second approach is based on the relation

$$C_V = \frac{\partial E(T)}{\partial T} \tag{C.2}$$

and exploits that the total energy $E(T)$ can be calculated with high accuracy on a dense temperature grid. $E(T)$ is then fitted to a functional form that can be differentiated exactly. However, finding an appropriate fitting ansatz for the entire temperature range is a difficult task itself and it is not a priori clear that it captures the physical situation. For a discussion of different fitting procedures and their limitations, see Ref. [179].

For the fermion-boson models studied in this thesis, the calculation of C_V is even more elaborate. Both approaches require a precise estimation of the first or even the second moment of the Hamiltonian from the sampled probability distribution. While the classical Monte Carlo method for the adiabatic limit gives direct access to these estimators (cf. Sec. 4.1.2), the QMC methods of Sec. 3.2 rely on an elimination of the bosonic fields from the probability distribution. Hence, the corresponding observables must be recovered from fermionic correlation functions using generating functionals. In Sec. 3.3 we have shown that the bosonic contributions to the total energy can be easily obtained from the distribution of vertices. A direct calculation of $\langle H^2 \rangle$ is complicated

[1] This is generally true for systems that obey the third law of thermodynamics. Note that we also consider the case of classical phonons in this thesis, where C_V reaches a constant at low temperatures. However, this small difference does not change much about the scaling argument.

by an increasing number of functional derivatives that must be evaluated to obtain the corresponding sum rules over fermionic fields. Then, the bosonic contributions to $\langle H^2 \rangle$ can be recovered from the distribution of vertices again.

In the following, we derive a direct estimator for the specific heat of the Holstein model using the SSE representation. Then, we discuss a physically-motivated fitting procedure proposed by Huscroft *et al.* [179] that only requires $E(T)$ as input data and therefore has a wider range of applicability. Finally, we provide an analysis of finite-size effects of C_V in the adiabatic limit.

C.1. Direct Monte Carlo estimator for the specific heat

We derive a direct estimator for the specific heat of the spinful Holstein model using the SSE representation, where all contributions to C_V are recovered from the distribution of vertices. We assume the vertices to be defined as in Eqs. (3.48)–(3.50). A similar estimator can also be derived for the CT-INT method, but then the electronic contributions must be calculated from the single-particle Green's function using Wick's theorem.

First moment of the Hamiltonian

For completeness, we review the estimator for the total energy that was already given in Sec. 3.4.4. The sum rules for the bosonic contributions (2.30)–(2.32) were derived without using translational invariance, but it is used in the following by rewriting $E = \beta^{-1} \int_0^\beta d\tau \, \langle H(\tau) \rangle$. For a configuration C_n, the SSE estimator for the total energy becomes

$$E(C_n) = E_{\mathrm{el}}(C_n) + E_{\mathrm{ph}}(C_n) + E_{\mathrm{ep}}(C_n) \,, \tag{C.3}$$

where the individual contributions are given by

$$E_{\mathrm{el}}(C_n) = -\frac{n_1}{\beta} \,, \tag{C.4}$$

$$E_{\mathrm{ph}}(C_n) = E_{\mathrm{ph}}^0 + \sum_{k=1}^{n_2} \left[\bar{P}_+(\tau_k - \tau_k') - \bar{P}_-(\tau_k - \tau_k') \right] - \lambda t C L N_\sigma^2 \,, \tag{C.5}$$

$$E_{\mathrm{ep}}(C_n) = -\frac{2n_2}{\beta} + 2\lambda t C L N_\sigma^2 \,. \tag{C.6}$$

Translational invariance of all vertices is contained in the averaged propagator

$$\bar{P}_\pm(\tau_k - \tau_k') = \frac{1}{\beta} \int_0^\beta d\tau \, \frac{P_\pm(\tau_k + \tau) P_\pm(\tau_k' + \tau)}{P_+(\tau_k - \tau_k')} \,. \tag{C.7}$$

Explicitly, it is given by ($\tau \in [-\beta, \beta]$)

$$\bar{P}_\pm(\tau) = \frac{1}{2\beta} \pm \frac{\omega_0}{4} \frac{\beta - |\tau|}{\beta} \left[\coth(\omega_0 \beta/2) - \frac{P_-(\tau)}{P_+(\tau)} \right] \pm \frac{\omega_0}{4} \frac{|\tau|}{\beta} \left[\coth(\omega_0 \beta/2) + \frac{P_-(\tau)}{P_+(\tau)} \right] . \tag{C.8}$$

Second moment of the Hamiltonian

To calculate the second moment of the Hamiltonian, we write its expectation value in a translationally invariant form, i.e.,

$$\left\langle \hat{H}^2 \right\rangle = \frac{1}{\beta^2} \iint_0^\beta d\tau d\tau' \left\langle H(\tau)\, H(\tau') \right\rangle . \tag{C.9}$$

As before, we split the total Hamiltonian into three contributions that are purely electronic, purely phononic, or contain the electron-phonon interaction.

The estimator for the purely electronic contribution has the same form as usual [193] and is given by

$$\frac{1}{\beta^2} \iint_0^\beta d\tau d\tau' \left\langle\!\!\left\langle H_{\mathrm{el}}(\tau)\, H_{\mathrm{el}}(\tau') \right\rangle\!\!\right\rangle_{C_n} = \frac{n_1\,(n_1-1)}{\beta^2} . \tag{C.10}$$

Also the mixing terms between the electronic part of the Hamiltonian and the remaining parts have simple estimators that are given by

$$\frac{2}{\beta^2} \iint_0^\beta d\tau d\tau' \left\langle\!\!\left\langle H_{\mathrm{el}}(\tau)\, H_{\mathrm{ph}}(\tau') \right\rangle\!\!\right\rangle_{C_n} = 2\, E_{\mathrm{el}}(C_n)\, E_{\mathrm{ph}}(C_n) , \tag{C.11}$$

$$\frac{2}{\beta^2} \iint_0^\beta d\tau d\tau' \left\langle\!\!\left\langle H_{\mathrm{el}}(\tau)\, H_{\mathrm{ep}}(\tau') \right\rangle\!\!\right\rangle_{C_n} = 2\, E_{\mathrm{el}}(C_n)\, E_{\mathrm{ep}}(C_n) . \tag{C.12}$$

The electronic and the bosonic contributions are recovered from vertices with different operator types and hence do not interfere in the total estimators.

The derivation of estimators is more complicated for correlation functions, where each part of the Hamiltonian contains bosonic fields. When we calculate the functional derivatives to obtain sum rules for the bosonic fields, we have to be aware of additional cross terms that do not appear for the individual energies. For example, the correlation function between the electron-phonon parts of the Hamiltonian becomes

$$\begin{aligned} \left\langle H_{\mathrm{ep}}(\tau)\, H_{\mathrm{ep}}(\tau') \right\rangle &= 4\lambda t\, P_+(\tau-\tau') \sum_i \left\langle \rho_i(\tau)\rho_i(\tau') \right\rangle \\ &+ (4\lambda t)^2 \int_0^\beta d\tau_1\, P_+(\tau-\tau_1) \int_0^\beta d\tau_2\, P_+(\tau'-\tau_2) \sum_{ij} \left\langle \rho_i(\tau)\rho_i(\tau_1)\rho_j(\tau')\rho_j(\tau_2) \right\rangle , \end{aligned} \tag{C.13}$$

The first term on the r.h.s. is an additional cross term. The corresponding estimator is

$$\frac{1}{\beta^2} \iint_0^\beta d\tau d\tau' \left\langle\!\!\left\langle H_{\mathrm{ep}}(\tau)\, H_{\mathrm{ep}}(\tau') \right\rangle\!\!\right\rangle_{C_n} = E_{\mathrm{ep}}(C_n)^2 - \frac{4n_2}{\beta^2} - \frac{E_{\mathrm{ep}}(C_n)}{\beta} . \tag{C.14}$$

For the remaining terms, we do not specify the correlation functions because they become too lengthy. We obtain the estimators

$$\frac{2}{\beta^2} \iint_0^\beta d\tau d\tau' \left\langle\!\!\left\langle H_{\mathrm{ep}}(\tau)\, H_{\mathrm{ph}}(\tau') \right\rangle\!\!\right\rangle_{C_n} = 2\, E_{\mathrm{ep}}(C_n)\, E_{\mathrm{ph}}(C_n) + \frac{4\lambda t C L N_\sigma^2}{\beta} \tag{C.15}$$

and

$$\frac{1}{\beta^2}\iint_0^\beta d\tau d\tau' \left\langle\!\!\left\langle H_{\mathrm{ph}}(\tau)\, H_{\mathrm{ph}}(\tau')\right\rangle\!\!\right\rangle_{C_n} = E_{\mathrm{ph}}(C_n)^2 + L\, P_+(0)\left[\bar{P}_+(0) - \bar{P}_-(0)\right] \qquad \text{(C.16)}$$
$$- \sum_{k=1}^{n_2}\left[\bar{P}_+(\tau_k - \tau_k') - \bar{P}_-(\tau_k - \tau_k')\right]^2 + \sum_{k=1}^{n_2}\frac{Z(\tau_k - \tau_k')}{P_+(\tau_k - \tau_k')} - \frac{2\lambda t C L N_\sigma^2}{\beta}\,.$$

For the latter, we introduced an additional function

$$Z(\tau) = \frac{\omega_0^3}{\beta^2}\, e^{(\beta-\tau)\omega_0}\, n_{\mathrm{B}}(\omega_0)\left[\tau^2 + \beta\,(\beta + 2\tau)\, n_{\mathrm{B}}(\omega_0) + 2\beta^2 n_{\mathrm{B}}(\omega_0)^2\right] \qquad \text{(C.17)}$$

that is defined for $\tau \in [0, \beta)$. To evaluate $Z(\tau)$ for $\tau < 0$, we use $Z(\tau + \beta) = Z(\tau)$. Here, $n_{\mathrm{B}}(\omega) = [\exp(\beta\omega) - 1]^{-1}$ is the Bose function.

Estimator for the CT-INT method

Although we derived the above estimator for the interaction vertex in the SSE representation, it can be easily transferred to the CT-INT method. Because the vertex for the retarded interaction is very similar in both methods, all estimators that only contain bosonic parts of the Hamiltonian directly transfer to the CT-INT method. Using the action as defined in Eq. (3.32), we only have to replace $C \to 2\delta^2$. Furthermore, the purely electronic contributions to the first and second moment of the Hamiltonian must be calculated from the single-particle Green's function using Wick's theorem. Finally, the mixing terms (C.11) and (C.12) have the same form as before, only the electronic contribution has to be estimated from the Green's function again.

C.2. Maximum entropy approach to the specific heat

To obtain the specific heat only from $E(T)$, Huscroft *et al.* [179] proposed a method that is superior to direct numerical differentiation, yields smooth curves, and gives error bars. It is based on the ansatz

$$E(T) = \int_{-\infty}^{\infty} d\omega\, \omega\left[n_{\mathrm{F}}(\omega, T)\, \rho_{\mathrm{F}}(\omega) + n_{\mathrm{B}}(\omega, T)\, \rho_{\mathrm{B}}(\omega)\right], \qquad \text{(C.18)}$$

corresponding to a spectral decomposition of the energy into fermionic (F) and bosonic (B) contributions. The temperature dependence of $E(T)$ is assumed to arise only from the Fermi and Bose functions $n_{\mathrm{F}}(\omega, T)$ and $n_{\mathrm{B}}(\omega, T)$, respectively. Considering Eq. (C.18) as an inverse problem of the form

$$E(T) = \int_{-\infty}^{\infty} d\omega\, K(\omega, T)\, \rho(\omega)\,, \qquad \text{(C.19)}$$

the maximum-entropy method [190] can be used to obtain the most likely solution for $\rho(\omega)$ that is compatible with the data $E(T)$ (within error bars) and contains the least information, i.e., only features supported by the data. In practice, $\rho(\omega)$ consists of

the fermionic and bosonic contributions $\rho_{\mathrm{F}}(\omega)$ and $\rho_{\mathrm{B}}(\omega)$ and the kernel $K(\omega, T)$ is defined from a comparison to Eq. (C.18). The specific heat then follows from $C_V(T) = \int_{-\infty}^{\infty} d\omega\, \partial_T K(\omega, T)\, \rho(\omega)$ and is explicitly given by

$$C_V(T) = k_{\mathrm{B}} \int_{-\infty}^{\infty} d\omega \left(\frac{\beta\omega}{2}\right)^2 \left[\frac{\rho_{\mathrm{F}}(\omega)}{\cosh^2(\beta\omega/2)} + \frac{\rho_{\mathrm{B}}(\omega)}{\sinh^2(\beta\omega/2)}\right]. \tag{C.20}$$

To invert Eq. (C.18), Huscroft *et al.* [179] assumed $\rho_{\mathrm{F}}(\omega) \geq 0$ and $\mathrm{sgn}(\omega)\rho_{\mathrm{B}}(\omega) \geq 0$. This choice may lead to fits that violate $C_V \geq 0$. The positivity of C_V can be imposed by choosing $\rho_{\mathrm{B}}(\omega) \geq 0$, which is only possible for Hamiltonians with bosonic contributions, e.g., the Holstein model. From our experience it is better not to impose $C_V \geq 0$, because then the fitting procedure is less restrictive. In practice, we did not encounter any problems where C_V becomes negative. Although the ansatz (C.18) is well motivated by the sum rules given in App. B.3.1, it neglects the temperature dependence of the spectral functions. In the end, the maximum entropy approach makes use of a noninteracting system to fit the temperature-dependent energy $E(T)$ of an interacting system. Especially at finite-temperature phase transitions or at low temperatures this fitting procedure may have problems. In Sec. 4.2, we mainly use the maximum entropy fits as a guide to the eye for the exact C_V data. For our simulations, the maximum entropy fits match the exact C_V data very well because the QMC estimates for $E(T)$ are very precise. Note that it is also possible to obtain error bars from the maximum entropy approach because $C_V(T)$ is an integrated quantity of the spectral function $\rho(\omega)$ [190].

C.3. Finite-size analysis in the adiabatic limit

In Sec. 4.1.3 we discussed the low-temperature behavior of C_V, and observed the appearance of a peak related to the ordering of the lattice. A reliable analysis also requires a study of finite-size effects. Therefore, we present in Fig. C.1 C_V as a function of temperature for different system sizes ranging from $L = 22$ to $L = 162$, and for two values of the electron-phonon coupling. Our discussion is based on Ref. [P4].

Figure C.1(a) shows data for the spinless Holstein model with $\lambda = 0.5$. For temperatures $k_{\mathrm{B}}T/t > 0.1$, C_V has already converged at the smallest L considered, whereas for lower temperatures a clear dependence on the lattice size is visible. Between $L = 22$ and $L = 82$, both the position of the low-temperature peak and its height change substantially. The upturn to its maximum is only converged for the two largest lattice sizes. At $\lambda = 1$ [Fig. C.1(b)], the peak appears at higher temperatures and its upturn is already converged for $L = 22$. While the height of the maximum has converged for $L = 82$, the subsequent downturn to the lowest temperatures measured still changes from $L = 82$ to $L = 162$. Note that error bars are large in this temperature regime and adjacent data points are not independent due to the use of parallel tempering.

For the spinless SSH model, finite-size effects on C_V are also visible at high temperatures [Fig. C.1(c) and C.1(d)]. However, these effects are simply related to the fact that only $L - 1$ phonon modes contribute to C_V because the length of the chain is fixed and the $k = 0$ mode drops out of the Hamiltonian. The finite-size effects at low temperatures

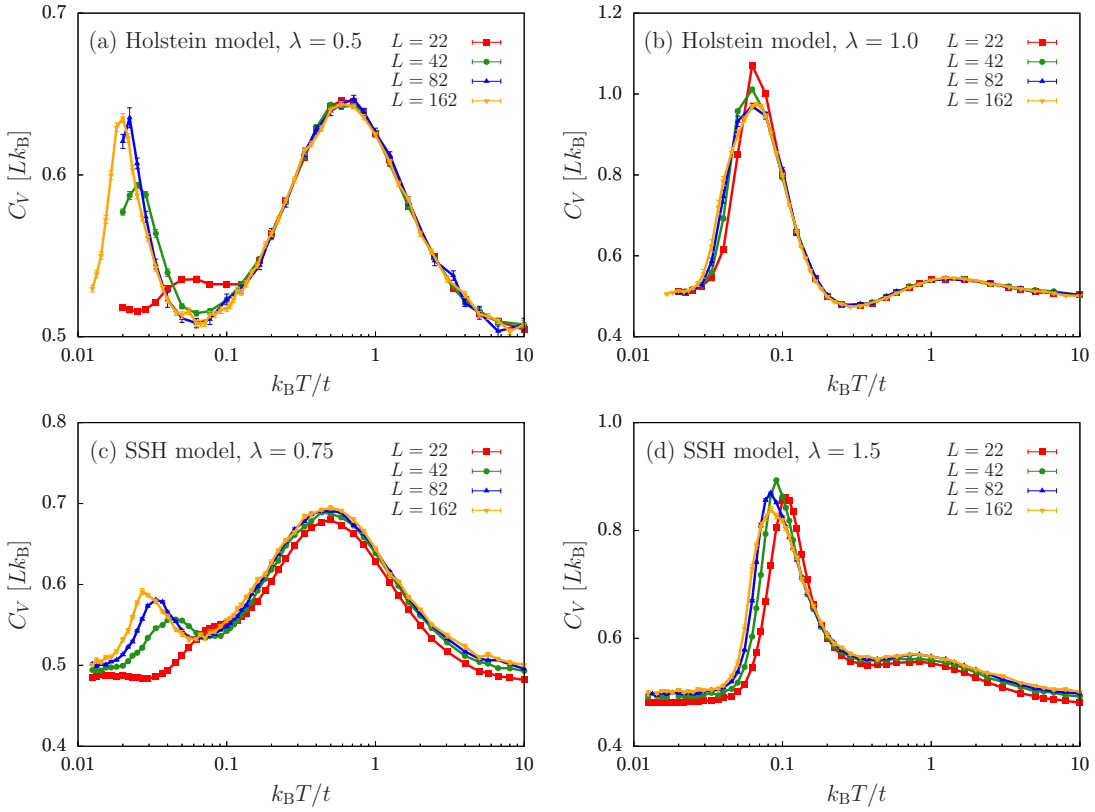

Figure C.1.: Specific heat of the spinless Holstein model [(a), (b)] and the spinless SSH model [(c), (d)] for different system sizes L and in the adiabatic limit. Data were obtained using the classical Monte Carlo method described in Sec. 4.1.2.

are slightly larger than for the Holstein model. For $\lambda = 0.75$ [Fig. C.1(c)], the peak position and height still change up to $L = 162$. Compared to the finite-size convergence in the Holstein model at $\lambda = 0.5$ [Fig. C.1(a)], we believe that the upturn at $L = 162$ is converged. For $\lambda = 1.5$ [Fig. C.1(d)] it is indeed converged, but the subsequent downturn again shows finite-size effects.

The above analysis suggests that except for the downturn at the lowest temperatures considered, the C_V data shown in Fig. 4.2 have converged with respect to L. The finite-size effects on C_V may also be consulted in order to estimate finite-size effects on the spectral functions.

Bibliography

[1] D. van Delft and P. Kes: *The discovery of superconductivity.* Physics Today **63**, 38 (2010).

[2] L. N. Cooper: *Bound Electron Pairs in a Degenerate Fermi Gas.* Phys. Rev. **104**, 1189 (1956).

[3] J. Bardeen, L. N. Cooper, and J. R. Schrieffer: *Theory of Superconductivity.* Phys. Rev. **108**, 1175 (1957).

[4] S. Tomonaga: *Remarks on Bloch's Method of Sound Waves applied to Many-Fermion Problems.* Prog. Theor. Phys. **5**, 544 (1950).

[5] J. M. Luttinger: *An Exactly Soluble Model of a Many-Fermion System.* J. Math. Phys. **4**, 1154 (1963).

[6] A. Luther and V. J. Emery: *Backward scattering in the One-Dimensional Electron Gas.* Phys. Rev. Lett. **33**, 589 (1974).

[7] R. E. Peierls: *Quantum Theory of Solids.* Clarendon Press, Oxford (1955).

[8] W. P. Su, J. R. Schrieffer, and A. J. Heeger: *Solitons in Polyacetylene.* Phys. Rev. Lett. **42**, 1698 (1979).

[9] A. J. Heeger, S. Kivelson, J. R. Schrieffer, and W. P. Su: *Solitons in conducting polymers.* Rev. Mod. Phys. **60**, 781 (1988).

[10] X.-L. Qi and S.-C. Zhang: *Topological insulators and superconductors.* Rev. Mod. Phys. **83**, 1057 (2011).

[11] A. S. Alexandrov (editor): *Polarons in Advanced Materials.* Canopus Publishing and Springer Verlag GmbH, Bristol (UK) (2007).

[12] L. D. Landau: *Über die Bewegung der Elektronen in Kristallgitter.* Phys. Z. Sowjetunion **3**, 644 (1933).

[13] K. Yonemitsu and K. Nasu: *Theory of photoinduced phase transitions in itinerant electron systems.* Phys. Rep. **465**, 1 (2008).

[14] T. Holstein: *Studies of polaron motion.* Annal. Phys. **8**, 325 (1959).

[15] T. Holstein: *Studies of polaron motion.* Annal. Phys. **8**, 343 (1959).

[16] H. Bethe: *Zur Theorie der Metalle.* Z. Phys. **71**, 205 (1931).

[17] E. H. Lieb and F. Y. Wu: *Absence of Mott Transition in an Exact Solution of the Short-Range, One-Band Model in One Dimension.* Phys. Rev. Lett. **20**, 1445 (1968).

[18] F. H. L. Essler, H. Frahm, F. Göhmann, A. Klümper, and V. E. Korepin: *The One-Dimensional Hubbard Model.* Cambridge University Press, Cambridge (2010).

[19] J. K. Freericks and E. H. Lieb: *Ground state of a general electron-phonon Hamiltonian is a spin singlet.* Phys. Rev. B **51**, 2812 (1995).

[20] J. E. Hirsch and E. Fradkin: *Phase diagram of one-dimensional electron-phonon systems. II. The molecular-crystal model.* Phys. Rev. B **27**, 4302 (1983).

[21] L. G. Caron and C. Bourbonnais: *Two-cutoff renormalization and quantum versus classical aspects for the one-dimensional electron-phonon system.* Phys. Rev. B **29**, 4230 (1984).

[22] E. Jeckelmann, C. Zhang, and S. R. White: *Metal-insulator transition in the one-dimensional Holstein model at half filling.* Phys. Rev. B **60**, 7950 (1999).

[23] R. T. Clay and R. P. Hardikar: *Intermediate Phase of the One Dimensional Half-Filled Hubbard-Holstein Model.* Phys. Rev. Lett. **95**, 096401 (2005).

[24] H. Bakrim and C. Bourbonnais: *Nature of ground states in one-dimensional electron-phonon Hubbard models at half filling.* Phys. Rev. B **91**, 085114 (2015).

[25] R. H. McKenzie, C. J. Hamer, and D. W. Murray: *Quantum Monte Carlo study of the one-dimensional Holstein model of spinless fermions.* Phys. Rev. B **53**, 9676 (1996).

[26] R. J. Bursill, R. H. McKenzie, and C. J. Hamer: *Phase Diagram of the One-Dimensional Holstein Model of Spinless Fermions.* Phys. Rev. Lett. **80**, 5607 (1998).

[27] M. Hohenadler, G. Wellein, A. R. Bishop, A. Alvermann, and H. Fehske: *Spectral signatures of the Luttinger liquid to the charge-density-wave transition.* Phys. Rev. B **73**, 245120 (2006).

[28] R. P. Hardikar and R. T. Clay: *Phase diagram of the one-dimensional Hubbard-Holstein model at half and quarter filling.* Phys. Rev. B **75**, 245103 (2007).

[29] S. Ejima and H. Fehske: *Luttinger parameters and momentum distribution function for the half-filled spinless fermion Holstein model: A DMRG approach.* Europhys. Lett. **87**, 27001 (2009).

[30] H. Fehske, G. Hager, and E. Jeckelmann: *Metallicity in the half-filled Holstein-Hubbard model.* Europhys. Lett. **84**, 57001 (2008).

[31] M. Hohenadler and H. Fehske: *Density waves in strongly correlated quantum chains.* arXiv:1706.00470 (2017).

[32] J. Greitemann, S. Hesselmann, S. Wessel, F. F. Assaad, and M. Hohenadler: *Finite-size effects in Luther-Emery phases of Holstein and Hubbard models.* Phys. Rev. B **92**, 245132 (2015).

[33] J. K. Cullum and R. A. Willoughby: *Lanczos Algorithms for Large Symmetric Eigenvalue Computations*, volume I & II. Birkhäuser, Boston (1985).

[34] S. White: *Density matrix formulation for quantum renormalization groups.* Phys. Rev. Lett. **69**, 2863 (1992).

[35] S. White: *Density-matrix algorithms for quantum renormalization groups.* Phys. Rev. B **48**, 10345 (1993).

[36] J. Gubernatis, N. Kawashima, and P. Werner: *Quantum Monte Carlo Methods: Algorithms for Lattice Models.* Cambridge University Press, Cambridge (2016).

[37] U. Schollwöck: *The density-matrix renormalization group.* Rev. Mod. Phys. **77**, 259 (2005).

[38] U. Schollwöck: *The density-matrix renormalization group in the age of matrix product states.* Annals of Physics **326**, 96 (2011).

[39] E. Jeckelmann and S. R. White: *Density-matrix renormalization-group study of the polaron problem in the Holstein model.* Phys. Rev. B **57**, 6376 (1998).

[40] C. Zhang, E. Jeckelmann, and S. R. White: *Density Matrix Approach to Local Hilbert Space Reduction.* Phys. Rev. Lett. **80**, 2661 (1998).

[41] C. Zhang, E. Jeckelmann, and S. R. White: *Dynamical properties of the one-dimensional Holstein model.* Phys. Rev. B **60**, 14092 (1999).

[42] E. Jeckelmann and H. Fehske: *Exact numerical methods for electron-phonon problems.* Riv. Nuovo Cimento **30** (2007).

[43] A. Weiße, H. Fehske, G. Wellein, and A. R. Bishop: *Optimized phonon approach for the diagonalization of electron-phonon problems.* Phys. Rev. B **62**, R747 (2000).

[44] M. Hohenadler and T. C. Lang: *Autocorrelations in Quantum Monte Carlo Simulations of Electron-Phonon Models.* In *Computational Many-Particle Physics*, edited by H. Fehske, R. Schneider, and A. Weiße, Springer Berlin Heidelberg, Berlin, Heidelberg, pp. 357–366 (2008).

[45] J. E. Hirsch, R. L. Sugar, D. J. Scalapino, and R. Blankenbecler: *Monte Carlo simulations of one-dimensional fermion systems.* Phys. Rev. B **26**, 5033 (1982).

[46] R. Blankenbecler, D. J. Scalapino, and R. L. Sugar: *Monte Carlo calculations of coupled boson-fermion systems. I.* Phys. Rev. D **24**, 2278 (1981).

[47] R. T. Scalettar: *World-line quantum Monte Carlo.* In *Quantum Monte Carlo Methods in Physics and Chemistry*, edited by M. P. Nightingale and C. J. Umrigar, Kluwer Academic Publishers, Dordrecht, pp. 65–100 (1998).

[48] M. Hohenadler, H. G. Evertz, and W. von der Linden: *Quantum Monte Carlo and variational approaches to the Holstein model.* Phys. Rev. B **69**, 024301 (2004).

[49] M. Hohenadler, D. Neuber, W. von der Linden, G. Wellein, J. Loos, and H. Fehske: *Photoemission spectra of many-polaron systems.* Phys. Rev. B **71**, 245111 (2005).

[50] R. H. Swendsen and J.-S. Wang: *Nonuniversal critical dynamics in Monte Carlo simulations.* Phys. Rev. Lett. **58**, 86 (1987).

[51] U. Wolff: *Collective Monte Carlo Updating for Spin Systems.* Phys. Rev. Lett. **62**, 361 (1989).

[52] H. G. Evertz, G. Lana, and M. Marcu: *Cluster algorithm for vertex models.* Phys. Rev. Lett. **70**, 875 (1993).

[53] N. V. Prokof'ev, B. V. Svistunov, and I. S. Tupitsyn: *Exact, complete, and universal continuous-time worldline Monte Carlo approach to the statistics of discrete quantum systems.* Sov. Phys. JETP **87**, 310 (1998).

[54] A. W. Sandvik: *Stochastic series expansion method with operator-loop update.* Phys. Rev. B **59**, R14157 (1999).

[55] O. Syljuasen and A. W. Sandvik: *Quantum Monte Carlo with directed loops.* Phys. Rev. E **66**, 046701 (2002).

[56] F. F. Assaad and H. G. Evertz: *World-line and Determinantal Quantum Monte Carlo Methods for Spins, Phonons and Electrons.* In *Computational Many-Particle Physics*, edited by H. Fehske, R. Schneider, and A. Weiße, Springer Berlin Heidelberg, Berlin, Heidelberg, pp. 277–356 (2008).

[57] R. T. Scalettar, D. J. Scalapino, R. L. Sugar, and D. Toussaint: *Hybrid molecular-dynamics algorithm for the numerical simulation of many-electron systems.* Phys. Rev. B **36**, 8632 (1987).

[58] S. Duane, A. Kennedy, B. J. Pendleton, and D. Roweth: *Hybrid Monte Carlo.* Phys. Lett. B **195**, 216 (1987).

[59] S. Beyl, F. Goth, and F. F. Assaad: *Revisiting the Hybrid Quantum Monte Carlo Method for Hubbard and Electron-Phonon Models.* arXiv:1708.03661 (2017).

[60] R. P. Feynman: *Slow Electrons in a Polar Crystal.* Phys. Rev. **97**, 660 (1955).

[61] H. De Raedt and A. Lagendijk: *Critical Quantum Fluctuations and Localization of the Small Polaron.* Phys. Rev. Lett. **49**, 1522 (1982).

[62] H. De Raedt and A. Lagendijk: *Numerical calculation of path integrals: The small-polaron model.* Phys. Rev. B **27**, 6097 (1983).

[63] P. E. Kornilovitch and E. R. Pike: *Polaron effective mass from Monte Carlo simulations.* Phys. Rev. B **55**, R8634 (1997).

[64] P. E. Kornilovitch: *Continuous-Time Quantum Monte Carlo Algorithm for the Lattice Polaron.* Phys. Rev. Lett. **81**, 5382 (1998).

[65] N. V. Prokof'ev and B. V. Svistunov: *Polaron Problem by Diagrammatic Quantum Monte Carlo.* Phys. Rev. Lett. **81**, 2514 (1998).

[66] P. E. Kornilovitch: *Path-integral approach to lattice polarons.* J. Phys.: Condens. Matter **19**, 255213 (2007).

[67] A. N. Rubtsov, V. V. Savkin, and A. I. Lichtenstein: *Continuous-time quantum Monte Carlo method for fermions.* Phys. Rev. B **72**, 035122 (2005).

[68] E. Gull, A. J. Millis, A. I. Lichtenstein, A. N. Rubtsov, M. Troyer, and P. Werner: *Continuous-time Monte Carlo methods for quantum impurity models.* Rev. Mod. Phys. **83**, 349 (2011).

[69] A. Georges, G. Kotliar, W. Krauth, and M. J. Rozenberg: *Dynamical mean-field theory of strongly correlated fermion systems and the limit of infinite dimensions.* Rev. Mod. Phys. **68**, 13 (1996).

[70] F. F. Assaad and T. C. Lang: *Diagrammatic determinantal quantum Monte Carlo methods: Projective schemes and applications to the Hubbard-Holstein model.* Phys. Rev. B **76**, 035116 (2007).

[71] M. Hohenadler, H. Fehske, and F. F. Assaad: *Dynamic charge correlations near the Peierls transition.* Phys. Rev. B **83**, 115105 (2011).

[72] Z. Cai, U. Schollwöck, and L. Pollet: *Identifying a Bath-Induced Bose Liquid in Interacting Spin-Boson Models.* Phys. Rev. Lett. **113**, 260403 (2014).

[73] A. W. Sandvik: *Stochastic series expansion method for quantum Ising models with arbitrary interactions.* Phys. Rev. E **68**, 056701 (2003).

[74] M. Hohenadler, S. Wessel, M. Daghofer, and F. F. Assaad: *Interaction-range effects for fermions in one dimension.* Phys. Rev. B **85**, 195115 (2012).

[75] P. Werner, A. Comanac, L. de' Medici, M. Troyer, and A. J. Millis: *Continuous-Time Solver for Quantum Impurity Models.* Phys. Rev. Lett. **97**, 076405 (2006).

[76] P. Werner and A. J. Millis: *Dynamical Screening in Correlated Electron Materials.* Phys. Rev. Lett. **104**, 146401 (2010).

[77] H. Hafermann: *Self-energy and vertex functions from hybridization-expansion continuous-time quantum Monte Carlo for impurity models with retarded interaction.* Phys. Rev. B **89**, 235128 (2014).

[78] P. Werner and M. Casula: *Dynamical screening in correlated electron systems—from lattice models to realistic materials.* J. Phys.: Condens. Matter **28**, 383001 (2016).

[79] P. Sun and G. Kotliar: *Extended dynamical mean-field theory and* GW *method.* Phys. Rev. B **66**, 085120 (2002).

[80] T. Ayral, S. Biermann, and P. Werner: *Screening and nonlocal correlations in the extended Hubbard model from self-consistent combined GW and dynamical mean field theory.* Phys. Rev. B **87**, 125149 (2013).

[81] L. Wang, Y.-H. Liu, J. Imriška, P. N. Ma, and M. Troyer: *Fidelity Susceptibility Made Simple: A Unified Quantum Monte Carlo Approach.* Phys. Rev. X **5**, 031007 (2015).

[82] A. W. Sandvik and J. Kurkijärvi: *Quantum Monte Carlo simulation method for spin systems.* Phys. Rev. B **43**, 5950 (1991).

[83] R. W. Kühne and U. Löw: *Thermodynamical properties of a spin-$\frac{1}{2}$ Heisenberg chain coupled to phonons.* Phys. Rev. B **60**, 12125 (1999).

[84] A. Bühler, G. S. Uhrig, and J. Oitmaa: *Thermodynamics of a spin-$\frac{1}{2}$ chain coupled to Einstein phonons.* Phys. Rev. B **70**, 214429 (2004).

[85] A. C. Hewson: *The Kondo Problem to Heavy Fermions.* Cambridge University Press, Cambridge (1993).

[86] U. Weiss: *Quantum Dissipative Systems.* World Scientific, Singapore (1999).

[87] P. Sengupta, A. W. Sandvik, and D. K. Campbell: *Peierls transition in the presence of finite-frequency phonons in the one-dimensional extended Peierls-Hubbard model at half-filling.* Phys. Rev. B **67**, 245103 (2003).

[88] A. C. Hewson and D. Meyer: *Numerical renormalization group study of the Anderson-Holstein impurity model.* J. Phys.: Condens. Matter **14**, 427 (2002).

[89] J. W. Negele and H. Orland: *Quantum Many-Particle Systems.* Perseus Books, Reading, MA (1998).

[90] A. Altland and B. Simons: *Condensed Matter Field Theory.* Cambridge University Press, Cambridge (2010).

[91] A. W. Sandvik, R. R. P. Singh, and D. K. Campbell: *Quantum Monte Carlo in the interaction representation: Application to a spin-Peierls model.* Phys. Rev. B **56**, 14510 (1997).

[92] H. G. Evertz: *Computer Simulations*. Lecture Notes, TU Graz (2009).

[93] A. D. Sokal: *Monte Carlo Methods in Statistical Mechanics: Foundations and New Algorithms*. In *Functional Integration, NATO ASI Series (Series B: Physics)*, volume 361, edited by C. DeWitt-Morette, P. Cartier, and A. Folacci, Springer, Boston, MA (1997).

[94] M. Troyer and U.-J. Wiese: *Computational Complexity and Fundamental Limitations to Fermionic Quantum Monte Carlo Simulations*. Phys. Rev. Lett. **94**, 170201 (2005).

[95] N. Metropolis, A. W. Rosenbluth, M. N. Rosenbluth, A. H. Teller, and E. Teller: *Equation of State Calculations by Fast Computing Machines*. J. Chem. Phys. **21**, 1087 (1953).

[96] W. K. Hastings: *Monte Carlo Sampling Methods Using Markov Chains and Their Applications*. Biometrika **57**, 97 (1970).

[97] W. Janke: *Monte Carlo Methods in Classical Statistical Physics*. In *Computational Many-Particle Physics*, edited by H. Fehske, R. Schneider, and A. Weiße, Springer Berlin Heidelberg, Berlin, Heidelberg, pp. 79–140 (2008).

[98] D. J. Luitz and F. F. Assaad: *Weak-coupling continuous-time quantum Monte Carlo study of the single impurity and periodic Anderson models with s-wave superconducting baths*. Phys. Rev. B **81**, 024509 (2010).

[99] D. J. Luitz: *Numerical methods and applications in many fermion systems*. Ph.D. thesis, Julius-Maximilians-Universität Würzburg (2012).

[100] F. F. Assaad: *DMFT at 25: Infinite Dimensions: Lecture Notes of the Autumn School on Correlated Electrons*. Verlag des Forschungszentrum Jülich, Jülich, chapter 7. Continuous-time QMC Solvers for Electronic Systems in Fermionic and Bosonic Baths (2014).

[101] M. Hohenadler and F. F. Assaad: *Peierls to superfluid crossover in the one-dimensional, quarter-filled Holstein model*. J. Phys.: Condens. Matter **25**, 014005 (2013).

[102] M. Hohenadler and F. F. Assaad: *Excitation spectra and spin gap of the half-filled Holstein-Hubbard model*. Phys. Rev. B **87**, 075149 (2013).

[103] M. Hohenadler: *Charge and spin correlations of a Peierls insulator after a quench*. Phys. Rev. B **88**, 064303 (2013).

[104] M. Hohenadler: *Interplay of Site and Bond Electron-Phonon Coupling in One Dimension*. Phys. Rev. Lett. **117**, 206404 (2016).

[105] M. Hohenadler, F. F. Assaad, and H. Fehske: *Effect of Electron-Phonon Interaction Range for a Half-Filled Band in One Dimension.* Phys. Rev. Lett. **109**, 116407 (2012).

[106] L. Pollet: *Recent developments in quantum Monte Carlo simulations with applications for cold gases.* Rep. Prog. Phys. **75**, 094501 (2012).

[107] L. Pollet, K. V. Houcke, and S. M. Rombouts: *Engineering local optimality in quantum Monte Carlo algorithms.* J. Comp. Phys. **225**, 2249 (2007).

[108] J. E. Hirsch: *Discrete Hubbard-Stratonovich transformation for fermion lattice models.* Phys. Rev. B **28**, 4059 (1983).

[109] S.-J. Gu: *Fidelity approach to quantum phase transitions.* Int. J. Mod. Phys. B **24**, 4371 (2010).

[110] W.-L. You, Y.-W. Li, and S.-J. Gu: *Fidelity, dynamic structure factor, and susceptibility in critical phenomena.* Phys. Rev. E **76**, 022101 (2007).

[111] D. Schwandt, F. Alet, and S. Capponi: *Quantum Monte Carlo Simulations of Fidelity at Magnetic Quantum Phase Transitions.* Phys. Rev. Lett. **103**, 170501 (2009).

[112] A. F. Albuquerque, F. Alet, C. Sire, and S. Capponi: *Quantum critical scaling of fidelity susceptibility.* Phys. Rev. B **81**, 064418 (2010).

[113] A. W. Sandvik: *A generalization of Handscomb's quantum Monte Carlo scheme-application to the 1D Hubbard model.* J. Phys. A: Math. Gen. **25**, 3667 (1992).

[114] J. Greitemann: *Quantum Monte Carlo Investigation of the One-dimensional Hubbard-Holstein Model.* Master's thesis, RWTH Aachen (2015).

[115] F. Alet, S. Wessel, and M. Troyer: *Generalized directed loop method for quantum Monte Carlo simulations.* Phys. Rev. E **71**, 036706 (2005).

[116] A. Weiße and H. Fehske: *Peierls instability and optical response in the one-dimensional half-filled Holstein model of spinless fermions.* Phys. Rev. B **58**, 13526 (1998).

[117] J. Cardy: *Scaling and Renormalization in Statistical Physics.* Cambridge University Press, Cambridge (1996).

[118] P. Zanardi and N. Paunković: *Ground state overlap and quantum phase transitions.* Phys. Rev. E **74**, 031123 (2006).

[119] J. Voit: *One-dimensional Fermi liquids.* Rep. Prog. Phys. **57**, 977 (1995).

[120] G. Sun, A. K. Kolezhuk, and T. Vekua: *Fidelity at Berezinskii-Kosterlitz-Thouless quantum phase transitions.* Phys. Rev. B **91**, 014418 (2015).

[121] J. Voit: *Dynamical correlation functions of one-dimensional superconductors and Peierls and Mott insulators.* Eur. Phys. J. B **5**, 505 (1998).

[122] F. Denoyer, F. Comès, A. F. Garito, and A. J. Heeger: *X-Ray-Diffuse-Scattering Evidence for a Phase Transition in Tetrathiafulvalene Tetracyanoquinodimethane (TTF-TCNQ).* Phys. Rev. Lett. **35**, 445 (1975).

[123] R. Comès, S. M. Shapiro, G. Shirane, A. F. Garito, and A. J. Heeger: *Neutron-Scattering Study of the 38- and 54-K Phase Transitions in Deuterated Tetrathiafulvalene- Tetracyanoquinodimethane (TTF-TCNQ).* Phys. Rev. Lett. **35**, 1518 (1975).

[124] J. P. Pouget, S. Kagoshima, C. Schlenker, and J. Marcus: *Evidence for a Peierls transition in the blue bronzes K0.30MoO 3 and Rb0.30MoO3.* J. Phys. (Paris), Lett. **44**, 113 (1983).

[125] M. Hase, I. Terasaki, and K. Uchinokura: *Observation of the spin-Peierls transition in linear* Cu^{2+} *(spin-1/2) chains in an inorganic compound* $CuGeO_3$. Phys. Rev. Lett. **70**, 3651 (1993).

[126] J.-P. Pouget: *The Peierls instability and charge density wave in one-dimensional electronic conductors.* Comptes Rendus Physique **17**, 332 (2016).

[127] D. J. Scalapino, M. Sears, and R. A. Ferrell: *Statistical Mechanics of One-Dimensional Ginzburg-Landau Fields.* Phys. Rev. B **6**, 3409 (1972).

[128] P. A. Lee, T. M. Rice, and P. W. Anderson: *Fluctuation Effects at a Peierls Transition.* Phys. Rev. Lett. **31**, 462 (1973).

[129] R. A. Craven, M. B. Salamon, G. DePasquali, R. M. Herman, G. Stucky, and A. Schultz: *Specific Heat of Tetrathiofulvalinium-Tetracyanoquinodimethane (TTF-TCNQ) in the Vicinity of the Metal-Insulator Transition.* Phys. Rev. Lett. **32**, 769 (1974).

[130] T. Wei, A. J. Heeger, M. B. Salamon, and G. E. Delker: *Specific heat studies of the spin-peierls transition.* Solid State Commun. **21**, 595 (1977).

[131] X. Liu, J. Wosnitza, H. von Löhneysen, and R. K. Kremer: *Specific Heat Analysis of the Spin-Peierls Transition in CuGe* O_3. Phys. Rev. Lett. **75**, 771 (1995).

[132] D. K. Powell, J. W. Brill, Z. Zeng, and M. Greenblatt: *Specific heat of* $\alpha'-NaV_2O_5$ *at its spin-Peierls transition.* Phys. Rev. B **58**, R2937 (1998).

[133] R. S. Kwok, G. Gruner, and S. E. Brown: *Fluctuations and thermodynamics of the charge-density-wave phase transition.* Phys. Rev. Lett. **65**, 365 (1990).

[134] W. Dieterich: *Ginzburg-Landau theory of phase transitions in pseudo-one-dimensional systems.* Adv. Phys. **25**, 615 (1976).

[135] D. Schmeltzer, R. Zeyher, and W. Hanke: *Effect of quantum fluctuations on one-dimensional electron-phonon systems: The Su-Schrieffer-Heeger model.* Phys. Rev. B **33**, 5141 (1986).

[136] M. Nakahara and K. Maki: *Quantum corrections to solitons in polyacetylene.* Phys. Rev. B **25**, 7789 (1982).

[137] M. Braden, G. Wilkendorf, J. Lorenzana, M. Aïn, G. J. McIntyre, M. Behruzi, G. Heger, G. Dhalenne, and A. Revcolevschi: *Structural analysis of* $CuGeO_3$*: Relation between nuclear structure and magnetic interaction.* Phys. Rev. B **54**, 1105 (1996).

[138] N. W. Ashcroft and N. D. Mermin: *Solid State Physics.* Saunders College Publishing, Philadelphia (1976).

[139] C. H. Aits and U. Löw: *Thermodynamic properties of the two-dimensional* $S = \frac{1}{2}$ *Heisenberg antiferromagnet coupled to bond phonons.* Phys. Rev. B **68**, 184416 (2003).

[140] C. Karrasch and J. E. Moore: *Luttinger liquid physics from the infinite-system density matrix renormalization group.* Phys. Rev. B **86**, 155156 (2012).

[141] R. M. Fye and R. T. Scalettar: *Calculation of specific heat and susceptibilities with the use of the Trotter approximation.* Phys. Rev. B **36**, 3833 (1987).

[142] E. Orignac and R. Chitra: *Mean-field theory of the spin-Peierls transition.* Phys. Rev. B **70**, 214436 (2004).

[143] W. P. Su, J. R. Schrieffer, and A. J. Heeger: *Soliton excitations in polyacetylene.* Phys. Rev. B **22**, 2099 (1980).

[144] E. Fradkin and J. E. Hirsch: *Phase diagram of one-dimensional electron-phonon systems. I. The Su-Schrieffer-Heeger model.* Phys. Rev. B **27**, 1680 (1983).

[145] P. Lee, T. Rice, and P. Anderson: *Conductivity from charge or spin density waves.* Solid State Commun. **14**, 703 (1974).

[146] N. D. Mermin and H. Wagner: *Absence of Ferromagnetism or Antiferromagnetism in One- or Two-Dimensional Isotropic Heisenberg Models.* Phys. Rev. Lett. **17**, 1133 (1966).

[147] S. A. Brazovskii and I. E. Dzyaloshinskii: *Dynamics of a one-dimensional electron-phonon system at low temperatures.* Zh. Eksp. Teor. Fiz. **71**, 2338 (1976).

[148] S. Ryu and Y. Hatsugai: *Topological Origin of Zero-Energy Edge States in Particle-Hole Symmetric Systems.* Phys. Rev. Lett. **89**, 077002 (2002).

[149] J. K. Asbóth, L. Oroszlány, and A. Pályi: *A Short Course on Topological Insulators*, *Lecture Notes in Physics*, volume 919. Springer International Publishing, Switzerland (2016).

[150] A. P. Schnyder, S. Ryu, A. Furusaki, and A. W. W. Ludwig: *Classification of topological insulators and superconductors in three spatial dimensions.* Phys. Rev. B **78**, 195125 (2008).

[151] A. Kitaev: *Periodic table for topological insulators and superconductors.* AIP Conf. Proc. **1134**, 22 (2009).

[152] S. Ryu, A. P. Schnyder, A. Furusaki, and A. W. W. Ludwig: *Topological insulators and superconductors: tenfold way and dimensional hierarchy.* New J. Phys. **12**, 065010 (2010).

[153] R. Jackiw and C. Rebbi: *Solitons with fermion number $\frac{1}{2}$.* Phys. Rev. D **13**, 3398 (1976).

[154] K. Michielsen and H. de Raedt: *Optical Absorption in the Soliton Model for Polyacetylene.* Mod. Phys. Lett. B **10**, 467 (1996).

[155] V. Cataudella, G. De Filippis, and C. A. Perroni: *Transport properties and optical conductivity of the adiabatic Su-Schrieffer-Heeger model: A showcase study for rubrene-based field effect transistors.* Phys. Rev. B **83**, 165203 (2011).

[156] P. W. Anderson: *Absence of Diffusion in Certain Random Lattices.* Phys. Rev. **109**, 1492 (1958).

[157] H. Onishi and S. Miyashita: *Temperature Dependence of Spin and Bond Ordering in a Spin-Peierls System.* J. Phys. Soc. Jpn. **69**, 2634 (2000).

[158] K. Hukushima and K. Nemoto: *Exchange Monte Carlo Method and Application to Spin Glass Simulations.* J. Phys. Soc. Jpn. **65**, 1604 (1996).

[159] H. J. Schulz: *The Crossover from One to Three Dimensions: Peierls and Spin-Peierls Instabilities.* In *Low-Dimensional Conductors and Superconductors*, edited by D. Jérome and L. G. Caron, Springer US, Boston, MA, pp. 95–112 (1987).

[160] L. D. Landau: *On the theory of phase transitions.* Zh. Eksp. Teor. Fiz. **7**, 19 (1937).

[161] D. Jérome and H. J. Schulz: *Organic conductors and superconductors.* Adv. Phys. **31**, 299 (1982).

[162] L. P. Kadanoff and G. A. Baym: *Quantum Statistical Mechanics: Green's Function Methods in Equilibrium and Nonequilibrium Problems.* Addison-Wesley, Redwood City, California (1989).

[163] J. Voit, L. Perfetti, F. Zwick, H. Berger, G. Margaritondo, G. Grüner, H. Höchst, and M. Grioni: *Electronic Structure of Solids with Competing Periodic Potentials.* Science **290**, 501 (2000).

[164] M. Capone, W. Stephan, and M. Grilli: *Small-polaron formation and optical absorption in Su-Schrieffer-Heeger and Holstein models.* Phys. Rev. B **56**, 4484 (1997).

[165] O. S. Barišić and P. Prelovšek: *Conductivity in a disordered one-dimensional system of interacting fermions.* Phys. Rev. B **82**, 161106 (2010).

[166] G. Schubert, G. Wellein, A. Weisse, A. Alvermann, and H. Fehske: *Optical absorption and activated transport in polaronic systems.* Phys. Rev. B **72**, 104304 (2005).

[167] F. J. Dyson: *The Dynamics of a Disordered Linear Chain.* Phys. Rev. **92**, 1331 (1953).

[168] G. Theodorou and M. H. Cohen: *Extended states in a one-demensional system with off-diagonal disorder.* Phys. Rev. B **13**, 4597 (1976).

[169] C. M. Soukoulis and E. N. Economou: *Off-diagonal disorder in one-dimensional systems.* Phys. Rev. B **24**, 5698 (1981).

[170] L. Fleishman and D. C. Licciardello: *Fluctuations and localization in one dimension.* J. Phys. C: Solid State Phys. **10**, L125 (1977).

[171] M. V. Mostovoy, M. T. Figge, and J. Knoester: *Disorder-induced solitons in conjugated polymers.* Europhys. Lett. **38**, 687 (1997).

[172] L. Bartosch and P. Kopietz: *Singularities and Pseudogaps in the Density of States of Peierls Chains.* Phys. Rev. Lett. **82**, 988 (1999).

[173] L. Bartosch and P. Kopietz: *Exact numerical calculation of the density of states of the fluctuating gap model.* Phys. Rev. B **60**, 15488 (1999).

[174] A. J. Millis and H. Monien: *Pseudogaps in one-dimensional models with quasi-long-range order.* Phys. Rev. B **61**, 12496 (2000).

[175] H. Fukuyama and P. A. Lee: *Dynamics of the charge-density wave. I. Impurity pinning in a single chain.* Phys. Rev. B **17**, 535 (1978).

[176] K. Kim, R. H. McKenzie, and J. W. Wilkins: *Universal subgap optical conductivity in quasi-one-dimensional Peierls systems.* Phys. Rev. Lett. **71**, 4015 (1993).

[177] H. Monien: *Exact Results for the Crossover from Gaussian to Non-Gaussian Order Parameter Fluctuations in Quasi-One-Dimensional Electronic Systems.* Phys. Rev. Lett. **87**, 126402 (2001).

[178] L. Bartosch: *Optical conductivity of a quasi–one-dimensional system with fluctuating order.* Europhys. Lett. **65**, 68 (2004).

[179] C. Huscroft, R. Gass, and M. Jarrell: *Maximum entropy method of obtaining thermodynamic properties from quantum Monte Carlo simulations.* Phys. Rev. B **61**, 9300 (2000).

[180] J. Loos, M. Hohenadler, and H. Fehske: *Spectral functions of the spinless Holstein model.* J. Phys.: Condens. Matter **18**, 2453 (2006).

[181] V. Meden, K. Schönhammer, and O. Gunnarsson: *Electron-phonon interaction in one dimension: Exact spectral properties.* Phys. Rev. B **50**, 11179 (1994).

[182] S. Sykora, A. Hübsch, K. W. Becker, G. Wellein, and H. Fehske: *Single-particle excitations and phonon softening in the one-dimensional spinless Holstein model.* Phys. Rev. B **71**, 045112 (2005).

[183] E. C. Creffield, G. Sangiovanni, and M. Capone: *Phonon softening and dispersion in the 1D Holstein model of spinless fermions.* Eur. Phys. J. B **44**, 175 (2005).

[184] T. Giamarchi: *Quantum physics in one dimension.* Internat. Ser. Mono. Phys., Clarendon Press, Oxford (2004).

[185] S. Sykora, A. Hübsch, and K. W. Becker: *Dominant particle-hole contributions to the phonon dynamics in the spinless one-dimensional Holstein model.* Europhys. Lett. **76**, 644 (2006).

[186] M. Hohenadler and W. von der Linden: *Lang-Firsov Approaches to Polaron Physics: From Variational Methods to Unbiased Quantum Monte Carlo Simulations.* In *Polarons in Advanced Materials*, edited by A. S. Alexandrov, Springer Netherlands, Dordrecht, pp. 463–502 (2007).

[187] J. Voit and H. J. Schulz: *Electron-phonon interaction and phonon dynamics in one-dimensional conductors: Spinless fermions.* Phys. Rev. B **36**, 968 (1987).

[188] A. Dorneich and M. Troyer: *Accessing the dynamics of large many-particle systems using the stochastic series expansion.* Phys. Rev. E **64**, 066701 (2001).

[189] P. Pippan, H. G. Evertz, and M. Hohenadler: *Excitation spectra of strongly correlated lattice bosons and polaritons.* Phys. Rev. A **80**, 033612 (2009).

[190] M. Jarrell and J. E. Gubernatis: *Bayesian inference and the analytic continuation of imaginary-time quantum Monte Carlo data.* Phys. Rep. **269**, 133 (1996).

[191] A. W. Sandvik: *Stochastic method for analytic continuation of quantum Monte Carlo data.* Phys. Rev. B **57**, 10287 (1998).

[192] K. S. D. Beach: *Identifying the maximum entropy method as a special limit of stochastic analytic continuation.* arXiv:cond-mat/0403055 (2004).

[193] A. W. Sandvik: *Computational Studies of Quantum Spin Systems.* AIP Conf. Proc. **1297**, 135 (2010).

[194] Jülich Supercomputing Centre: *JURECA: General-purpose supercomputer at Jülich Supercomputing Centre*. J. Large-Scale Res. Facilities **2**, A62 (2016).

Publications

[P1] **M. Weber** and M. Hohenadler: *Two-Dimensional Holstein Model: Critical Temperature, Ising Universality, and Bipolaron Liquid*. arXiv:1709.01096 (2017)

[P2] **M. Weber**, F. F. Assaad, and M. Hohenadler: *Directed-Loop Quantum Monte Carlo Method for Retarded Interactions*. Phys. Rev. Lett. **119**, 097401 (2017)

[P3] **M. Weber**, F. F. Assaad, and M. Hohenadler: *Continuous-time quantum Monte Carlo for fermion-boson lattice models: Improved bosonic estimators and application to the Holstein model*. Phys. Rev. B **94**, 245138 (2016)

[P4] **M. Weber**, F. F. Assaad, and M. Hohenadler: *Thermodynamic and spectral properties of adiabatic Peierls chains*. Phys. Rev. B **94**, 155150 (2016)

[P5] **M. Weber**, F. F. Assaad, and M. Hohenadler: *Phonon spectral function of the one-dimensional Holstein-Hubbard model*. Phys. Rev. B **91**, 235150 (2015)

[P6] **M. Weber**, F. F. Assaad, and M. Hohenadler: *Excitation spectra and correlation functions of quantum Su-Schrieffer-Heeger models*. Phys. Rev. B **91**, 245147 (2015)

[P7] **M. Weber**, M. Hohenadler, and F. F. Assaad: *Kondo screening of spin-charge separated fluxons by a helical liquid*. Phys. Rev. B **89**, 205125 (2014)

Danksagungen

Zum Abschluss möchte ich mich bei allen Menschen bedanken, die mich in den letzten vier Jahren beim Anfertigen dieser Arbeit maßgeblich unterstützt haben. An erster Stelle möchte ich Martin Hohenadler nennen: Vielen Dank für die zahllosen Stunden, die du in die Betreuung meiner Doktorarbeit investiert hast und in denen du deine Faszination für die Physik des Holstein-Modells sowie dessen Lösung mithilfe von Quanten-Monte-Carlo-Methoden mit mir geteilt hast, vielmehr aber noch für die freundschaftliche Unterstützung in allen wissenschaftlichen Belangen der letzten Jahre. Besonderer Dank gilt auch Fakher Assaad, vor allem für seine Bemühungen, mich von einer Doktorarbeit in seiner Arbeitsgruppe zu überzeugen, aber auch eine weitere wissenschaftliche Karriere in Betracht zu ziehen. Beiden danke ich insbesondere für die Freiheiten, die sie mir im Rahmen ihres Forschungsprojektes gegeben haben, um meine eigenen Ideen umsetzen zu können. Darüber hinaus danke ich beiden für die motivierende und freundschaftliche Arbeitsatmosphäre, ebenso wie allen aktuellen und ehemaligen Mitgliedern der Arbeitsgruppe Assaad: Martin Bercx, Stefan Beyl, Kuang-Shing Chen, Florian Goth, Johannes Hofmann, Thomas Lang, Francesco Parisen Toldin, Marcin Raczkowski, Toshihiro Sato, Jonas Schwab, Zhenjiu Wang und Jan Werner. Aus dieser Liste möchte ich insbesondere meinen Bürokollegen Johannes Hofmann hervorheben, mit dem ich viele spannende und konstruktive Diskussionen über Physik führen durfte. Für das sorgfältige Korrekturlesen dieser Arbeit danke ich im Speziellen Johannes, Martin und Stefan.

Mindestens genauso wichtig für den Erfolg dieser Arbeit war der emotionale Rückhalt, den mir Freunde und Familie besonders in den schwierigen Phasen der Promotion gegeben haben. Vor allem möchte ich mich bei meinen Eltern Hartmut und Monika für ihre bedingungslose Unterstützung bedanken, die ich in den letzten Jahren nicht hätte missen wollen. Für ihre Unterstützung, vornehmlich im schwierigen letzten Jahr der Promotion, danke ich all meinen Freunden, denen Dank gebührt, insbesondere aber Leonard und Jonathan.

Diese Arbeit wäre weiterhin ohne den Zugang zu modernen Hochleistungscomputern nicht möglich gewesen. Deswegen möchte ich meine Doktorarbeit mit denselben Worten abschließen, mit denen wir auch unsere Veröffentlichungen beenden: *We gratefully acknowledge the computing time granted by the John von Neumann Institute for Computing (NIC) and provided on the supercomputer JURECA [194] at the Jülich Supercomputing Centre.*